

FINAL REPORT

U.S. Air Force-Taiwan Nanoscience Program

**Novel Photovoltaic Nanocomposites Based on
Single-Molecule Optoelectronics on Functionalized Carbon
Nanotubes Percolated Networks and the Polymer Chain
Conformation Effect**

(AOARD-084125)

Principal Investigator

Arnold C.-M. Yang

acyang@mse.nthu.edu.tw

Department of Materials Science and Engineering

National Tsing Hua University

101, Kuang Fu Road, Section 2, Hsinchu City, Taiwan

Phone: +886-3-572-0792, FAX: +886-3-572-2366

Report Documentation Page				Form Approved OMB No. 0704-0188	
Public reporting burden for the collection of information is estimated to average 1 hour per response, including the time for reviewing instructions, searching existing data sources, gathering and maintaining the data needed, and completing and reviewing the collection of information. Send comments regarding this burden estimate or any other aspect of this collection of information, including suggestions for reducing this burden, to Washington Headquarters Services, Directorate for Information Operations and Reports, 1215 Jefferson Davis Highway, Suite 1204, Arlington VA 22202-4302. Respondents should be aware that notwithstanding any other provision of law, no person shall be subject to a penalty for failing to comply with a collection of information if it does not display a currently valid OMB control number.					
1. REPORT DATE 07 DEC 2009		2. REPORT TYPE FInal		3. DATES COVERED 07-07-2008 to 06-08-2009	
4. TITLE AND SUBTITLE Single-Molecule Optoelectronics via Polymer Templatation on Percolated Carbon Nanotube Skeletons or Molecularly Sheared				5a. CONTRACT NUMBER FA23860814125	
				5b. GRANT NUMBER	
				5c. PROGRAM ELEMENT NUMBER	
6. AUTHOR(S) Chang-Mou Yang				5d. PROJECT NUMBER	
				5e. TASK NUMBER	
				5f. WORK UNIT NUMBER	
7. PERFORMING ORGANIZATION NAME(S) AND ADDRESS(ES) National Tsing Hua University,101, Kuang Fu Rd, Sec 2,Hsinchu 30043,Hsinchu ,tw,30043				8. PERFORMING ORGANIZATION REPORT NUMBER N/A	
9. SPONSORING/MONITORING AGENCY NAME(S) AND ADDRESS(ES) AOARD, UNIT 45002, APO, AP, 96337-5002				10. SPONSOR/MONITOR'S ACRONYM(S) AOARD	
				11. SPONSOR/MONITOR'S REPORT NUMBER(S) AOARD-084125	
12. DISTRIBUTION/AVAILABILITY STATEMENT Approved for public release; distribution unlimited					
13. SUPPLEMENTARY NOTES					
14. ABSTRACT This is the final report of a project on the fundamental sciences and technical processes of single molecule optoelectronics, as well as of nanocomposites of carbon nanotubes and polymers, that were systematically investigated in interrelated structured segments.					
15. SUBJECT TERMS Conductive Polymers, nano photonics, Solar Cells					
16. SECURITY CLASSIFICATION OF:			17. LIMITATION OF ABSTRACT Same as Report (SAR)	18. NUMBER OF PAGES 131	19a. NAME OF RESPONSIBLE PERSON
a. REPORT unclassified	b. ABSTRACT unclassified	c. THIS PAGE unclassified			

Abstract

In this research project, fundamental science and technical processes of single molecule optoelectronics of conjugated polymers, as well as of nanocomposites comprised of carbon nanotubes and polymers, were systematically investigated in inter-related structured segments. Significant novel and useful results had been acquired, which have paved the solid basis for future fruitful explorations in this important emerging subject.

Firstly, the mechano-electronic interactions of conjugated polymer chains were investigated in stretched polymer films. The extraordinarily large optoelectronic enhancement of single molecule conjugated polymers induced by extensive stretching was studied. The deformation triggered enhancement was found to be associated with an increase of non-radiative lifetimes of the stretch-hardened polymer chains. This indicated the important role of dramatically increased polaron formation energy (Chapter 1).

The mechano-electronic effect due to chain conformation was also observed in the monolayer films (ca. 3-4 nm) resulted from dewetting of ultrathin conjugated polymer films on rigid substrate. This observation offered an application opportunity of the large mechano-electronic effect through a process full compatible with the current semiconductor manufacturing techniques. It thus has opened a window for making real optoelectronic devices (electroluminescence and photovoltaics) exploiting enhanced single molecule properties. The mechano-optical enhancement was found to be highly dependent on the shear deformation at the substrate and the original molecular packing in the ultrathin polymer films. Ongoing work includes multi-dewetting processes designed for making thick stacks of monolayers for high intensity applications (Chapter 2).

The physical states of the ultrathin polymer films were thus investigated in details in the light of residual stress and molecular packing (Chapter 3), stress relaxation (Chapter 4), and elastic modulus of the ultrathin films (Chapter 4). A molecular model that describes molecular condensation during film formation enroute of spin coating of dilute polymer solution was constructed in order to explain the various unique thin film packing problems we observed, and to predict the behavior of more complicated polymer systems (Chapter 4). The mechanical interactions between ultrathin polymer films and substrate during dewetting were further investigated with the substrate being a soft elastic rubber to fully elucidate the interaction details in nanometer scales (Chapter 5).

The single molecule behavior and chain conformation effect of conjugated polymer were further exploited in the nanocomposites comprised of percolated carbon nanotubes and conjugated polymers. Conjugated polymers were grafted to carbon

nanotubes in order to investigate the chain conformation effect on the carbon nanotube templates (Chapter 6). As a further investigation of the nanocomposite systems, the mechanical interactions between the well-dispersed carbon nanotubes and the glassy polymer chains were studied in both the multi-walled and single walled carbon nanotubes systems (Chapter 7).

The contents of Chapter 5 and the first part of Chapter 7 were published respectively in Physical Review Letters and Macromolecules. Seven more manuscripts based on the results revealed in Chapters 1, 2, 3, 4, and 7 are to be submitted for publication shortly.

Table of Contents

Chapter 1: Large Increase of Optoelectronic Efficiency of Conjugated Polymer by Extreme Plastic Deformations

Chapter 2: Dramatic Optoelectronic Enhancement Induced by Dewetting Ultrathin Conjugated Polymer Films

Chapter 3: Molecular Stresses in Metastable Ultrathin Polymer Films Prepared by Spin Coating

Chapter 4: Metastable Ultrathin Polymer Films

- a) Relaxation of Residual Stress in Ultrathin Polymer Films
- b) Derivation of Surface Tension and Shear Modulus of Polymer Thin Films Using a Model Based upon Power Spectral Density
- c) Macromolecule Condensation during Formation of Ultrathin Films

Chapter 5: Viscoelastic Thin Polymer Films under Transient Residual Stresses: Two-Stage Dewetting on Soft Substrates

Chapter 6: Grafting Conjugated Macromolecules to Percolated Carbon Nanotubes Network Templates for Optoelectronic Functions

Chapter 7: Nano-Mechanical Interactions between Single-Walled Carbon Nanotubes (CNTs) and Entangled Glassy Polymer Chains

- a) Single-Walled CNTs Nanocomposites
- b) Multi-Walled CNTs Nanocomposites

Chapter 1: Large Increase of Optoelectronic Efficiency of Conjugated Polymer by Extreme Plastic Deformations

Abstract

Polymers are known to have poor optoelectronic quantum efficiencies that can be linked to the inherent self-trapping of photon-induced charges (excitons) to the soft 1-D hydrocarbon chains. However, we observed a very large photoluminescence enhancement, by as high as 1000%, when the molecules dispersed in optically inert matrix were deformed by stretching up to strain $\varepsilon = 300\%$. There was a strain threshold for the enhancement, above $\varepsilon = 60\%$, and the enhancement decreased and finally vanished as the molecular concentration in the matrix increased. Accompanying with the large photoluminescence increase, the luminescence spectrum remain largely unchanged but the non-radiative lifetime increased significantly, indicating an emerging obstruction to the phonon-exciton interactions. The dramatic effect was very sensitive to stress relaxation and intermolecular interactions which may reduce or even offset the enhancement effect. Chain segmental motions that lead to varying local chain conformation for charge entrapment may be restricted when fully stretched, thus giving rise to a dramatic increase of quantum efficiencies. Our results have important implications for the development of high efficiency energy or electronic devices based on polymers.

Introduction

Conjugated polymers have attracted considerable attention due to their intriguing optoelectronic properties and low material and processing costs that hint ubiquitous roles for prospective luminescent, photovoltaic, and electronic applications [1-6]. With alternating π -bonds in the hydrocarbons backbones, conjugated polymers harvest incident photons that match their vibronic energy gaps, generate singlet excitons which thereafter undergo a series of intricate radiative or nonradiative energy transfer processes [6-19]. Although the detailed pathways remain illusive, phonon interactions with the excitons to form charged polarons or via intersystem crossing convert into neutral triplet excitons play a central role in the nonradiative processes. These interactions leave clues in photoinduced absorption bands at, respectively, the near IR or visible light spectral ranges [7,15-17]. Compelling evidence revealed that the formation of non-emissive species in conjugated chains may account for more than 90% of the total photo-energy uptake [8,10]. Such a deficiency in polymer-based quantum yields has long blocked feasible energy or electronic devices from emerging.

The strong phonon interactions in conjugated polymers are rooted to their inherent

flexible nature of the 1-D molecular chains. By means of facile local conformation changes (cis-gauche or gauche-trans transitions) or reversible chromophore transformation (e.g., the well-established cyclization of diarylethenes into dihydrophenanthrene systems) [6,17], self-trapping of charges occurs and it hinders considerably the charge conductivity along the chains. Other than these intramolecular interactions, reactions between adjacent photoexcited segments of different chains prevail and inflict significant reduction of radiative efficiency. The intermolecular interactions explain the dramatic enhancement in luminescent efficiencies routinely observed when conjugated polymers are dispersed into single molecules in blends or in solutions [20-23]. In consequence of the intra- and intermolecular interactions, the non-radiative energy dissipations [8-13] are characterized by charge hopping or degenerated molecular orbital states between adjacent molecular segments that increase the radiative lifetime of the photoexcited species.

Thus, when polymer chains are individually dispersed and then stretched, large mechano-optoelectronic effects are expected. So far, very limited work is done in this area [24-25]. As will be shown in the following, with very large non-relaxing deformations applied to dispersed conjugated polymer chains, dramatic enhancements in optoelectronic efficiencies (up to above a 25 folds increase) have been observed. The experiment was carried out by stretching a conjugated polymer, poly-(2-methoxy-5-(2'-ethylhexyloxy) -*p*-phenylenevinylene) (MEH-PPV) dispersed in a saturated glassy polymeric thin film. The matrix polymer was either polystyrene (PS) or polyphenylene oxide (PPO), each of which demonstrates, respectively, the generic brittle (crazing) or ductile (local shear yielding) nano-plastic flows [26-35] upon stretching. The observations clearly manifest a strong dependence of the optoelectronic behavior of polymers on the mechanical state that can be manipulated by externally applied constraints.

Experimental Section

The PS ($M_w = 2,000,000$ g/mol., $M_w/M_n \leq 1.3$) and the styrene oligomers ($M_w = 2,032$ g/mol., $M_w/M_n \leq 1.06$ and $MW = 760$ g/mol., $M_w/M_n \leq 1.1$) were bought from the Pressure Chemical Co., and the conjugated polymer MEH-PPV ($M_n = 150,000 \sim 250,000$ g/mol., $M_w/M_n \approx 5$) was purchased from Sigma-Aldrich Chemical Co. PPO ($M_w = 244,000$ g/mol., $M_w/M_n \approx 3$) was also purchased from Sigma-Aldrich Chemical Co. All polymers were used as received without further purification. Blends of MEH-PPV with either PS or PPO were prepared with MEH-PPV weight fractions c ranging from 0.1 wt % to 10 wt %. Thin polymer films on glass slides were prepared by spin coating from polymer solutions in equal-parted solvent mixture of toluene, tetrahydrofuran, and cyclohexanone. The polymer solution, generally of polymer

concentration in the range of 1 – 30 mg/ml, was stirred slowly, wrapped in aluminum foil to protect from UV lights, at room temperature for approximately two day, followed by syringe filtration using a 0.2 μm pores filter to remove dust or un-dissolved particles. The filtration produces no effect on the actual values of the MEH-PPV fraction for samples of low c 's where the conjugated polymer dissolves readily. However, it may possibly cause a negative deviation of c values for samples of high c 's where significant aggregates are present, and thus this was taken into account for data analysis of the concentrated samples. The spin speed was in the range of 2500 rpm ~ 3000 rpm to produce films of thickness around 0.5 μm . When the solvent evaporated, the film was floated off onto the surface of water bath and subsequently picked up by a piece of copper grids, dried for about 1 day, and then ready for tensile testing [26-27]. The copper grids, before the sample preparation, were first annealed at 600 $^{\circ}\text{C}$ in sealed vacuum for one hour to increase plastic ductility suitable for good loading support of the polymer thin films, which are to be tested under tensile deformations [26-27]. They were then dipped briefly in a PS solution to leave a thin layer of polymer on the grid bars before picking up the film from the water bath. The specimen of polymer thin film on copper grids was shortly exposed to the solvent vapor to enhance bonding between the film and supporting copper grids [26-27].

The specimen was then mounted in a strain jig and stretched uni-axially under an optical microscope for deformation to be observed. After the stretching, the sample was retreated from the strain jig but the deformation applied to the thin film was retained by the plasticized supporting copper grids. The stretched samples were then tested in photoluminescence spectrometer (Perkin-Elmer LS-55) using suitable excitation frequencies to evaluate its photo-luminescence (PL) properties. Signal from blank copper grids was used for background subtraction. Atomic force microscope (Digital Instrumental, Nanoscope IIIa and DimensionTM 3100) and transmission electron microscope (JEOL JEM-2010, TEM) were employed to investigate the topography and microstructure of local deformation zones of crazes. A confocal PL microscope (Leica SP2-Confocal) was also used to observe the stretched samples.

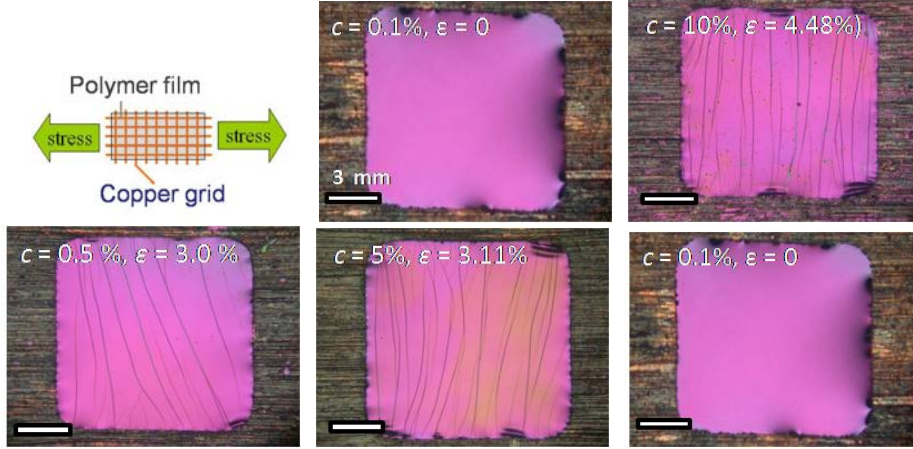
Results and Discussions

Stretching of the polymer film

The prepared thin films of MEH-PPV dispersed in PS for the experiment were smooth and tight without wrinkles before stretching (Fig. 1a). Local deformation zones of crazes grown perpendicular to stretching emerged when a strain (ε) was applied beyond a critical value (ε_c), approximately $\varepsilon_c = 0.5\%$ [26-31]. As the strain increased further, crazes widened amid the initiation of new ones (Fig. 1a). Under

TEM, interconnected fibrils of large extension ratio ($\lambda \sim 4.0$) [26-31] that orient parallel to the stretching direction were observed within crazes (Fig. 1b). The local strain of the crazed matter was determined to be close to the upper bound permitted for a well entangled chain network [26-31], indicating that the chains within crazes are fully stretched. The crazing behavior of the films as observed under an optical microscope did not show significant dependence on MEH-PPV weight fraction (c) for the range from 0 to 10% (Fig. 1a).

a).



b)

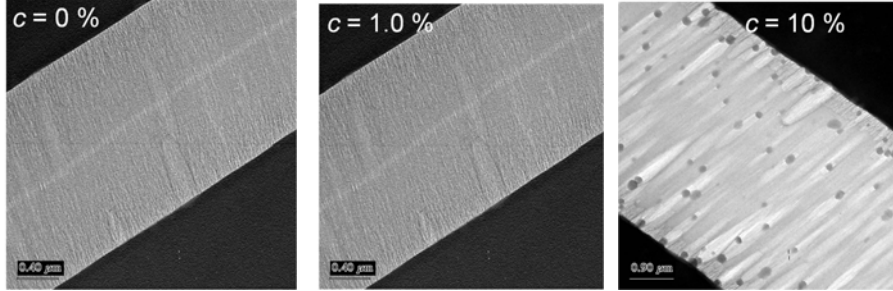


Figure 1. a) Optical micrographs of the polymer film for various MEHPPV fractions c 's and applied strains ϵ 's. b) TEM micrographs of crazes for various c 's.

During the stretching, craze formation acts effectively as a strain sink [26-28] and the amount of polymer drawn into crazes V_z can be related to ϵ and Poisson's ratio ν by $V_d = (\epsilon - \epsilon_c)[1 + \epsilon(1 - 2\nu)] \approx (\epsilon - 0.5\%)$ if V_z is expressed in volume fraction and the void volume between fibrils is excluded. The topography of the crazed region in the film clearly shows a local depression (Fig. 2a, inset) and the depth of the depression d_d first increases linearly with craze width w_d and then levels off to a plateau D when w_d becomes greater than a thickness-dependent threshold, illustrating a necking process in nanometer scales (Fig. 2a) [32-35]. The plateau depth D can be related to the draw ratio λ of the crazed matter and film thickness τ by $\lambda = 1.25(1 -$

$2D/\tau)^{-1}$, where the void volume fraction within the craze was calibrated to be 0.2 corresponding to closest fibril packing [33,34]. Similar relationships exist for shear deformation zones in ductile polymers, such as PPO or partially plasticized PS's, but the critical strain ε_c 's are generally greater than 0.5%, to be around 1- 3%, and the void volume within the shear deformed matter is reduced to zero.

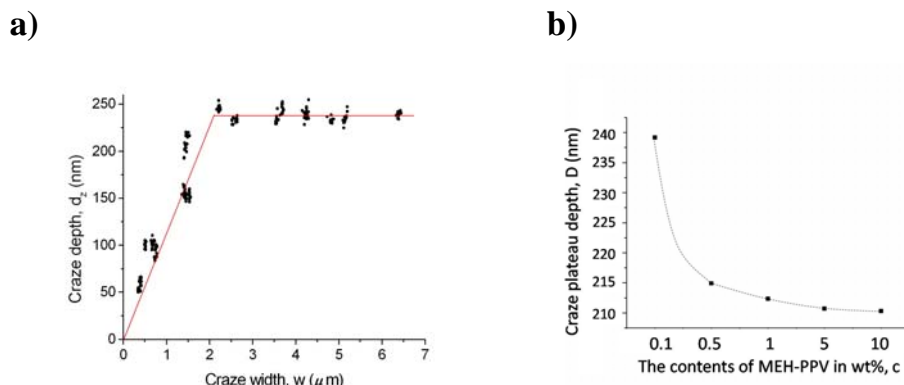


Figure 2. a) Craze depth versus craze width in the strained films, illustrating a micro-necking characteristic. b) The plateau craze depth decreases with c but tends to level off for large c 's.

The dispersion of MEH-PPV in PS matrix was generally adequate for $c \leq 1\%$, but for larger c 's ($c \geq 5.0$ wt %) small aggregate particles that had escaped the filtration were present in the films, as visible in crazes under TEM (Fig. 1b). The well fibrillated craze microstructure generally demonstrates no dependence on c for the range explored here, but the fibril draw ratio λ decreases slightly with c as evident in the dependence of the plateau depth D versus c (Fig. 2b). This clearly indicates that the dispersed MEH-PPV molecules do in fact participated in the nano-plastic flows. The molecular strains of the dispersed MEH-PPV in fact are slightly less than that of the PS matrix molecules, but for the purpose here they were assumed to be identical to the λ measured in the crazes of the films.

PL enhancement by plastic flows

The PL spectra of the un-stretched polymer films on copper grids (Fig. 2c) manifest distinct peaks at approximately 550 nm and 600 nm corresponding to, respectively, the intra-chain and inter-molecular transitions [11,12,22]. The intra-chain luminescence intensity (550 nm emission) increases with c but deviates considerably lower than linearity for $c \geq 1\%$, indicating the strong detrimental effect of inter-molecular interactions [8-13]. When normalized to c , the intensity is about 20 times greater for $c = 0.1\%$ than in $c = 10.0\%$, as expected from the suppression of inter-chain energy loss pathways [8-13].

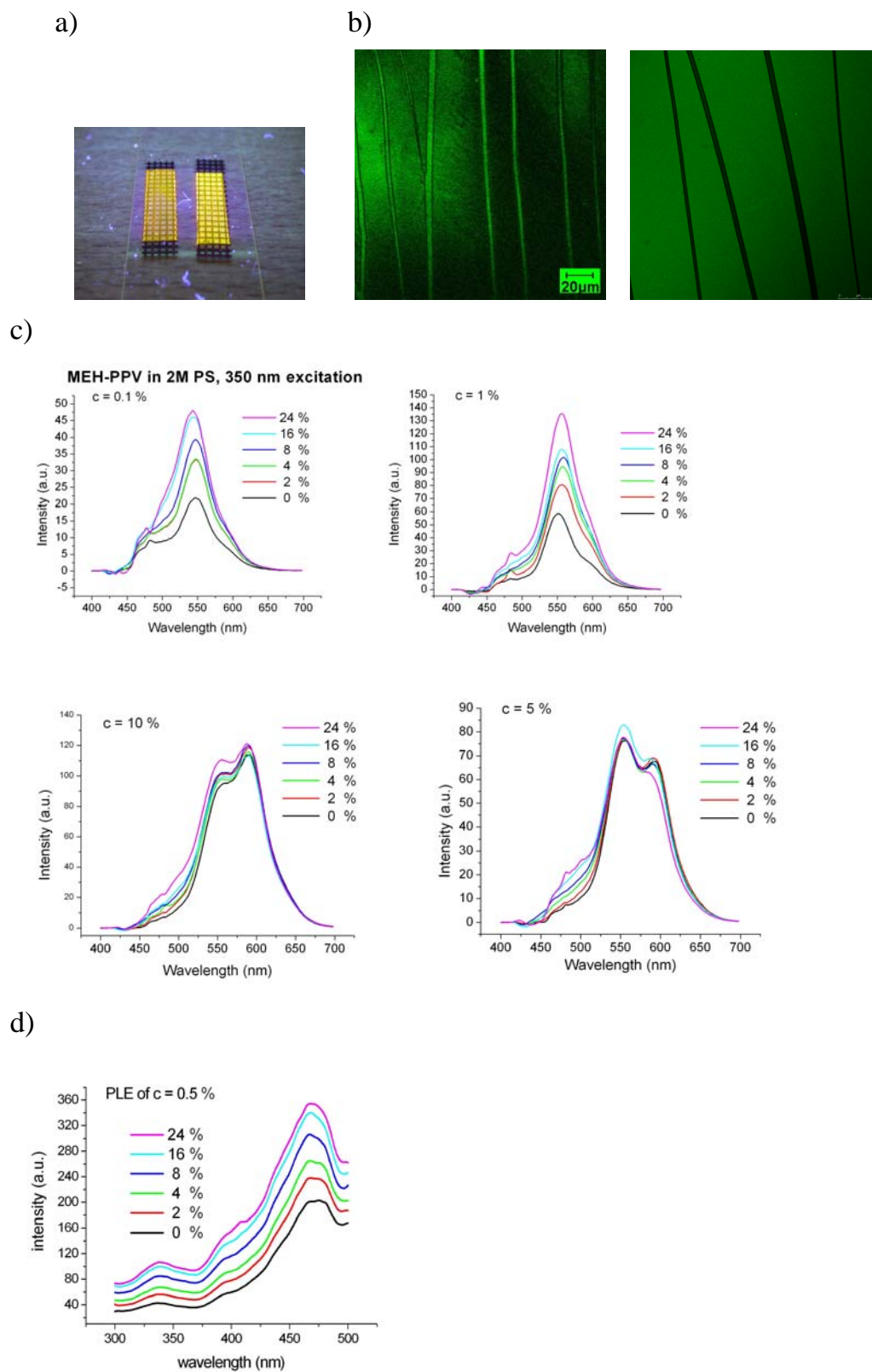
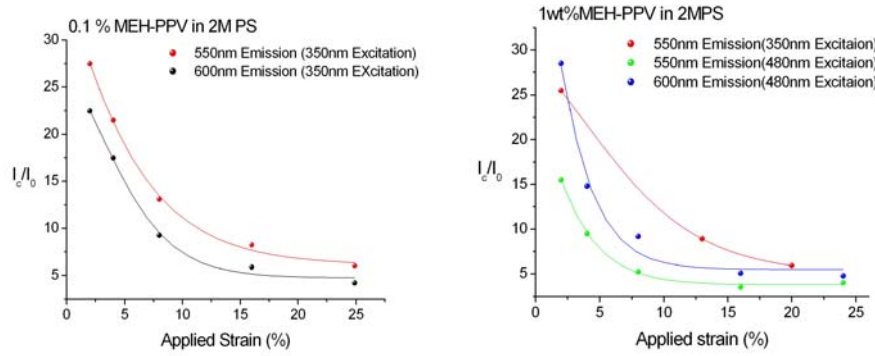


Figure 3. a) Luminescence enhancement in films of diluted MEH-PPV is observable to the bare eye with various viewing angles. b) Confocal PL micrographs of crazed

sample (left: 1wt% MEH-PPV, $\varepsilon = 8\%$; right: 10 wt% MEH-PPV, $\varepsilon = 8\%$) with excitation frequency at 488 nm. c) PL luminescence spectra for various c 's as a function of applied strain (excitation wavelength: 350 nm). The intensity below ~ 500 nm, which is strongly influenced by background luminescence of scattered incident beam, should be ignored. d) The PLE spectrum of the photoluminescent film is independent of the applied strain.

a)



b)

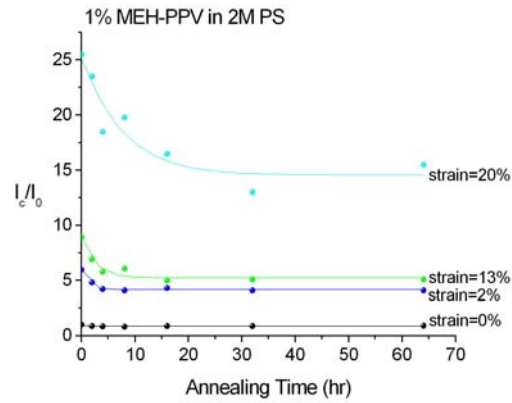


Figure 4. a) The optoelectronic enhancement for the well-dispersed MEH-PPV as a function of applied strain in various c 's. b) The enhancement decreases with annealing time at 90°C in purged N_2 during which crazes were relaxed.

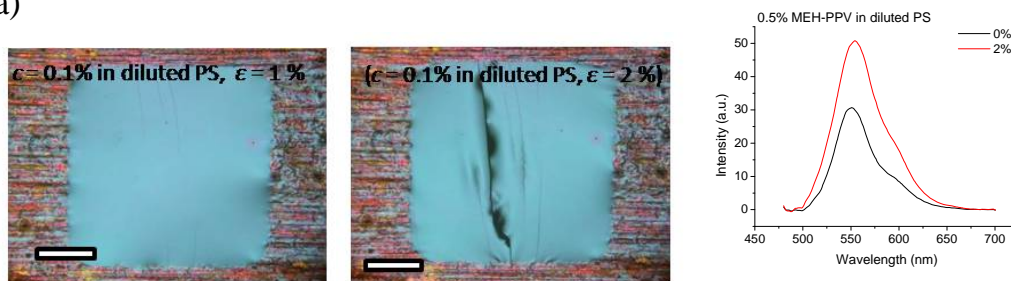
When a strain was applied to the films of low MEH-PPV fractions ($c \leq 1\%$), a large enhancement on photoluminescence (PL) that was obvious to the bare eye occurred (Figs. 3a). Under a confocal PL microscope, crazes were luminous brightly against the backdrop of elastically stressed film (Fig. 3b) indicating that the well dispersed conjugated polymer emits light more efficiently when stretched within the crazes. In Fig. 3c where the PL spectra from the films of various c 's are shown, the film of lower MEH-PPV fractions ($c \leq 1\%$) illustrates a considerable increase of PL intensity with an applied strain. (The intensity below ~ 500 nm, which is due to background luminescence of scattered incident beam, should be ignored.) On the other hand, for higher c 's ($\geq 5.0\%$), the PL intensities were virtually invariant with the applied strains. That is, no optoelectronic enhancement due to stretching was observed when the intermolecular interactions between the MEH-PPV molecules were dominant. For all samples, the spectra did not show significant shift of the major emission peaks with the applied strain, consistent with PLE spectra which were essentially invariant to ε (Fig. 3d). Comparable PL augments were observed under either 480 nm or 350 nm excitation wavelength, but a shorter wavelength of 350 nm was used for most of the data collections here to minimize the interference effect of incident beam.

The PL enhancement as effected by the local molecular deformation was quantified by analyzing the PL intensity, I_t , as contributed from the plastically flowed regions (the crazes or shear deformation zones), I_d , and that from the elastic regions, I_0 , i.e., $I_t = I_0(1 - V_z) + I_d V_z$. The PL enhancement is defined as the ratio of I_d/I_0 since, as will be shown later that small strain produces no enhancement effect, I_0 can be regarded as identical to that of zero strain. The PL enhancement I_d/I_0 was thus readily determined from the measured PL intensity I_t and the applied strain ε according to $I_d/I_0 = I_t/I_0(1/V_z) - 1$ where $V_z = (\varepsilon - 0.5\%)$. As shown in Fig. 4a, the enhancement is approximately 25 fold for small strains ($\varepsilon \sim 2.0\%$) but decreases to a level approximately 6 fold for the largest strains at around 20% (beyond which the supporting copper grids starts to break).

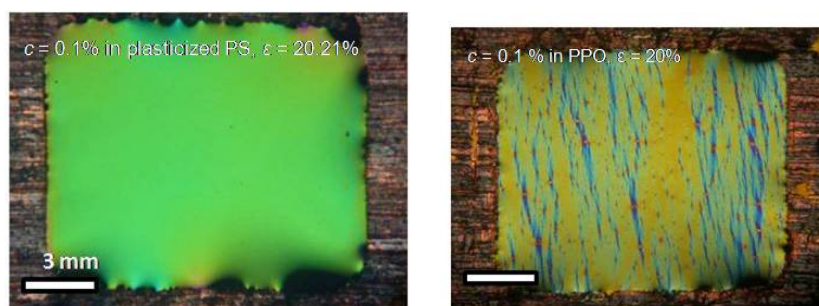
Since it is well known that wider crazes are prone to undergo fibril coalescence arising from fibril relaxation [30], the origin behind the decrease of PL enhancement with applied strain was attributed to local fibril relaxation in the wider crazes that are more populated in films of greater strains (Fig. 1a). To support this view, a physical annealing experiment (90°C , N_2 -purged) was conducted on the stretched samples. The enhancement I_d/I_0 was found to decrease with annealing time and eventually saturate (Fig. 4b) when the craze microstructure finally stabilized. Particularly, the decrease in the samples of a small strain ($\varepsilon = 2\%$) is remarkable, clearly indicating

that the relaxation of craze fibril gives rise to significant reduction of the PL enhancement triggered by large plastic flows.

a)



c)



d)

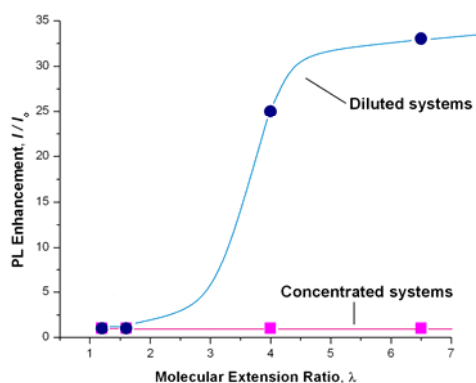


Figure 5. a) When diluted with styrene oligomer ($M_w = 2000$ g/mol.), the film samples embrittle and break at low strains. Corresponding to the increased local strain within crazes, from $\varepsilon = 300\%$ to $\varepsilon = 550\%$, the PL intensity (taken from intact films) showed significant increases that accounted for an enhancement factor of approximately 33. b) The film of fully plasticized PS matrix (with blended 55 wt.% styrene oligomer of $MW = 760$ to PS) deforms uniform up to $\varepsilon \sim 20\%$. For these films, no enhancement effect on photoluminescence was observed. c) Applying strain to samples of MEH-PPV dispersed in PPO matrix produces shear deformation zones within which the local molecular deformation is around $\varepsilon \sim 60\%$. In these samples, negligible enhancement effect was observed. d) The PL enhancement of well dispersed MEH-PPV versus molecular deformation.

In addition, the PL enhancement that decreases with strain may also be contributed by the fact that narrow crazes contain fibrils of greater draw ratio due to the existence of mid-rib, a trail marked by highly stretched matter left at the craze center by the propagating craze tip [26-28,31]. Since the width of the mid-rib is essentially constant with craze width, narrow crazes have greater average local plastic strains. The effect of local deformation on the PL enhancement was further explored by using diluted entangled PS as the matrix in which the dispersed MEH-PPV molecules are subject to greater molecular strains in the crazes [31]. This was done by blending the long PS chains with a styrene oligomer ($M_w = 2000$ g/mol.) which is too short to entangle and serves as diluent to the entangled chain network. The craze draw ratio increased substantially from $\lambda \sim 4.0$ to $\lambda \sim 6.5$ as the films embrittled [31] at diluent volume fraction $c_{dil} = 0.5$. For these samples, an even greater PL enhancement, approximately a 33 fold increase, was observed (Fig. 5a) with only a small strain $\varepsilon = 2\%$. Evidently, greater molecular deformations always lead to larger PL enhancement if the conjugated macromolecules are well dispersed and fully stretched. In this regime, the optoelectronic enhancement I_d/I_0 appears to be approximately independent of c , ranging from 5 to 25, depending on the condition of the imposed molecular strain.

This remarkable mechano-optoelectronic effect, however, was not observed in the films with a concentrated MEH-PPV content ($c \geq 5.0\%$) (Fig. 3c). It is important to note that these films were producing comparable population of crazes (Fig. 1a) with similar craze microstructures (Fig. 1b). This observation highlights the strong influence due to inter-molecular interactions on the mechano-optical effect [8,11-13].

For molecular deformations lower than $\lambda = 4.0$, the stretch-induced PL enhancement was explored by using either the fully plasticized PS or PPO as the binding matrix for MEH-PPV. The former was prepared by blending a styrene oligomer ($MW \sim 760$ g/mol.) to the long PS chains so that the film could be strained uniformly without the formation of crazes occurring (Fig. 5b). In this case, the local molecular deformation is equal to the applied strain. For samples with PPO being the binder matrix, the resulted molecular deformation in the local shear deformation zones (Fig. 5c) is approximately $\varepsilon = 60\%$ [29]. In both systems, the PL spectra did not show any detectible enhancement upon application of strains, indicating that the threshold molecular strain for the mechano-optoelectronic effect is at least beyond $\varepsilon = 60\%$.

Thus, the dependence of the optoelectronic enhancement in MEH-PPV macromolecules on molecular deformation can be summarized by a curve shown in Fig. 5d, where the enhancement is very small for molecular deformations less than $\varepsilon =$

100% but increases dramatically thereafter and approaches as high as ~33 fold when the deformation reaches $\varepsilon = 550\%$.

Molecular constraints induced by extreme deformations

The origin of the large strain-induced enhancement may be unveiled by a revisit of the classical Frank-Condon model associated with the vibronic interactions in general molecular materials. Upon photoexcitation, the molecular orbital is perturbed around where the electron-hole pair is created. Then, due to the induced steric interactions, local atomic spatial configurations alter to minimize the increased electrostatic potential. For conjugated polymers, the photo-induced charge perturbation extends over a length scale of around 1 nm, or approximately 6 - 8 repeating units, large enough to allow local bond rotations to take place and form well-separated charged polarons. These passive chain conformation changes constitute to the molecular basis for vibronic interactions and charge self-trapping. Now, for a polymer chain fully stretched and maintained by a large force, bond rotations are made much more difficult to proceed because the Young's modulus has increased substantially and any chain rotation will change the chain length. Consequent to the diminishing tendency of charge self-trapping, charge recombination prevails and leads to a dramatic increase of radiative quantum efficiencies. The large threshold truthfully reflects the requirement of large deformations for effective segmental constraints. The enhancement versus molecular strain may mimic the corresponding increase of the Young's modulus of a single molecule. The strong sensitivity of PL enhancement on mechanical relaxation also reflects the critical dependence of Young's modulus of single molecules on chain slackness.

Consistent with this scenario, large increases of charge conductivity were observed in stretched solid films of polyaniline in which over an order of magnitude increases have been documented [36].

Moreover, the measured average binding energies of trapped polarons in ordinary MEH-PPV were reported to be ranging approximately from 0.09 eV to 0.22 eV [14,17,18], which are in a comparable energy scale as that of chain vibration, ~ 0.2 eV, as determined from photo-induced IR-active vibration [17] and that of segmental rotation barriers, ~ 0.1 – 0.2 eV, from idealized molecular models [37]. This general information has provided a well justified energy landscape for the dramatic mechano-optoelectronic interactions reported here. Specifically, for MEH-PPV, cis defects have been regarded as the principal precursors for the photoinduced cyclization of diarylethenes into dihydrophenanthrenes that gives rise to the prevalent formation of charged polarons [17]. These structural defects introduce deep levels within the energy gap to trap photo-induced charges and dissipated the excited energy

through multi-phonon emission, thus preventing luminescence [17,19]. Recently it was found that an exciton is capable of moving along a single chain of MEH-PPV without losing its quantum coherence [38,39]. This is in sharp contrast to the intermolecular hopping mechanisms dominant in concentrated systems [38,39]. As we observed here, the intrachain exciton transport can be vastly enhanced in a fully extended stretched conjugated macromolecule due to the reduced tendency of self-trapping of charges.

Other effects

Other effects may also participate in the processes observed here. Molecular deformations may spur increased absorption efficiency due to molecule unfolding to the incident light. This effect, although not the principal driving force, may further increase the observed mechano-induced enhancement.

One important corollary from the mechano-optoelectronic interactions revealed here is the large effect due to molecular constraints. If vibronic interactions in conjugated polymers can be controlled to result in dramatically increased optoelectronic quantum gains, many feasible means other than plastic flows may be used to this end. Finally, molecular constraints may also lead to a significant increase of charge conductivity, thus offering a new window for efficient electronic devices based on polymers.

Conclusions:

In summary, a large mechano-optoelectronic effect of conjugated polymers was discovered in that the optoelectronic efficiency can be substantially enhanced by stretching the molecules beyond a large threshold molecular strain. The enhancement can be as high as ~ 33 fold as observed here, although other secondary factors accompanying the molecular deformations may also contribute to the observed enhancement. For molecular deformations smaller than the threshold, however, negligible enhancement was observed. In addition, the strain-induced quantum gain is very sensitive to detrimental local stress relaxation and inter-chain energy dissipation. The observations indicate that, when constrained by extreme plastic deformations, the strong electron-phonon interactions inherent to the long 1-D molecules are drastically depressed due to the increased chain stiffness that restricts conformation re-adjustment and thus charge self-trapping. The dramatic mechano-optoelectronic enhancement effect reported here has important implications for the development of high efficiency energy and electronic devices based on polymers.

Acknowledgements:

The authors greatly appreciate the instructive discussions with Prof. Gunter Reiter of University of Freiburg, Germany, Dr. Mark Geoghegan of University of Sheffield, U.K., Prof. J. H. Hsu of National Sun Yat Sen University, Kaohsiung, and Prof. Jonathan White of University of Yuanze, Chungli, Taiwan. The research work is contributed substantially by K. P. Tung as a graduate student who died of flu in 2008. The work is supported by National Science Council (NSC) of Taiwan and a grant from the US Air Force (AOARD-084125) under the Taiwan NSC-US Air force Nanoscience Initiatives.

References:

- [1] A. G. MacDiarmid, A. J. Epstein, *Faraday Discuss. Chem. Soc.* **317** (1989).
- [2] J. H. Burroughes, D. D. C. Bradley, A. R. Brown, R. N. Marks, K. MacKay, R. H. Friend, P. L. Burns, A. B. Holmes, *Nature* **347**, 539 (1990).
- [3] C. Tanase, E. J. Meijer, P. W. M. Blom, D. M. de Leeuw, *Phys. Rev. Lett.* **91**, 216601-1 (2003).
- [4] T. Virgili, G. Cerullo, L. Luer, G. Lanzani, *Phys. Rev. Lett.* **90**, 247402-1 (2003).
- [5] N. Tessler, G. J. Denton, R. H. Friend, *Nature* **382**, 695 (1996).
- [6] M. Fox, *Optical Properties of Solids*, Oxford University Press, 2001.
- [7] Z. Vardeny, E. Ehrenfreund, O. Brafman, M. Nowak, H. Schaffer, A. J. Heeger, F. Wudl, *Phys. Rev. Lett.* **56**, 671 (1986).
- [8] M. Yan, L. J. Rothberg, F. Papadimitrakopoulos, M. E. Galvin, and T. M. Miller, *Phys. Rev. Lett.* **72**, 1104 (1994).
- [9] Z. An, C. Q. Wu, and X. Sun, *Phys. Rev. Lett.* **93**, 216407-1 (2004).
- [10] D. Moses, A. Dogariu, A. J. Heeger, *Synthetic metals* **116**, 19 (2001)
- [11] I. B. Martini, A. D. Smith, and B. J. Schwartz, *Phys. Rev. B* **69**, 035204 (2004).
- [12] B. J. Schwartz, *Annu. Rev. Phys. Chem.* **54**, 141 (2003).
- [13] J.-L. Bredas, J. Cornil, D. Beljonne, D. A. Dos Santos, and Z. Shuai, *Acc. Chem. Res.* **32**, 267 (1999).
- [14] K. D. Meisel, H. Vocks, and P. A. Bobbert, *Phys. Rev. B* **71**, 205206 (2005).
- [15] M. G. Roe, J. M. Ginder, P. E. Wigen, A. J. Epstein, M. Angelopoulos, A. G. MacDiarmid, *Phys. Rev. Lett.* **60**, 2789 (1988).
- [16] M. Wohlgenannt, W. Graupner, G. Leising, Z. V. Vardeny, *Phys. Rev. B* **60**, 5321 (1999).
- [17] T. Drori, E. Gershman, C. X. Sheng, Y. Eichen, Z. V. Vardeny, and E. Ehrenfreund, *Phys. Rev. B* **76**, 033203 (2007).
- [18] E. Artacho, M. Rohlfing, M. Cote, P. D. Haynes, R. J. Needs, C. Molteni, *Phys.*

- Rev. Lett.* **93**, 116401-1 (2004).
- [19] Meng, H.-F.; Hong, T.-M. *Phys. Rev. B* **61**, 9913 (2000).
- [20] Cadby, A.; Dean, R.; Jones, R. A.; Lidzey, D. G. *Adv. Mater.* **18**, 2713 (2006).
- [21] Iyengar, N. A.; Harrison, B.; Duran, R. S.; Schanze, K. S.; Reynolds, J. R. *Macromol.* **36**, 8978 (2003).
- [22] D. A. Vanden Bout, W.-T. Yip, D. Hu, D.-K. Fu, T. M. Swager, P. F. Barbara, *Science* **277**, 1074 (1997).
- [23] G. He, Y. Li, J. Liu, Y. Yang, *Appl. Phys. Lett.* 2002, **80**, 4247.
- [24] T. W. Hagler, K. Pakbas, K. F. Voss, A. J. Heeger, *Phys. Rev. B* **44**, 8652 (1991).
- [25] S. Heun, R. F. Mahrt, A. Greiner, U. Lemmer, H. Bassler, D. A. Halliday, D. D. C. Bradley, P. L. Burn, A. B. Holmes, *J. Phys: Condens. Matter* **5**, 247 (1994).
- [26] E. J. Kramer, *Advances in Polymer Science* **52/53**, 1 (1983).
- [27] E. J. Kramer, L. L. Berger, *Advances in Polymer Science* **92**, 1 (1990).
- [28] R. P. Kambour, *J. Polym. Sci. Macromol. Rev.* **7**, 1 (1973).
- [29] A. M. Donald, E. J. Kramer, *Polymer* 1982, **23**, 457.
- [30] A. C.-M. Yang, E. J. Kramer, *J. Polym. Sci., Polym. Phys. Ed.* 1985, **23**, 1353.
- [31] A. C.-M. Yang, E. J. Kramer, C. C. Kuo, S. L. Phoenix, *Macromol.* 1986, **19**, 2020.
- [32] A. C. M. Yang, M. S. Kunz, J. A. Logan, *Macromol.* **26**, 1776 (1993).
- [33] J. H. Lin, A. C. M. Yang, *Macromol.* **34**, 3698 (2001).
- [34] C. H. Lin, A. C. M. Yang, *Macromol.* **34**, 4865 (2001).
- [35] C.-W. Lin, L.C. Huang, C.-C. M. Ma, A.C.-M. Yang, C.-J. Lin, L.-J. Lin, *Macromol.* **41**, 4978 (2008).
- [36] A. J. Epstein, A. G. MacDiarmid, "The controlled electromagnetic response of polyanilines and its application to technologies", p. 141 in W. R. Salaneck, D. T. Clark, E. J. Samuelsen (Eds.), *Science and Applications of Conducting Polymers*, Adam Hilger, New York, USA (1991)
- [37] U. W. Gedde, *Polymer Physics* (Chapman & Hall, London, 1995), Chap. 8.
- [38] J.-L. Bredas, R. Silbey, *Science* **323**, 348 (2009).
- [39] E. Collini, G. D. Scholes, *Science* **323**, 369 (2009).

Chapter 2: Dramatic Optoelectronic Enhancement Induced by Dewetting Ultrathin Conjugated Polymer Films

Abstract

The photoluminescent efficiencies of the light-emitting MEH-PPV molecules were found to have undergone an extraordinary enhancement when they were squeezed into ultrathin film with a thickness about 1 tenth of their molecular dimensions. This can be done by dewetting thin polymer films containing MEH-PPV molecules in which a residual layer about 3-5 nm thick developed in the retreated areas behind the dewetting fronts. These monolayer conjugated polymers emitted fluorescence with very high quantum efficiencies. The dewetting processes can be carried out by thermal annealing, solvent vapor imbibing, or in a multilayered thin film process. The photoluminescent characteristics accompanying the dewetting were explored and discussed. Finally, a light emitting diode was successfully fabricated based on this monolayer conjugated polymer.

Introduction

Organic optoelectronic devices [1-3] for energy or lighting have convincingly become one of the most promising solutions for a world facing stark challenges of commodity scarcity. At the core of this endeavor lies the perpetually advancing science and technology of conjugated polymers that have consistently brought in new breakthroughs paving venues to industrial successes. Recent noteworthy streaks of major discoveries have revealed the existence of strong effects of chain packing and conformation that may revolutionarily revamp the efficiency landscapes of polymer-based devices [4-10]. In the report herein, dramatically enhanced optoelectronic efficiencies of conjugated polymers were shown in monolayers in which the macromolecules were confined and severely sheared by a facile process of dewetting that may be fully compatible with the prevailing technologies employed in current semiconductor industries [11-15].

In further details, the molecular condensation to form ultrathin polymer films is controlled by solvent evaporation and the long-range van der Waals forces that dominate during the dynamic equilibrium. The way how the macromolecules are packed plays a very important role in determining how the conjugated polymer reacts to energy activation and dissipation. In an optoelectronic device, the fine structure of molecule packing and detailed segmental interactions at interfaces of neighboring layers control the pivotal charge injection process dictating the overall device efficiencies. Molecular recoiling upon heating or solvent vapor imbibing of these

confined macromolecules in the ultrathin films produced dewetting and new chain ordering via intermolecular or molecule- substrate interactions. The optoelectronic behavior of these oriented molecules provides unique opportunity to investigate the fundamental optoelectronic behavior of the 1D hydrocarbon chains. Particularly, the single-molecule behavior and the inter-molecule interactions may reveal the fundamental characteristics of individual chromophores and conversations between them. Advent in these frontier areas of conjugated polymers research will effectively shed important light on the development of organic optoelectronics for efficient lighting or harnessing energy through photovoltaic devices.

Experimental Section

MEH-PPV in the experiment was purchased from Sigma-Aldrich Chemical Co., with M_w 125,000~250,000 g/mol with polydispersity (M_w/M_n) around 5. Polystyrene was purchased from Pressure Chemical Co., $M_w = 2,032$, $M_w/M_n \leq 1.06$. A blend of solvents comprising equal parted toluene (HPLC/SPECTRO, TEDIA), THF (anhydrous, TEDIA), and cyclohexanone (GC grade, Sigma-aldrich) was used to dissolve the MEH-PPV polymer or mixture of MEH-PPV and PS. The solution was stirred slowly at 50°C for 12 - 24 hours and filtered (0.45 μ m pore size) to remove impurities in solution. The polymer solution was then spin-casted on 1 cm x 1 cm silicon wafer and glass. The film thicknesses, adjusted by changing the rotation speed of spin coating, were 20 and 40 nm. Bare silicon wafers, with a thin layer of native oxide, and glass cover slips were used for the substrate. For some experiments, the substrate was modified by precoating a thin layer of PDMS (polydimethylsiloxane, Sylgard 182, Dow Corning) via spin-coating of the toluene solution. The silicone coatings were then cured at 130°C for 25 minute. The thickness of silicone is around 3 nm for pure MEH-PPV film and smaller than 1 nm for MEH-PPV/PS film. The prepared film was protected from light by foil wrapping. Some samples used for this study were preared in a glove box (MBraun), but the testing results were idendtial to that of the samples prepared in the ambient conditions.

After being stored for 12 – 24 hours to allow for any residual solvent to evaporate, the films were annealed in a vacuum oven at a temperature between 100 - 130°C, during which the film morphological evolution and the luminescence spectra were monitored and recorded. Alternatively the dewetting experiments were carried out in a solvent vapor chamber (Figure 1a) with a fixed temperature (between 27 ~ 30°C) where the solvent molecules plasticized the film to generate similar effects as thermal annealing. Prior to the solvent imbibing, the air in the solvent chamber was evacuated first before solvent introduction. Optical microscope and atomic force

microscope was used to record the film morphological information. A fluorescence spectrometer (Perkin Elmer) and a time-resolved confocal microscope (PicoQuant) were used to measure the photoluminescence spectra. Photoluminescence mapping of the dewetted film was done by utilizing a scanning near-field optical microscope. In order to explore the thickness of the residual monolayer of dewetted films, x-ray reflectivity method using the synchrotron radiation (National Synchrotron Radiation Research Center, NSRRC, $\lambda = 1.54982 \text{ \AA}$) was employed.

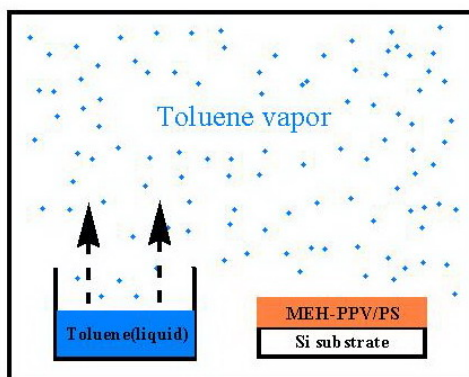


Fig. 1a Solvent chamber

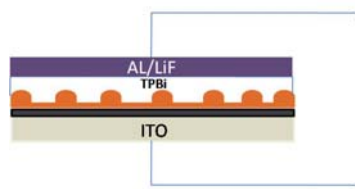


Figure 1b. Structure of the EL device

A light emitting diode was fabricated according to the structure shown in Figure 1b. The hole transport layer, PEDOT: PSS, Poly 3,4-ethylenedioxythiophene) poly(styrenesulfonate), was spin-coated on ITO glass. The MEH-PPV/PS film was then spin-cast on PEDOT, followed by solvent dewetting (80 minutes) and subsequent coating with TPBi and Al/LiF. Al/LiF was used as the cathode to measure the electroluminescence characteristics.

Results and Discussions

Ultrathin Polymer Films As-Deposited on Different Substrates

The ultrathin polymer films deposited on clean silicon wafer and glass slip shows different film morphology and luminescent efficiencies. Films of the same thickness (20 nm) were smooth on silicon wafer, but were defected with many small holes of an average depth around $2.7 \pm 0.2 \text{ nm}$ when deposited on glass slips (Figure. 2b). This difference was unlikely to be arising from the roughness difference of the two substrates (Figure 2a). Rather, it was due to the large difference between the electrostatic interactions (the Hamaker constants) between the polymer film surface and the substrate. For a positive Hamaker constant (such as the case of polymer on glass slips), dewetting of the viscous polymer films at the final stage of solvent evaporation during spin coating takes place to give rise to the formation of many shallow small holes.

The variation of dynamic equilibrium during film formation also generates large differences in molecular packing and chain conformation. That was illustrated in the large difference of luminescence intensity of the as-deposited films on these substrates. Given a same film thickness, the photoluminescent intensity of the films on the glass is almost three times than that of the films on glass (Figure 2b). Further depth of this subject is being explored.

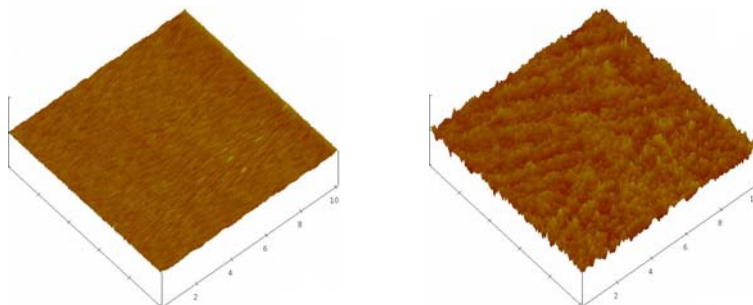


Figure 2a. AFM topography of silicon wafer (left) and glass slip (right).

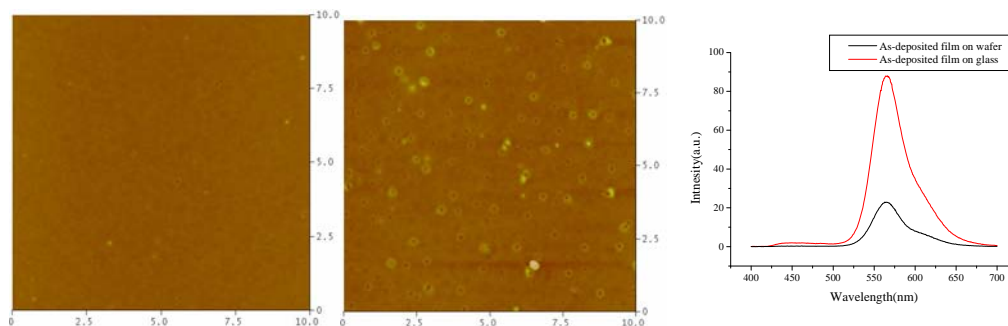


Figure 2b. AFM topography of the as-deposit MEH-PPV/PS thin films on silicon wafer (left: (roughness = 0.4 nm)) and glass slip (middle: roughness = 0.6 nm), and the PL spectra of both (right).

Dewetting on Different Substrates

As shown in Figure 3, the MEH-PPV/PS film (20 nm) on silicon wafer underwent dewetting when annealed at 100°C. During the long annealing time before the first set of incipient dewetting holes to appear, the polymer films roughened as a result of chain relaxation. The first set of holes emerged at 7.8 hrs, which progressively grew in sizes and transformed into interconnected ridges and then droplets. As will be shown later, large photoluminescence enhancement accompanied with the appearance of dewetting holes and droplets.

For films of the same thickness, it took even longer times to dewet on glass as compared to that on silicon wafers. This is disregarding the fact that these pre-existing shallow holes served as the nucleation sites for the dewetting instability. Due to the large number of these pre-existing holes, the numbers of droplets per area after

dewetting on glass are more than on that on silicon wafer (Figure 4). Correspondingly, the average sizes of the droplets (height of 111.0 ± 9.7 nm and diameter of 1.5 μm) were much smaller than that on silicon (average height of 263.0 ± 15.0 and diameter of ~ 6 μm). As will be shown in later sections, the residual layer left over from dewetting on the substrate developed following very different pathways. For instance, the sliding distance for forming these residual layers scaled reasonably as the inter-droplets distances, as inferred from the growth kinematics of dewetting holes. The inter-droplets spacing was about 14 μm , about 4 times of that (~ 3 μm) on glass, which translates to significantly larger difference in the actual strains of these residual layers. This provides an important explanation why the optoelectronic behavior of the residual layers is so different on these two kinds of substrates. Other contributions, such as the initial molecular packing in the as-deposit film, to the deformation and the optoelectronic behavior require further investigation.

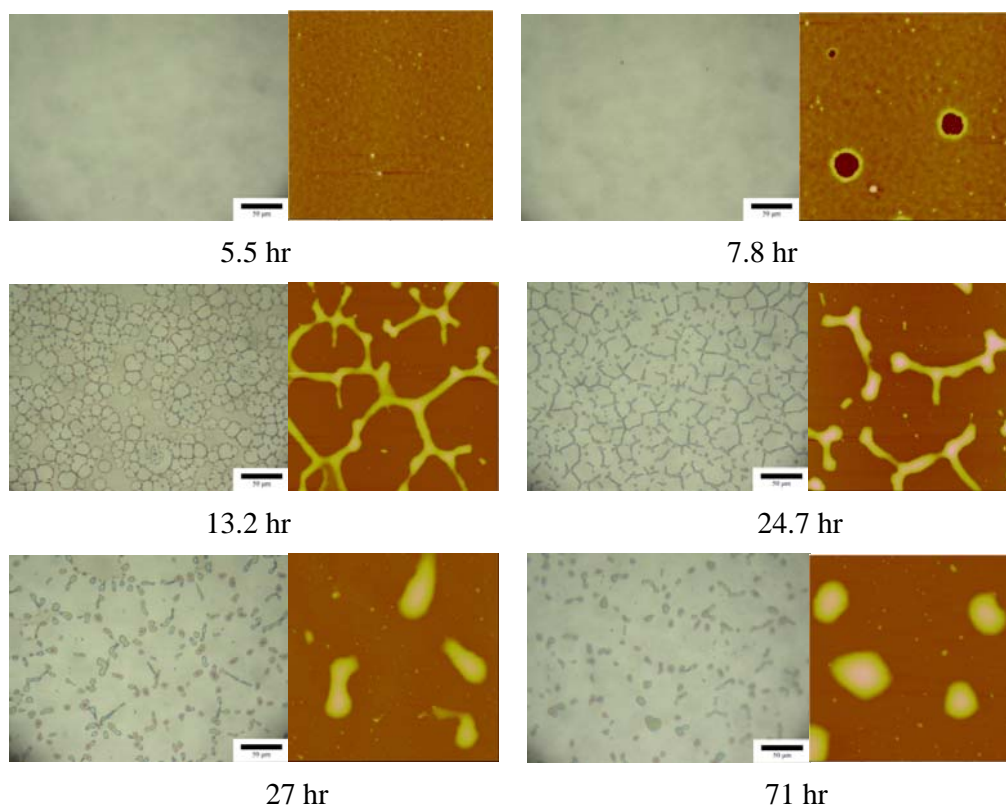


Figure 3. Optical and AFM micrographs of MEH-PPV/PS film dewetted on silicon wafer upon annealing at 100°C from 0 hr to 71 hrs.

In some situations where surface treatments may be desired to modify the surface property as related to dewetting, a thin silicone rubber was applied to these surfaces before spin coating the ultrathin polymer film. Generally speaking, the dewetting

became much faster, as shown in Figure 4 where incipient dewetting holes emerged at around 40 minutes annealing time, significantly shorter than 7.8 hours on silicon wafer. One important revelation from Figure 4 is the obvious coarsening of the droplets even after the islands had been well developed as shown by the variation from 150 minutes annealing time to 420 minutes. This indicates the existence of large scale mass transfer of the giant molecules over a length scale up to around 10 microns via the mechanical linkage of the residual layer of thickness around ~ 3 nm. This continuous evolution of the residual layer explains the further increase of the optoelectronic enhancement after island formation as will be reported in later sections.

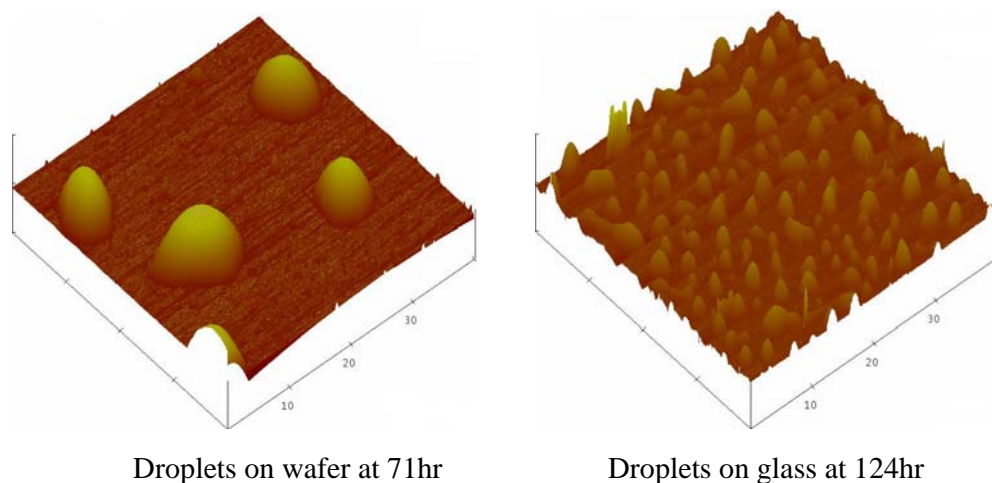


Figure 4. Dissimilar droplets patterns resulted on different substrates of the dewetted MEH-PPV/PS films.

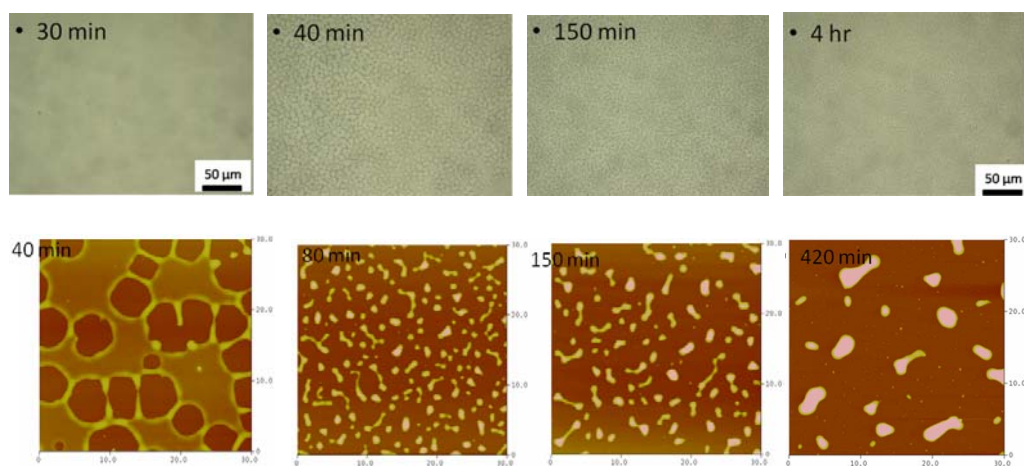


Figure 4. OM and AFM micrographs of the morphological evolution of MEH-PPV/ PS films on silicone coating over silicon wafer under thermal annealing.

Dewetting of Pure MEH-PPV Film

For pure MEH-PPV film (20 nm), it needed much longer times to dewet so we generally coated a thicker silicone layer (4-5 nm) on the substrate. The silicone coating, however, did not change too significantly the long range van der Waals interactions between the surfaces such that small pre-existing holes persisted in the as-deposited film. Figure 5a shows the dewetting process of the film on silicone-coated glass. The dewetting holes first emerged at around 12 hours annealing, which grew very slowly for about 21 hours and suddenly transformed into droplets at around 33 hours. As shown in Chapter 5, this is due to mechanical energy coupling between the polymer film and thick soft elastic substrate that gives rise to growth standstill of the holes and only when the polymer film had been fully relaxed the holes can start to grow again [16].

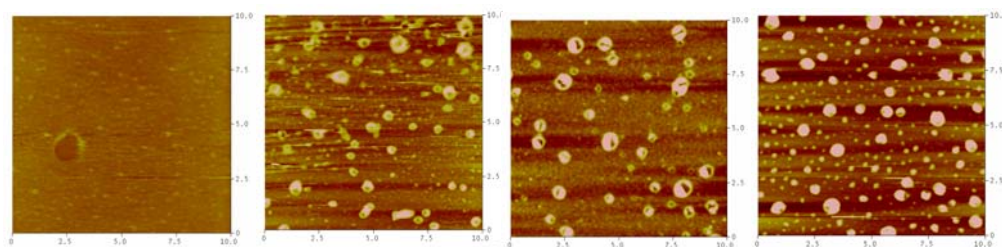


Figure 5a. The AFM images of the pure MEH-PPV film dewetted at 100°C. (a) 0hr (b) 12hr (c) 24hr (d) 33hr.

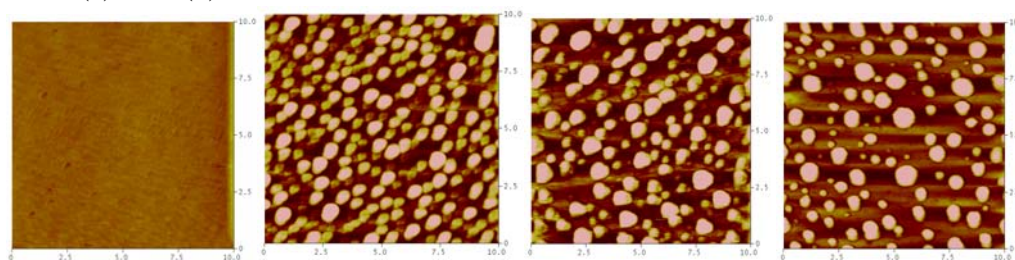


Figure 5b. The AFM images of the pure MEH-PPV film dewetted at 130°C. (a) 0hr (b) 1h (c) 4hr (d) 20hr

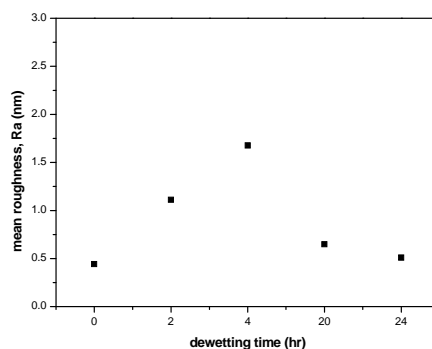


Figure 5c. The roughness of the pure MEH-PPV film (between droplets) during dewetting at 130°C.

To further accelerate the dewetting process, the annealing temperature was raised from 100°C to 130°C and the emergence of the dewetting hole hastened to less than 1 hour and the droplets suddenly formed subsequently (Figure 5b). The droplets continued to increase in sizes with increasing annealing time along with the decrease of film roughness (between droplets) as shown in Figure 5c.

On silicon wafer which was previously coated with a thin silicone layer (~ 1nm), the MEH-PPV film (20 nm) dewetted into numerous droplets (Figure 6) after 13 hours at 130°C.

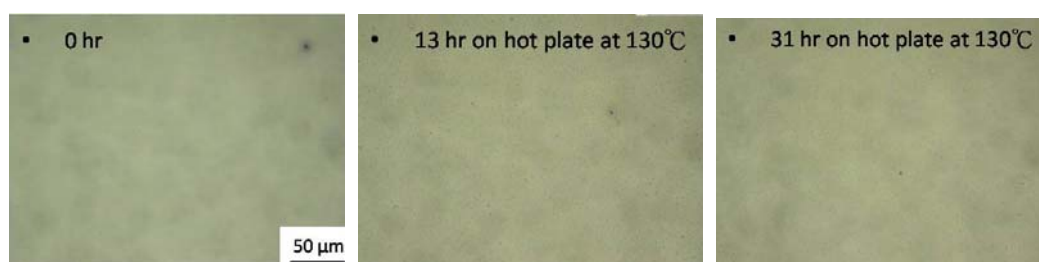


Figure 6. The OM micrographs of the dewetting MEH-PPV films at 130°C on thin silicone-coated silicon wafer.

Photoluminescence of Dewetted Films

Corresponding to the film evolution on Si wafers and glass slips arising from thermal dewetting shown in Figure 3, Figure 7 displays the PL spectra using 350 nm excitation. The main emission peaked at 565 nm for films on both substrates. After annealing the peak shifted to 585 nm and the PL intensity declined, consistent with the phenomenon of conjugated segments aggregation.[1,2]. The presence of inter-chain interactions in conjugated polymers can be revealed by measuring the PL excitation spectra and it was found that there are different excited states in the polymer films. As shown in Figure 7, the intensities of the 585 nm emission for films on both substrates remained weak even after long annealing times. The blue shift signals the decrease of conjugated length and may be attributed to separation, such as de-aggregation, of the MEH-PPV molecules.

Interesting enough, concurrent to the red-shift existed there a new emission at around 540 nm that caused a considerable progressive blue shift of the main emission. The emergence of this new blue shift peak accompanied with the appearance of dewetting holes. From the PL spectra, the enhancement factor on bare wafer and glass are totally different. The enhancement factor of wafer and glass are 5.47 and 1.52 respectively (Figure 7). As discussed in the previous sections, drastically different

strains accumulated in the residual films may account for the dissimilar enhancement behavior of the dewetting films on these two substrates.

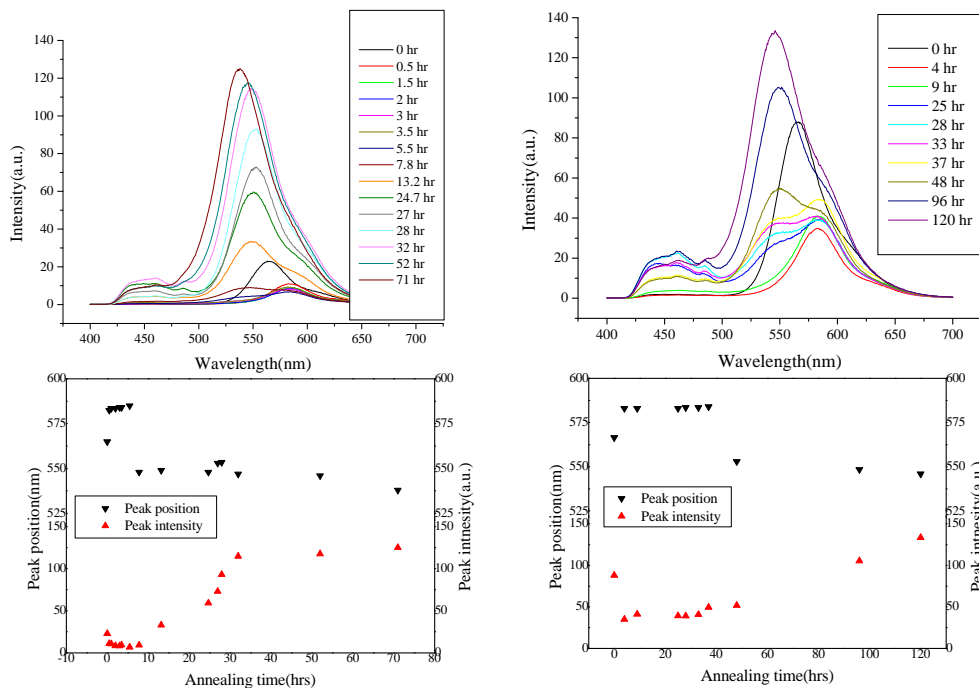


Figure 7. PL spectra of the film of MEH-PPV blended with PS on silicon wafer (left) and glass (right).

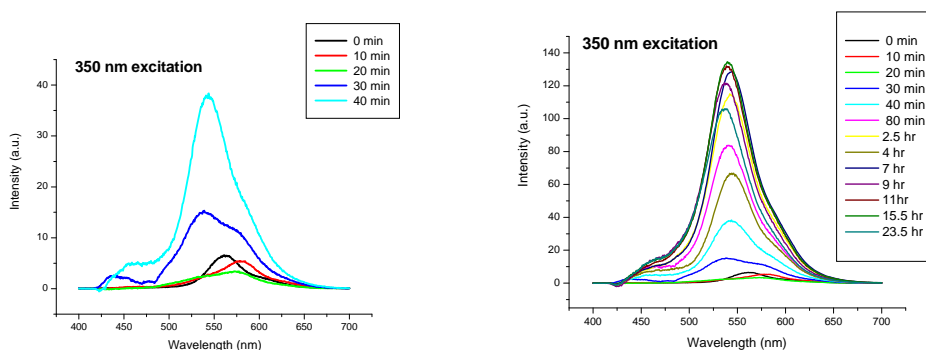


Figure 8. The shifts of main emission peak and its intensity as a function of annealing time for films on silicon wafers (left) and glass slips (right).

In a similar experiment but the silicon wafer was pre-coated with a thin layer of silicone, the variation of photoluminescence was similar to that shown in Figure 7 but the enhancement was about 20 times (Figure 8).

For pristine MEH-PPV films on silicon wafer precoated with thin silicone layer, the photoluminescence intensity varied with the progress of dewetting (130°C) following the same fashion as the MEH-PPV/PS film with an optical enhancement of

5 times as the main emission peak shifted from 585 nm to 535 nm (Figure 9). No red-shifts, however, were observed. This may be due to the fact that the as-deposited film emitted at 585 nm, the red-shifted wavelength of the blend films. This also indicated that annealing did not facilitate in the neat resin further chain aggregation that causes red shifts.

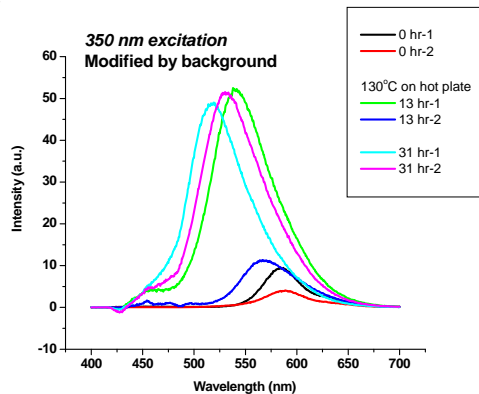


Figure 9. PL spectra of dewetting MEH-PPV film on Si wafers precoated with thin silicone.

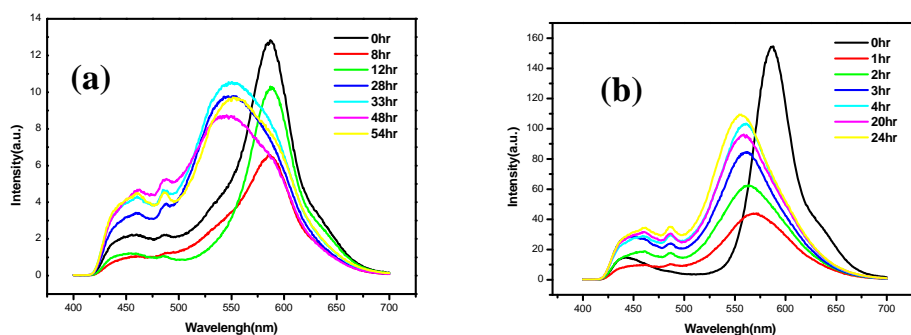


Figure 10. The PL spectra of MEH-PPV film annealed at (a) 100°C (b) 130°C for different dewetting time.

Dewetting of pristine MEH-PPV films (20 nm) on glass that was pre-coated with a thick silicone layer, the PL spectra varied similarly with that of MEH-PPV/PS on bare glass (Figure 10), but again without the red shift. The blue shifted emission, however, did not show enhancement, likely arising from the lesser degree of effective deformation of the fully relaxed polymer film at the substrate.

The Residual Monolayer

As clearly illustrated by the results shown above, the blue shifted emission arises from the development of holes during dewetting. Further investigation into the dewetted film had revealed that there exists an very thin layer of so-called “residual

film” behind the dewetting front (Figure 11, left depiction) resulted from severe shear of the thinning film by substrate friction under the influence of favorable long range van der Waals interactions. This thin layer, measured by AFM to be around 2 – 5 nm thick, adheres strongly to the substrate such that solvent dipping that dissolved the relatively large-sized droplets could not remove this monolayer.

Under a confocal microscope, this monolayer emitted light quite brightly when the focus condition was appropriate (Figure 11, right depiction).

Preliminary data of near field scanning optical microscope survey indicated strong luminescence emitting from the regions of holes (Figure 12).

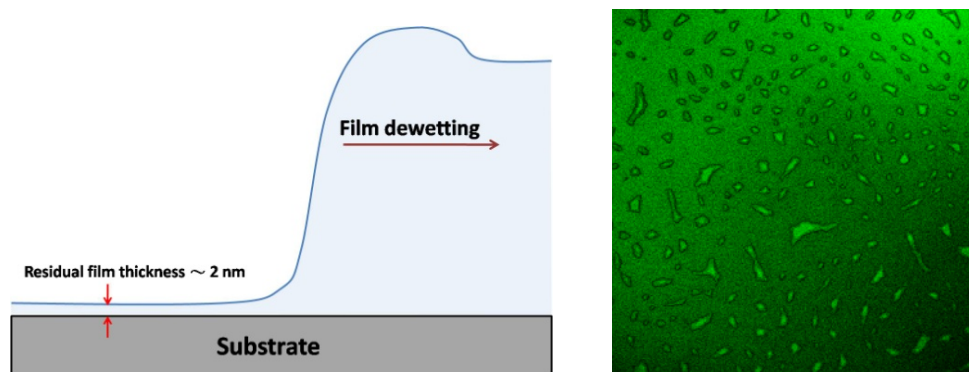


Figure 11. (left) Schematic drawing for the residual film and (right) confocal luminescent micrograph of dewetted films

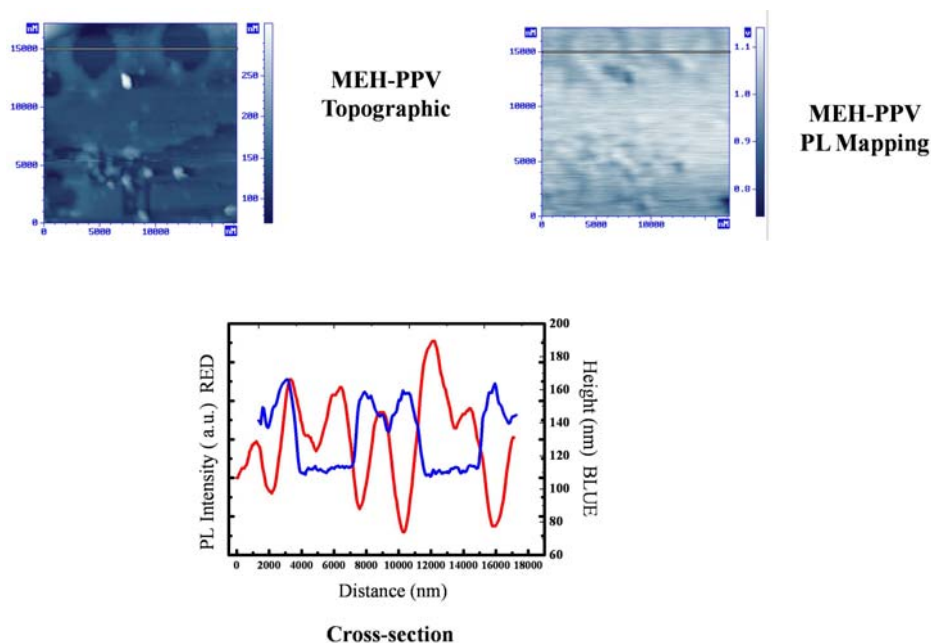


Figure 12. Scanning near-field optical microscopy of dewetted MEH-PPV film

The thickness of the residual MEH-PPV was further measured by x-ray

reflectivity using synchrotron radiation (Figure 13) with a multilayer fitting procedure. The thickness of the residual layer was found to be around 5 nm or 4 nm (Tables 1 and 2), respectively, for MEH-PPV or MEH-PPV/PS films, independent of film thickness.

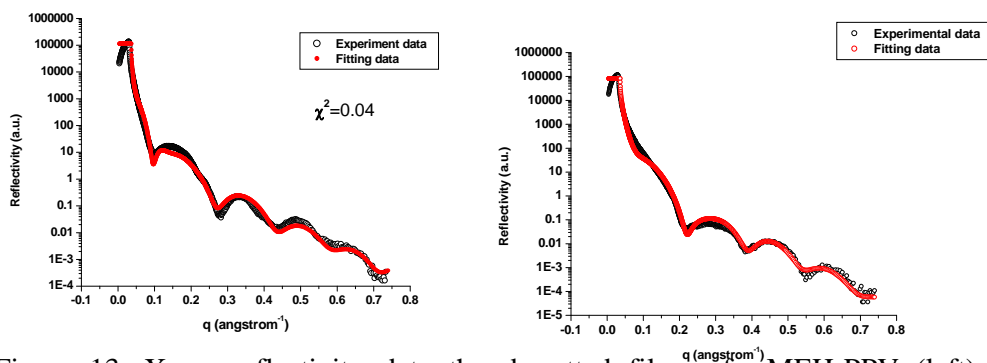


Figure 13. X-ray reflectivity data the dewetted films of MEH-PPV (left) and MEH-PPV/PS film (right).

Layer	Thickness (nm)	Roughness (nm)
MEH-PPV droplets	62.554	7
Residual film	5.5	1.5
Silicone	0.87733	0.2
Silicon oxide	3.5414	0.39273

Table 1. The fitting result of dewetted MEH-PPV film

Layer	Thickness (nm)	Roughness (nm)
MEH-PPV droplets	356.7	29.835
Residual film	3.9	0.34765
Silicone	0.19414	0.13
Silicon oxide	1.0701	0.2927

Table 2. The fitting result of dewetted MEH-PPV/PS film

Single molecule spectroscopy [8-10] was further used to investigate the luminescent characteristics of the conjugated polymer before and after dewetting. Ordinary single molecule conjugated polymer luminescence (Figure 14a, left) as compared to that after dewetting (Figure 14a, right) indicates that the large shear

extension significantly reduces the number of single molecules but the luminescence intensity of individual molecules increases dramatically. The luminescence lifetime also increases substantially in the dewetted sample (Figure 14, right) indicating that the phonon induced exciton annihilation is depressed by molecular confinement. Furthermore, while ordinary single molecule luminescence shows characteristic blinking (Figure 14c), the stretched single molecules do not demonstrate any blinking.

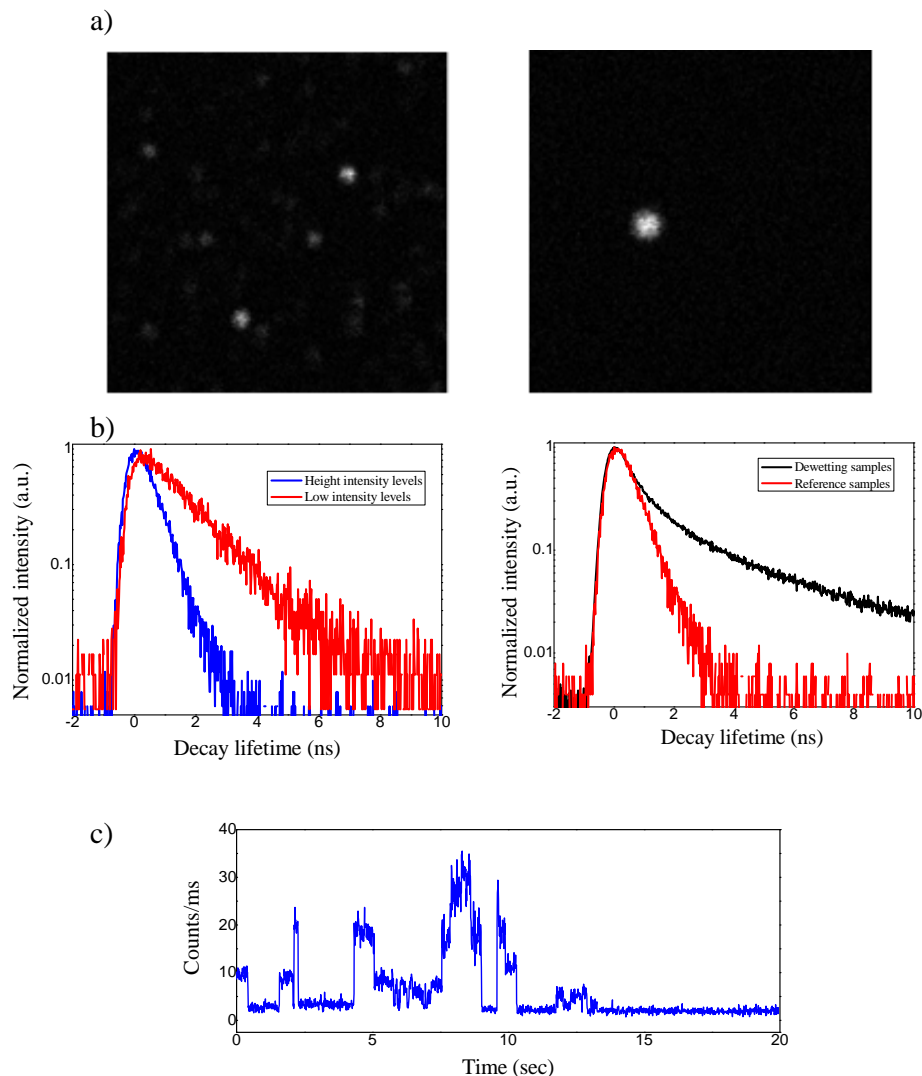


Figure 14. a) Single molecules emitting lights from the as-deposit film before dewetting (left micrograph) and the residual layer of the dewetted region (right micrograph). b) Decaying characteristics of the single molecule luminescence corresponding to a). c) Blinking of the MEH-PPV single molecule before dewetting. No blinking of the molecules in the residual film.

The deformation induced optoelectronic efficiencies are in excellent agreement with that observed in the plastic deformation zones (crazes) in glassy polymers, as reported in Chapter 1. The blue shifts observed in the dewetted films, which was

attributed to the decrease of the aggregate state of MEH-PPV molecules, are consistent with the large deformation accumulated in the residual films of long hole retreating distance.

“Solvent Dewetting”

The thin polymer films underwent dewetting in ambient temperatures when imbibing the solvent vapor (solvent annealing) [13-15]. Figure 15 shows the dewetting due to solvent annealing of the MEH-PPV and MEH-PPV/PS films (20 nm). The photoluminescent spectra of these “solvent dewetted” films demonstrated a behavior very similar to that observed in the thermal dewetted films. This indicates that dewetting of polymer ultrathin films by either thermal annealing or solvent annealing follows similar routes that a thin layer of residual molecules developed on the retreated surface. These highly sheared monolayers of conjugated polymer emit light with extraordinarily high optoelectronic efficiencies.

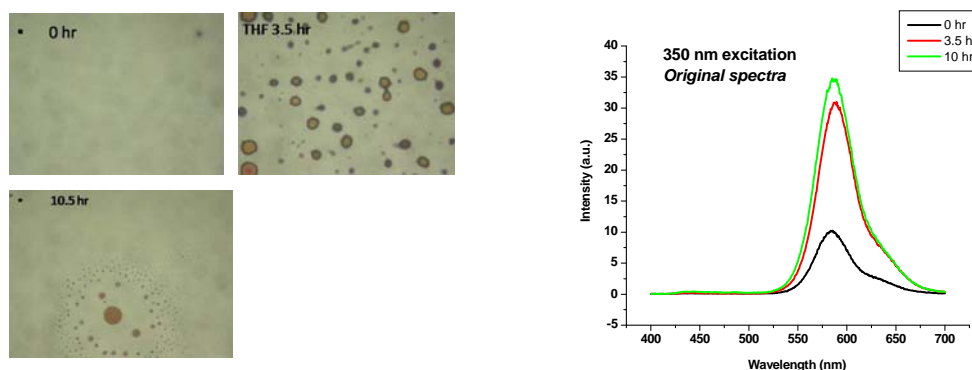


Figure 15a. Solvent vapor dewetted MEH-PPV film (a) OM images (b) PL spectra

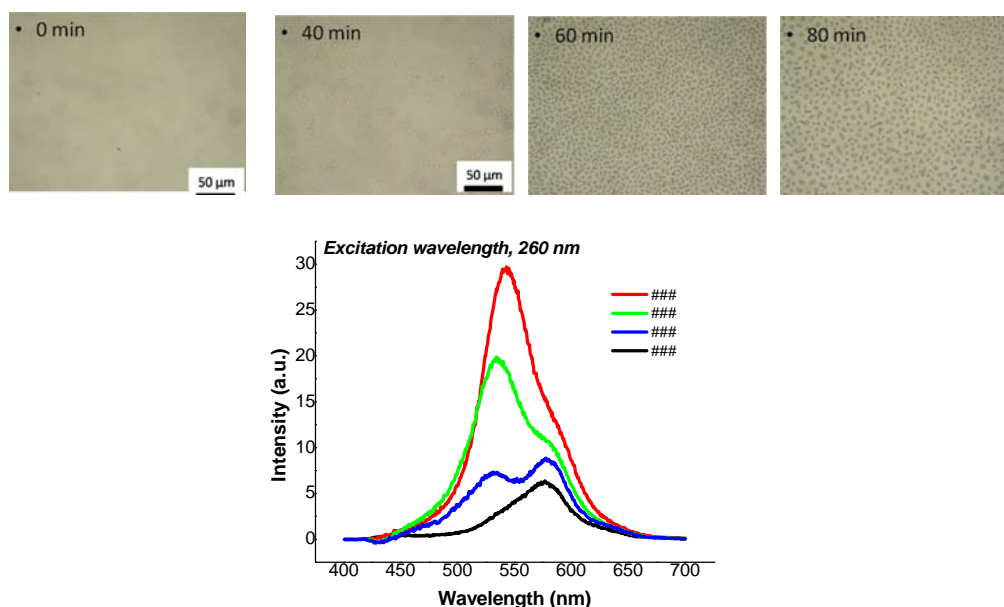


Figure 15b. Solvent dewetted MEH-PPV/PS film and their PL spectra.

Although these films that underwent solvent dewetting did show clear red shift, possibly due to smaller opening force operative during the layer-on-layer solvent dewetting, samples of diluted MEH-PPV in PS clearly demonstrated red shift upon first contact the solvent vapors. Figure 16 shows the spectra of 1% MEH-PPV in PS (MW = 2k) on the substrates of silicon wafer and glass slip. Clearly shown, the luminescence decreased progressively with the solvent vapor contact time, indicating that when the solvent contact the thin film, polymer chains would tend to relax and aggregate. This may change the conformation of polymer chains and also affect the conjugation length of chromophores. There are significant differences regarding the blue shift characteristics of the films on different substrates, which are being explored in the light of molecular packing as influenced by the substrate during spin coating.

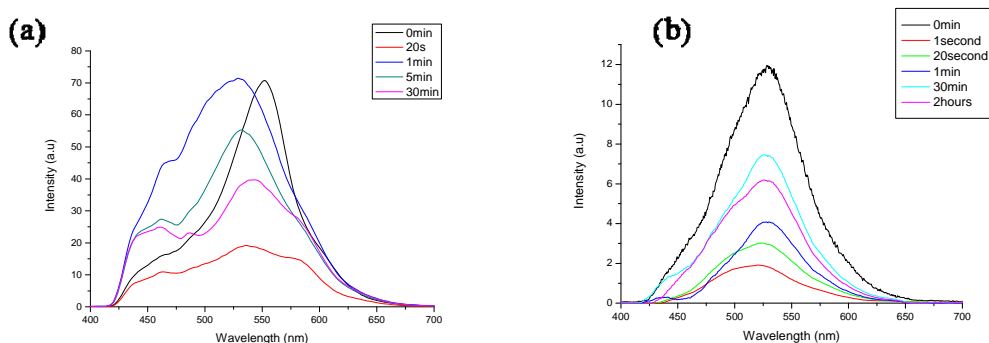


Figure 16. PL spectra of 1% MEH-PPV/99%PS film on silicon wafer (a) and glass substrate (b).

Multilayer Dewetting

Finally, a new experiment of multilayer dewetting was conducted to verify that ultrathin layer of “sheared” conjugated polymer can emit light several times of that in a relatively unstrained state. Samples were prepared by spinning a 5 nm thick MEH-PPV film on silicon wafer. Then, a 40 nm thick PS film of 200k molecular weight was prepared by spin coated on a glass slip, floated off the substrate on a water surface after overnight drying, and then picked up from the water surface to the 5 nm thick MEH-PPV film. The sandwiched sample underwent dewetting in a solvent vapor environment. As shown in Figure 17, identical photoluminescent was observed and a final optoelectronic enhancement factor of 14 times was obtained (Figure 17), confirming our stretch-induced mechanism for extraordinarily enhanced optoelectronic efficiencies for conjugated polymers.

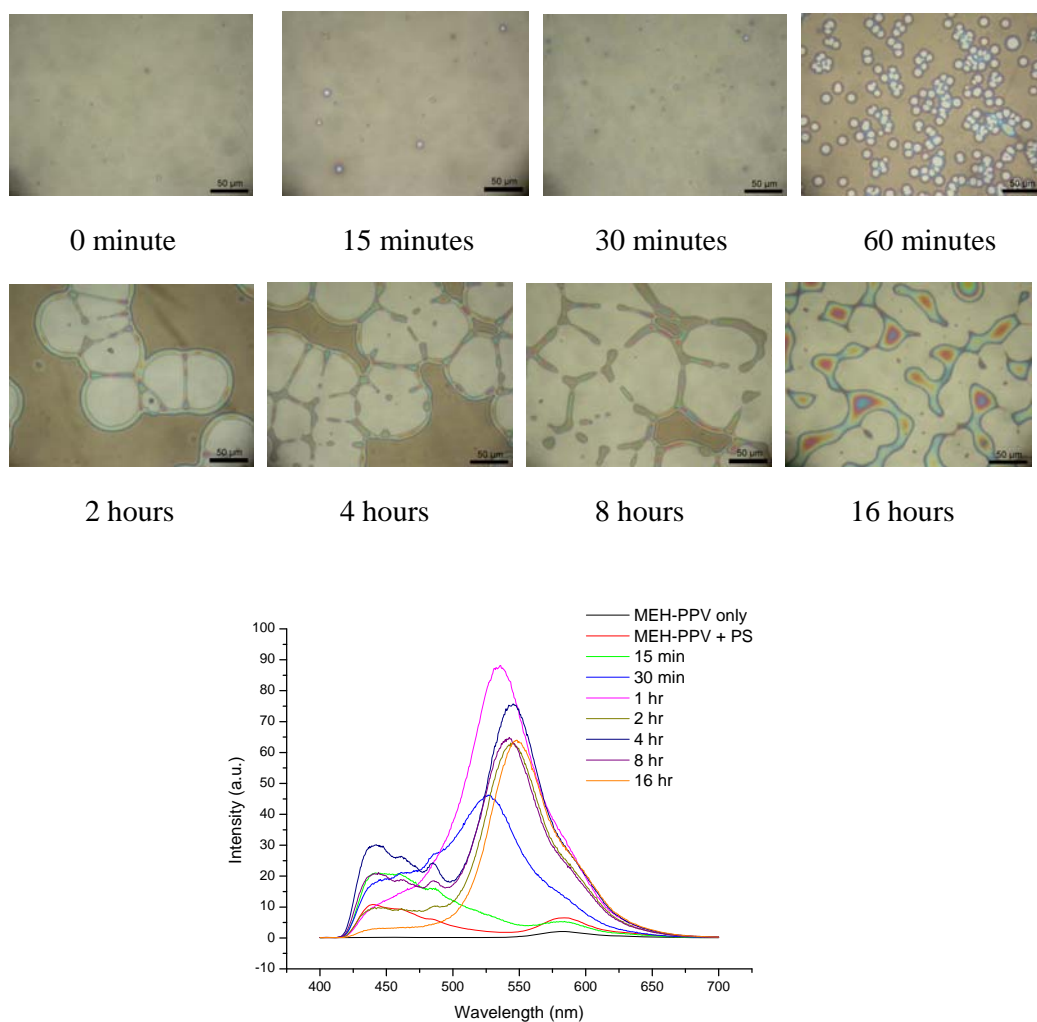


Figure 17. Dewetting of the multilayer samples and the PL spectra.

Electroluminescence Performances



Figure 18. Electroluminescence of devices based on the non-dewetted film (left) and the dewetted film (right).

Light emitting diodes were made from MEH-PPV/PS films before and after dewetting according to the structure depicted in Figure 1b. The MEH-PPV/PS film was transformed into droplets and the residual layer after 80-minute of solvent dewetting. Successful devices were made out of the dewetted film which clearly shows the blue shifts. This opens a new window, particularly along with the multilayer dewetting techniques, for feasible applications with extraordinarily high optoelectronic efficiencies of conjugated polymers.

Conclusions

The photoluminescent behavior of the light-emitting MEH-PPV molecules was found to have undergone a series of significant changes upon annealing when the molecules were dispersed in optically inert ultrathin polymer films. In the beginning, the major emission peak had red shifted slightly from 565 nm to 585 nm, with a pronounced decrease in intensity, which was contributed by the well-reported aggregation effect. As annealing time increased, the red-shifted peak continued to decrease until the dewetting holes emerged when the luminescence started to blue shift progressively, ultimately to 540 nm, accompanied with a dramatic intensity increase that may go as high as 20 fold. Almost identical behavior was observed in the dewetting processes induced by solvent vapor imbibing (solvent annealing). The large luminescence enhancement was found due to the development during dewetting of a residual monolayer (ca. 3 - 4nm) within which the conjugated polymer chains were severely sheared and confined to the substrate. A diversity of factors that demonstrated strong effects on the enhancement, such as the substrate Hamaker constant, interface rigidity, and the concentration of the conjugated molecules, pointed to the dominating influence of chain conformation within the residual monolayers on luminescence. Single molecule spectroscopy indicated that the luminescence intensity of the stretched molecules enhanced significantly along with the significantly increased lifetime. The blinking characteristics were also found to have vanished in the sheared molecules, indicating that excitons annihilation decreased substantially. The dewetting induced optoelectronic enhancement was compatible with current manufacturing processes and a simple light emitting diode based on the monolayer was successfully fabricated.

References

- [1] G. Gustafsson, Y. Cao, G. M. Treacy, F. Klavetter, N. Colaneri, and A. J. Heeger, *Nature* **357**, 477(1992).
- [2] D. Braun, A. J. Heeger, *Appl. Phys. Lett.* **58**, 1982 (1991).
- [3] M. Berggren, O. Inganäs, G. Gustafsson, J. C. Carlberg, J. Rasmussen, M. R.

- Andersson, et al, *Nature* **372**, 44 (1994).
- [4] G. He, Y. Li, J. Liu, Y. Yang, *Appl. Phys. Lett.* **80**, 22 (2002)
 - [5] T.- Q. Nguyen, V. Doan, B. J. Schwartz, *J. Chem. Phys.* **110**, 8 (1999)
 - [6] H.-L. Chou, S.-Y. Hsu, P.-K. Wei, *Polymer* **46**, 4967 (2005).
 - [7] G. He, Y. Li, J. Liu, Y. Yang, *Appl. Phys. Lett.* **80**, 4247 (2002).
 - [8] P. F. Barbara, A. J. Gesquire, S.-J. Park, Y. J. Lee; *Acc. Chem. Res.* **38**, 602 (2005).
 - [9] J. Yu, R. Lammi, A. J. Gesquiere, P. F. Barbara; *J. Phys. Chem. B* **109**, 10025 (2005).
 - [10] J. Yu, D. Hu, P. F. Barbara; *Science* **289**, 1327 (2000).
 - [11] G. Reiter, *Phys. Rev. Lett.* **68**, 75 (1992).
 - [12] M. H. Yang, S. Y. Hou, Y. L. Chang, A. C.-M. Yang, *Phys. Rev. Lett.* **96**, 066105 (2006).
 - [13] S. H. Lee, P. J. Yoo, S. J. Kwon, and H. H. Lee, *J. of Chem. Phys.* **121**, 4346 (2004)
 - [14] J. Zhu, J. Zhao, Y. Liao, and W. Jiang, *J. Polym. Sci.: Part B* **43**, 2874 (2005).
 - [15] L. Xue, Y. Han, *Langmuir* **25**, 9 (2009).
 - [16] S. Al Akhrass, G. Reiter, S. Y. Hou, M. H. Yang, Y. L. Chang, F. C. Chang, C.F. Wang, A.C.-M. Yang, *Phys. Rev. Lett.* **100**, 178301 (2008).

Chapter 3: Molecular Stresses in Metastable Ultrathin Polymer Films Prepared by Spin Coating

Abstract

The residual stress operative in thin films of a polymer (polystyrene) prepared by spin coating was determined from the local elastic stress release induced by nucleation of pinholes during the dewetting instability. The local stress was found to be independent of the position in the film and is orders of magnitude greater than the capillary force. It was attributed to entropy-driven chain recoiling of the confined macromolecules. The molecular deformation, approximately $\alpha \sim 5$ for thickness $\tau = 4$ nm, is large enough that it can only be described by the Langevin, rather than Gaussian, chain statistics. The effects of spin speed and aging-induced relaxation, as well as molecular packing were investigated. A unique dependence of the total molecular force versus τ reveals a broad minimal in the thickness regime from R_g to $2R_g$ corresponding to the minimal molecular layers in the ultrathin film. A molecular process dominated by the solvent evaporation and pinned boundary layer during spin coating is consistent with the observed behavior of molecular stress and chain deformation in the ultrathin polymer films.

Introduction

Polymer thin films are being used extensively and form the important basis for modern technologies. Recently, ultrathin polymer films (1 – 100 nm) have attracted broad interests because of the low costs and their enabling capabilities for a wide range of applications where surface properties play an important role [1-18]. The polymer thin coatings not only can provide specifically tailored optical, electrical, adhesive, frictional, and biological performances, but also are able to control surface reactions for important bio-, chemical, or physical events. Ultrathin films also are a convenient form for studying the fundamental behavior of macromolecule, in which the complicated processes, such as chain topological entanglements, crystallization, and exciton-phonon interactions, can be simplified and studied in-thorough in the reduced dimensions. Most of these films are prepared by solution cast via spin coating [19-29]. However, due to the fast solvent evaporation and the fast spinning action, the films so prepared are not in the thermal equilibrium and hence contain significant residual stresses. Despite the numerous papers that have revealed interesting observations of flow-induced molecular deformation [30-32] or that devoted to

empirical [22-24] or theoretical analyses [25-29] of the spin coating process, the molecular scenario that controls the chain conformation in the thin polymer films is still lacking. Thus, quantitative exploration of the residual stress and chain conformation is crucial for precise control of the thin film properties, which is prerequisite for any sensible investigations based on this type of systems.

For a long time, the force acting on thin polymer films was considered exclusively due to the capillary force, $\sim A/\tau^2$ (A : Hamaker constant; τ : film thickness) [9-13]. Only until recently when the entropy-driven molecular recoiling force, a unique feature of long chain molecules confined in reduced dimensions, was firstly recognized [14-18]. In this article, the molecular force acting in ultrathin polystyrene (PS) film was measured using a well defined micro-mechanical approach, in which the atactic PS serves as an ideal model system for all amorphous linear polymer chains. The residual force was found to be predominantly originated from recoiling of the confined long chain macromolecules and, in comparison, the capillary force can be neglected in this case. The molecular recoiling force was further revealed to be stable during an accelerated aging at 80°C up to 14 days, consisting with the assertion that chain movements in ultrathin polymer films were restricted by surface adhesion. The structure of the ultrathin film was examined by calculating the chain conformation using a general Langevin statistics. It was found that the total force exerting on the film manifests a broad minimum in the film thickness range of $R_g \sim 2 R_g$, corresponding to a mono-molecular layer structure in the film. From the observations, the dynamics of macromolecules during spin coating was revealed and a simple contact shear model can satisfactorily explains the observed polymer conformation in the film as solvent concentration varies.

Experimental Methods

Atactic monodispersed polystyrene (PS) thin films were used as a model system for amorphous linear macromolecules to study the residual stress and molecular deformation in the ultrathin films that are prepared by the spin coating method. The PS (Pressure Chemical Co., $M_w = 400,000$, $M_w/M_n \leq 1.10$) was used as received without further purification to make the coating solution in toluene solvent. PS thin films were cast on clean silicon wafer, normally, by using a fixed spin speed (4500 rpm) with the polymer concentration (c) adjusted to yield various film thicknesses (4 - 80 nm). Alternative series of PS films were prepared by varying the spin speed with fixed concentration c . The polymer concentrations used in the experiment, from 1.5 to 10.0 mg/ml, were significantly less than the critical concentration for semidilute solution ($c^* \sim 22\text{mg/ml}$). The film thickness was found to increase linearly with c (Fig.

2c, inset) [22] and for c less than a critical concentration c_0 (~ 0.8 mg/ml) perforated and porous coatings, instead of complete films, were obtained. When the films were dried in the ambient for 2 days, they were placed in an oven at 170°C for a series of time lengths to allow various extents of dewetting in the films to take place. The dewetted films were then examined under an optical microscope and an atomic force microscope (AFM). From the film topography, the underlying physics that govern the film behavior were investigated.

Results and Discussions

The PS films were spin coated from the dilute solutions where PS macromolecules were suspending isolated coils that were spread by the swirling actions during the spin coating and coalesced with one another in response to the rapid solvent evaporation to form continuous solid film. Hence, these films are non-equilibrated and forces exist in the films. Within a few minutes at 170°C , tiny pinholes were observed in the polymer film, a clear sign of the onset of dewetting. The distribution and growth of these tiny holes did not show any significant dependence on the locations in the film. This observation strongly indicates that the local stress in the ultrathin film is position-insensitive and r -independent. As a direct result of hole nucleation, local release of the in-plane elastic stress (σ) in the PS film took place to give a local thickness increase at around the hole edge and form a lumped structure (the crest) at the hole periphery (Fig. 1a), which, as will be shown later, can be used to analyze the released stress. The cross-sectional profile of the incipient hole is generally curved (Fig. 1c) with the surface angle generally less than 10° . The crest height (h) was found to increase linearly with the hole depth (D) up to the point of substrate contact ($D = \tau$) (Fig. 2a and 2b). The data also show that both the h - D dependence and the magnitude of h are approximately invariant of the dewetting time in the incipient hole growth. From this linear dependence, the polymer layer underneath the incipient hole is thus assumed to be unrelaxed and still subject to the original lateral stress ($p = \sigma_0$). By the same token, the subsequent growth of the newly created holes is also assumed to be independent of the depth of the hole, D , in this stage ($0 < D < \tau$). Laterally away from the incipient holes, the rest of the film is protected by the adhesion to substrate and hence can be assumed still under the original residual stress σ_0 provided that chain relaxation in the ultrathin PS film has not created significant variation in the chain conformation and the resulted stress; as will be demonstrated later in an aging experiment, this is a reasonable assumption at least in the incipient hole growth stage. For longer annealing times at the dewetting

temperature, substrate exposure occurred when the hole grew beyond the incipient stage ($\Delta = \tau$) and the influence of substrate surface tension began to participate. From this point on, frictional interactions between the PS film and substrate took place and the material removed from the hole region was transferred to edge of the hole, resulting a rapid increase of height at the hole edge (Fig. 1a). To differentiate from that due to elastic stress release, the local thickness increase around the edge of the hole from material pileup beyond the incipient stage was termed “rim”. Only the crest heights (δ s) obtained in the incipient stage were used to analyze the thin film stresses.

(a)

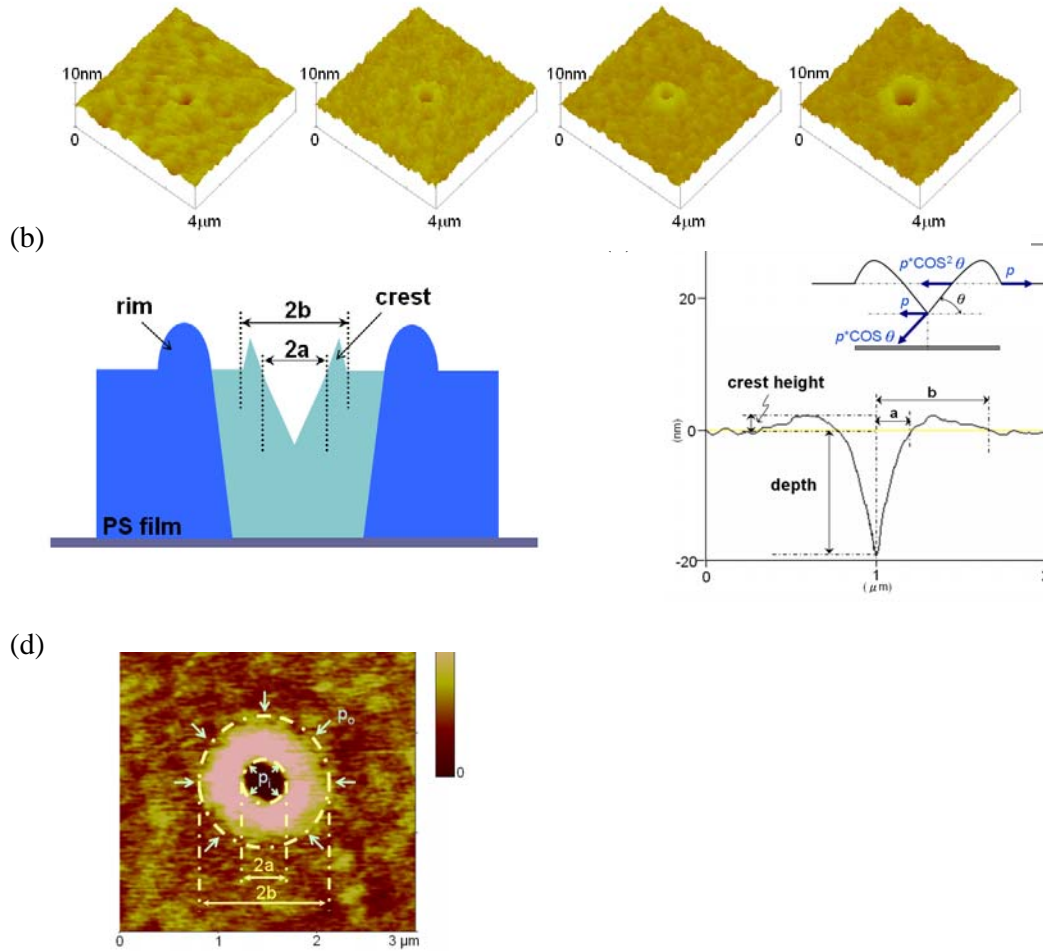


Fig.1. a) a series of AFM 3d topographic scanning of a growing incipient dewetting hole that shows a crest around the hole edge increasing with time (400k PS, 40 nm), b) a schematic drawing of an incipient dewetting hole (light-shaded area) and one that has grown to touch the substrate (dark-shaded area), c) cross-section of an incipient hole, and d) modeling showing the exertion of pressures p_0 and p_i on an incipient hole of an inner radius, a , and the outer peripheral radius, b .

Following Timoshenko [33], the stresses σ_r and σ_θ at the vicinities of a round hole under the influences of an external stress p_e and an internal stress p_i in a thin film under the plane stress condition ($\sigma_z = 0$) (Fig. 1d) can be expressed as

$$\begin{aligned}\sigma_r &= \frac{a^2 b^2 (p_i - p_e)}{(b^2 - a^2) r^2} + \frac{p_e b^2 - p_i a^2}{b^2 - a^2} \\ \sigma_\theta &= -\frac{a^2 b^2 (p_i - p_e)}{(b^2 - a^2) r^2} + \frac{p_e b^2 - p_i a^2}{b^2 - a^2}\end{aligned}\quad (\text{Eq. 1})$$

The assumption that $\sigma_z = 0$ is reasonable for ultrathin films and the outer radius b is recognized as the lateral limit beyond which the mechanical perturbation due to hole formation vanishes. The simple geometries shown in Fig. 1d indicate that the external stress p_e and internal stress p_i for an incipient hole during dewetting equal to σ_0 and $\sigma_0 \cos^2 \theta$, respectively. It is further observed that the Timoshenko equations are consistent with the boundary conditions of an incipient hole that $\sigma_r = \sigma_\theta = p_e = \sigma_0$ for $r = a = 0$ (before the onset of dewetting) and $r \geq b$ (far away from the hole).

Assuming linear elasticity, for a relaxed tiny layer (with thickness dD) in the polymer film, its contribution to the crest height at the hole edge, $d\delta$, will be related to the stress release ($\Delta\sigma_r + \Delta\sigma_\theta$) as

$$d\delta = \Delta e_z \cdot dD = \frac{-\nu}{E} (\Delta\sigma_r + \Delta\sigma_\theta) dD$$

where $\Delta\sigma_r = \sigma_0 - \sigma_r$ and $\Delta\sigma_\theta = \sigma_0 - \sigma_\theta$. For Δ 's sufficiently smaller than τ , the effect of adhesion may be neglected such that the material constants ν , E , and the stress release ($\Delta\sigma_r + \Delta\sigma_\theta$) are independent with the depth of the film. Further, at the edge of the hole ($r = a$), it can be shown from Eq. 1 that $\Delta\sigma_r = p_i - p_o = \sigma(\cos^2 \theta - 1) = \Delta\sigma_\theta$ and thus

$$d\delta = \frac{\nu}{E} [2\sigma_0 (1 - \cos^2 \theta)] d\tau = \frac{2\nu\sigma_0 \sin^2 \theta}{E} d\tau$$

It is reasonable to approximate that the molecular deformation of the confined chains in the ultrathin films is independent of z and thus the stress σ_0 is also z -independent. Therefore, under the previous assumption that film growth is independent of D , such that the total crest height δ is simply the integration of $d\delta$ over the whole thickness τ to be

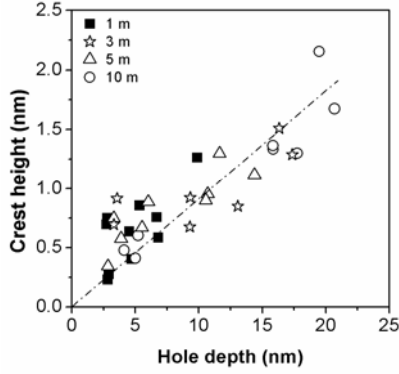
$$\delta = \frac{2\nu\sigma_0}{E} \int_0^\tau \sin^2 \theta dD$$

The integration requires detailed information of the cross-sectional profile of the

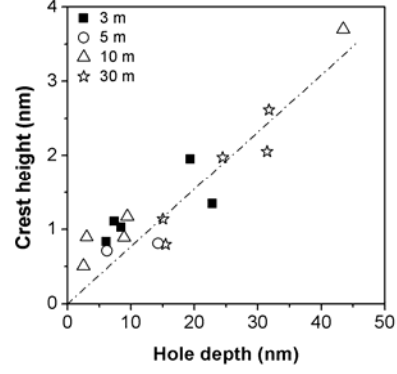
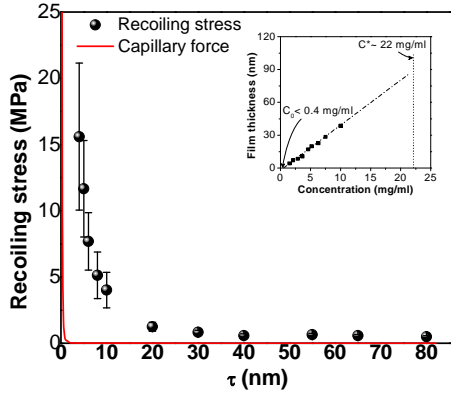
incipient holes and can usually be obtained readily from the AFM data. For the purpose of illustration, the angle θ is assumed to be a constant (independent of z) for each incipient hole and determined from $\tan^{-1}(D/a)$ or $\tan^{-1}(\tau/a_0)$. Then, the residual stress σ_0 can be related to and calculated from δ , d , and θ according to

$$\sigma_0 = \frac{\delta E}{2vd(1 - \cos^2 \theta)}$$

(a)



(c)



(d)

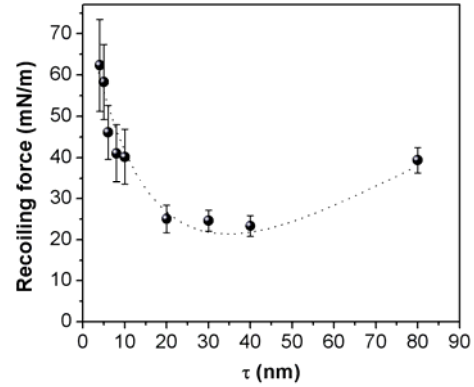


Figure 2. a,b) The crest height of an incipient hole increases linearly with hole depth for PS (400K) films of thickness of 20 and 40 nm for a) and b) respectively, c) The molecular recoiling stress σ_0 increases rapidly as film thickness decreases to below R_g , in comparison with the capillary force (in red line) calculated using a Hamaker constant $A = 10^{-20}$ J, and d) recoiling force $f \equiv \sigma_0 \tau$ as a function of film thickness τ .

Since the polymer film is rubbery at the dewetting temperature (170°C), we have $\nu = 0.5$ and $E = 0.2$ MPa obtained from the rubbery plateau¹⁹. Since the ratio (δD) is a constant up to $D = \tau$ (Fig. 2a and 2b), the crest height δ was conveniently taken from its value at $D = \tau$ for calculations of residual stress σ_0 . Furthermore, due to the fact

that the configuration of the film-substrate interface remains approximately unaffected during the incipient dewetting, the measured residual stress σ_0 is solely arising from the entropy-driven molecular recoiling and should be independent of capillary interactions. The molecular recoiling stress σ_0 obtained using a more detailed investigation of the cross-section θ , with a quadratic fitting of a with respect to D ($a \approx c''D^2 + c'D$) and $\theta \approx \tan \theta = dD/da$, was found to be slightly greater than that using the constant θ approximation. Since the difference in σ_0 is approximately within the same order of magnitude, the stresses obtained using the constant θ approximation were used to further investigate the chain conformation of the confined macromolecules in the ultrathin films.

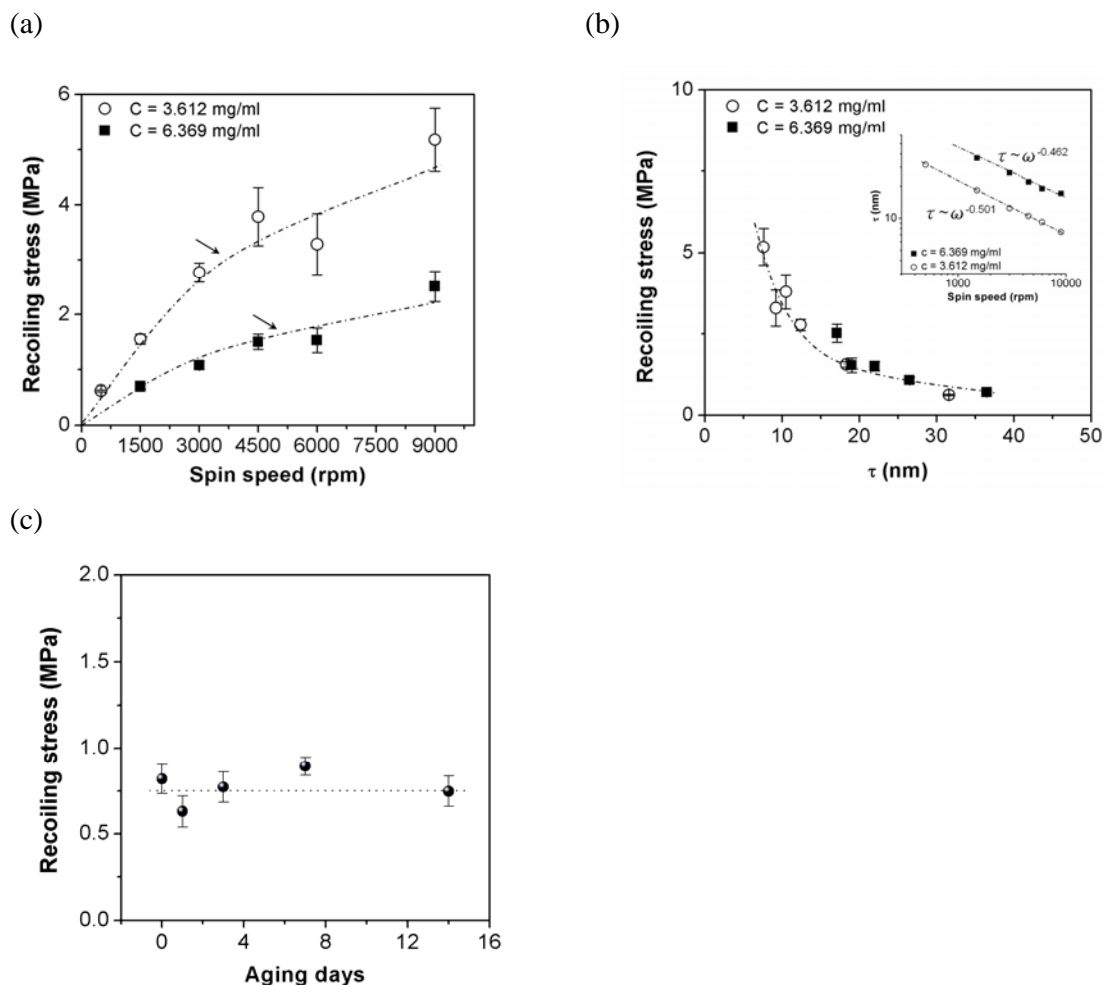


Figure 3. a) The recoiling stress increases almost linearly with the spin speed until it saturates at high speeds, b) A master curve can be drawn by plotting all the data acquired against film thickness, c) PS 400k, 30 nm, The molecular recoiling stress (in MPa) measured from incipient hole topography as a function of aging time at 80°C.

The molecular recoiling stress (σ_0) in the PS thin films was measured as a function of film thickness (Fig. 2c). For films of relatively large thickness ($> 2R_g$), the recoiling stress is very small. It, however, increases steadily as τ decreases, and finally rises rapidly when τ is below R_g (~ 17.32 nm) [34]. The molecular recoiling force f , obtained by multiplying σ_0 with film thickness τ , also decreases as τ increases, but rebound modestly for greater τ 's in response to the population increase of recoiling macromolecules in the solid film (Fig. 2d). The molecular recoiling force f in the PS film of 400k molecular weight is in the order of magnitude of 1 – 20 MPa. In comparison, the capillary force is much smaller (Fig. 2c). For $\tau = 10$ nm, for instance, the capillary force is approximately $2.7 \cdot 10^{-4}$ MPa, about 4 orders of magnitude smaller than σ_0 . Thus, the molecular recoiling force is clearly dominating in the polymer films of this thickness range.

The effects of spin speed and concentration were examined and the results are shown in Fig.3a. The recoiling stress increases almost linearly with the spin speed until it saturates at high speeds. Solutions of higher concentrations saturate at higher spin speeds. At the same spin speed, the recoiling stress is higher for the lower concentration solutions, indicating that molecular deformation is greater in the lower concentration solutions. A master curve can be drawn by plotting all the data acquired against film thickness (Fig. 3b).

The molecular recoiling stress was further examined by conducting an aging experiment where PS films (30 nm thick) were stored at 80°C for a series of time interval up to 14 days before growing the incipient dewetting holes for stress measurements. It was found that the molecular recoiling stress is essentially constant during the aging process (Fig. 3c). This is consistent with the observation that the crest heights versus hole depth is independent with the dewetting time as shown in Fig. 3. The results also are consistent with the aging relaxation experiments by Torkelsen and others [6-7] that molecule movements within the ultrathin dimensions are restricted.

The measured residual stress in the ultrathin PS film obviously is arising from the recoiling of macromolecules that are frozen in the film with chain conformations significantly deviated from thermal equilibrium. The “deformed” chain conformations were resulted from the work by the swirling force and quick solvent evaporation on the colloidal macromolecules in the cast solution during spin coating. As a first step to unveil the physical structure of the entangled chains in the ultrathin film and the molecular process involved during the solid film formation, the deformed chain

conformation was analyzed from the measured recoiling stress. From the film symmetry and equi-biaxial nature of the recoiling stress, it is fully reasonable to assume for the polymer chains a flattened conformation, obtained by uniaxially compressing the unperturbed chain in z -axis, with the volume conserved, such that after the deformation the molecular radius in the lateral direction ($R_{g,xy}$) is $\alpha \cdot R_g$ while in the z direction $R_{g,z}$ is $\alpha^{-2} \cdot R_g$ where α is the equi-biaxial draw ratio and R_g is the radius of gyration of the unperturbed coil. The draw ratio α can be related in a random-walk Gaussian statistics to the recoiling stress σ_0 by $\sigma_0 = 2\nu k_B T(\alpha - \alpha^{-5})$ where k_B is the Boltzmann constant and the entangled chain density ν is evaluated from $\nu = \rho N_{av}/M_e$, using the mass density ($\rho = 0.969 \text{ g/cm}^3$), entanglement molecular weight ($M_e = 13300 \text{ g/mole}$ [34]), and Avogadro number N_{av} , to be $4.38 \times 10^{25} \text{ chains/m}^3$. Although the draw ratio so obtained illustrates a rapid increase when film thickness τ decreases below R_g (Fig. 4a), it increased to an unreasonably large value of 29 for $\tau = 4 \text{ nm}$. Since the value of draw ratio has approached to the theoretical upper limit of ~ 40 for a fully stretched PS chain ($M_w = 400k$), the conditions for Gaussian chains approximation break down and hence the general Langevin statistics should be used to evaluate the actual molecular deformation. This can be done by multiplying the measured molecular recoiling stress σ_0 with the cross-sectional area (A_0) of a single chain segment of PS ($A_0 = 0.688 \text{ nm}^2$) [34,35] to yield the molecular force F exerting at the end of the macromolecule, from which the molecular dimension r (end-to-end distance) can be obtained via $L(\frac{Fl}{k_B T}) = \frac{r}{nl}$, where $L(x) = [\coth(x) - x^{-1}]$

is the Langevin function. The molecular deformation obtained by using this general chain statistics manifests a functional dependence on τ qualitatively similar to that by the Gaussian approximation but with much reasonable draw ratios (Fig. 4a). The α of the confined polymer chains in ultrathin films of 4 nm is approximately equal to 5, very similar to that in a craze where the fibril dimensions is similar to the film thickness here [36-39]. A master curve of α versus τ is obtained, as shown in Fig. 4b.

The verdict that Gaussian chain statistics is not followed by the macromolecules confined to the ultrafilms may pose a sharp contrast to the previous published results based on scattering experiments of SANS or SAXS. The latter, however, are burdened with difficulties associated with sample preparation and data collection of ultrathin films [2-5] therefore, are generally not able to probe films with thickness much less than the unperturbed dimensions.

The packing of entangled chains in the ultrathin film was investigated by determining the number of molecular layers, n , for constructing the film. It was determined by dividing the film thickness τ with the $R_{g,z}$, as obtained from the measured molecular recoiling stress using the Langevin statistics. By doing so, we

implicitly assumed that the mass density (ρ) in the polymer films is independent of film thickness. The packing number n was found to be around unity in the broad thickness regime from 20 to 40 nm, roughly corresponding to $R_{g,z}$ to $2R_{g,z}$, or approximately R_g to $2R_g$ (Fig. 4c). Away from this thickness regime, n increases mildly to 1.8 as τ increases to 80 nm. In the other direction, n increases much more rapidly to around 3 as τ decreases to 4 nm. Considering the constant θ approximation used for the calculations, the result of $n = 1$ in the broad minimum between $R_{g,z}$ and $2R_{g,z}$ is fortuitous. The overall behavior depicted in Fig. 4c, however, is not and in fact reveals important clues of the molecular process during the formation of solid films.

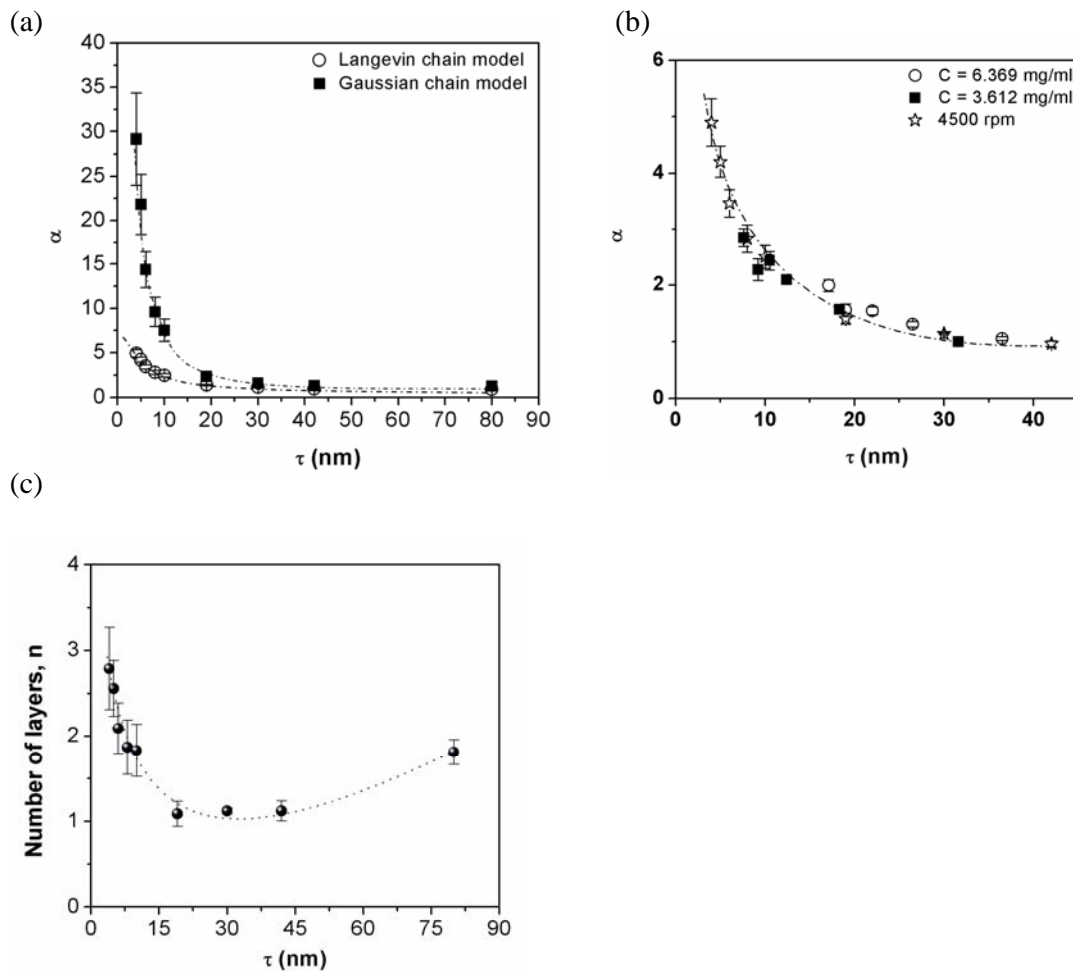


Figure 4. The molecular draw ratio of the confined chains in the ultrathin films PS chains as a function of film thickness τ calculated by using either a Gaussian chain model or a Langevin chain model, b) a master curve can be obtained for α vs. τ for all data collected here for PS macromolecules, and c) The number of molecular layers packed in the PS thin films.

The complicated microscopic processes during spin coating of polymer solutions have been studied extensively but a clear molecular scenario is still not available. Among the many factors that are linked to spin coating, the mechanical actions arising from the spinning substrate and that of the quick solvent evaporation probably are the two most prominently recognized driving forces for the formation of the polymer thin films [22-24]. The former creates a centrifugal force and a shear, acting respectively along the radial r and tangential θ directions, before solvent evaporation transforms the spun solution into a glassy film. The centrifugal force, proportional to $\rho\omega^2 r$ where ρ is the mass density of the solution and ω the angular spin speed, however, is a small force, around 3×10^{-2} Pa for 1 mm thick polymer solution at $r = 5$ mm, that can only accounts for the uniform outward spreading of the solution during initial spinning but is impossible to inflict significant molecular deformations that are consistent with the measurements here. The shear force arising from the large relative linear velocity at the substrate surface may be large enough for appreciable molecular deformation, it, however, is r -dependent [40-41] and contradiction will arrive to the observation of r -independent molecular recoiling forces in spin-coated polymer films if the shear force is treated as the driving force for the large molecular deformation.

As strongly suggested by the dependence of α versus τ (Fig. 4b), solvent evaporation may have played a dominant role during the film formation process. Although the shear force induced by substrate spinning is r -dependent, the boundary layer thickness h is not. The notion of the boundary layer is more than century-old but its exact analytical description is still absent. Nevertheless, it is required to satisfy the boundary condition that the fluid velocity at the interface on a solid that moves with a large relative velocity must be stationary. Using the Prandtl-Blasius approximation [40,41], the thickness h can be approximated as $h \sim 5(\mu x / \rho v)^{1/2}$ where the travel distance x and linear velocity v are both proportional linearly to r and hence leaving h r -independent (μ is the solution viscosity). The shear-dominant boundary layer pins an equilibrated polymer solution at the substrate surface and the excess of the polymer solution that are not sufficiently engaged with the substrate are spun off easily. Although the shearing force clearly may produce large deformations to the anchored solution, since the polymer molecules in the solution are isolated coils ($c < c^*$) and are much “denser” or “harder” than the pure solvent, the solvent phase absorbs most of the shear deformation and leaves the molecular coils relatively un-sheared. It is the later solvent evaporation that takes place in the anchored layer introduces large molecular deformations by rapidly extracting the solvent molecules from the polymer coils. With the large frictional force operative between the polymer chains and the substrate, the solvent extraction may be so fast that polymer coils ($\sim c^*$) cannot recoil congruently and thus create large lateral molecular extensions α 's. As a

reference, for a monolayer of polymer solution of concentration c^* , in which the chain density is approximately 1/33 of the bulk value [34], the molecular deformation α should be roughly $(33)^{1/2} \sim 5.7$ if molecular recoiling during solvent extraction is ignored. Clearly, this is the same order of magnitude of the molecular deformations obtained by our study here.

With this new molecular scenario of spin coating, the effects of polymer solution (Fig. 2c, inset) and spin speed (Fig. 3a) can be easily comprehended. They can be examined and analyzed from the angle of an equilibrated anchored layer of which the thickness and chain concentration are dependent on the initial polymer concentration in the solution and the spin speed. The universal dependence of α versus τ can also be fully explained.

In summary, the residual stress in polymer thin film prepared by spin coating can be measured by analyzing the local stress release from the nucleation of pinholes induced by dewetting. The stress is orders of magnitude greater than the capillary force, conventionally regarded as the dominant force in ultrathin films, and is attributed to the recoiling of the confined long chains from the chain conformations significantly deviated from that of unperturbed state to that of thermal equilibrium. The stress increases significantly as the film thickness becomes smaller than the unperturbed molecular dimension. The chain conformations in these films can only be described by the Langevin, rather than Gaussian, statistic and were determined to be $\alpha \sim 5$, similar to that in craze fibrils, for thickness $\tau = 4$ nm. The effects of spin speed and aging-induced relaxation, as well as molecular packing were investigated. A broad minimal of the total operative force was found in the thickness regime from R_g to $2R_g$ that corresponds to minimum number of molecular layers in the film. Based on the observed behavior of the spin-coated ultrathin films, a molecular process where solvent evaporation interplayed with a shear-dominated boundary layer scenario is proposed to be responsible for the observed molecular stress and chain deformation.

References:

- [1] G. Reiter and P. G. deGennes, *Eur. Phys. J. E*, 2001. **6**: p. 25.
- [2] C. W. Frank, V. Rao, M. M. Despotopoulou, R. F. W. Pease, W. D. Hinsberg, R. D. Miller, J. F. Rabolt, *Science* 1996, 273, 912.
- [3] T. Russell 1996
- [4] J. Kraus, P. Müller-Buschbaum, T. Kuhlmann, D. W. Schubert, M. Stamm, *Europhys. Lett.*, **49**, 210 (2000)
- [5] T. Kaijama, Y. Oishi, *Trends Polym. Sci.* **3**, 30 (1995)

- [6] R. D. Priestley, L. J. Broadbelt, J. M. Torkelson, *Macromol.* 2005, 38, 654. R. D.
- [7] Priestley, C. J. Ellison, L. J. Broadbelt, J. M. Torkelson, *Science* 2005, 309, 456.
- [8] Z. Fakhraai, J. A. Forrest, *Science* 2008, 319, 600.
- [9] G. Reiter, *Phys. Rev. Lett.*, 1992. **68**: p. 75.
- [10] K. Jacobs, S. Herminghaus, and K.R. Mecke, *Langmuir*, 1998. **14**: p. 965.
- [11] G. Reiter and R. Khanna, *Phys. Rev. Lett.* , 2000. **85**: p. 2753.
- [12] R. Seemann, S. Herminghaus, and K. Jacobs, *Phys. Rev. Lett.*, 2001. **86**: p. 5534.
- [13] J.L. Masson, P.F. Green, *Phys. Rev. Lett.*, 2002. **88**: p. 205504-1.
- [14] G. Reiter, M. Hamieh, P. Damman, S. Slavons, S. Gabriele, T. Vilmin, E. Raphael, *Nat. Mater.*, 2005. **4**: p. 754.
- [15] M.H. Yang, S. Y. Hou, Y. L. Chang, A.C.-M. Yang, *Phys. Rev. Lett.* 2006, **96**, 066105.
- [16] T. Vilmin and E. Raphael, *Phys. Rev. Lett.* 2006, **97**, 036105.
- [17] P. Damman, S. Gabriele, S. Slavons, S. Desprez, D. Villers, T. Vilmin, E. Raphael, M. Hamieh, S. A. Akhrass, G. Reiter, *Phys. Rev. Lett.* 2007, **99**, 036101.
- [18] S. Al Akhrass, G. Reiter, S. Y. Hou, M. H. Yang, Y. L. Chang, F. C. Chang, C.F. Wang, A.C.-M. Yang, *Phys. Rev. Lett.* 2008, 100, 178301.
- [19] A. G. Emslie, F. T. Bonner, L. G. Peck, *J. Appl. Phys.* 1958, 29, 858.
- [20] D. Meyerhofer, *J. Appl. Phys.* 1978, 49, 3993.
- [21] D. W. Schubert, T. Dunkel, *Mat. Res. Innovat*, 2003, 7, 314.
- [22] C. J. Lawrence, *Phys. Fluids* 1988, 31, 2786.
- [23] D. P. Birnie III, M. Manley, *Phys. Fluids* 1997, 4, 870.
- [24] P. C. Sukaneck, *J. Electrochemical Soc.* 1991, 138, 1712.
- [25] F. Kremer, L. Hartmann, A. Serghei, P. Pouret, L. Leger, *Eur. Phys. J. E*, 12, 139 (2003)
- [26] B. Reisfeld, S. G. Bankoff, S. H. Davis, *J. Appl. Phys.* 1991, 70, 5258.
- [27] B. S. Dandapat, P. Daripa, P.C. Ray, *J. Appl. Phys.* 2003, 94, 4144.
- [28] L. W. Schwartz, R. V. Roy, *Phys. Fluids* 2004, 16, 569.
- [29] T. Ohara, Y. Matsumoto, H. Ohashi, *Phys. Fluids A* 1989, 1, 1949.
- [30] T. T. Perkins, D. E. Smith, S. Chu, *Science* 1997, 276, 2016.
- [31] D. E. Smith, H. P. Babcock, S. Chu, *Science* 1999, 283, 1724.
- [32] P. Tapadia, S. Ravindranath, S.-Q. Wang, *Phys. Rev. Lett.* 2006, 96, 196001.
- [33] S.P. Timoshenko and J.N. Goodier, *Theory of elasticity*. 3d ed. 1969, c1970: New York, McGraw-Hill.
- [34] M. Rubinstein and R.H. Colby, *Polymer physics*. 2003: Oxford University Press, New York.
- [35] C.W. Lin, L. C. Huang, C.-C. M. Ma, A. C.-M. Yang, C.-J. Lin, and L.-J. Lin, *Macromol.* 2008, 41, 4978.

- [36] A. C.-M. Yang, E. J. Kramer, J. Mater. Sci., 1986, 21, 3601.
- [37] A. C.-M. Yang, E. J. Kramer, J. Polym. Sci.: Polym. Phys. 1985, 23, 1353.
- [38] A. C.-M. Yang, M. S. Kunz, and J. A. Logan, *Macromolecules* 1993, **26**, p1767.
- [39] J. H. Lin, A.C.-M. Yang, *Macromolecules* 2001, **34**, 3698 –3705.
- [40] H. Schlichting, Boundary Layer Theory, 8th Edition, McGraw-Hill, New York, 2000.
- [41] L. Rosenhead, Laminar Boundary Layers, Oxford University Press, London, 1963.

Chapter 4: Metastable Ultrathin Polymer Films

Part A: Relaxation of the Large Residual Stress in Ultrathin Polymer Films

Abstract:

The main purpose of this work was to investigate the molecular instability of long polymer chains confined in viscoelastic ultra-thin films (thickness = 1~100 nm). Models systems prepared by spin-coating of the polystyrene ($M_w = 90$ kg/mol.) thin films (10, 40nm) supported on two different substrates of bare silicon wafer and the silicon wafer coated with thick SiO_x (100nm). These films, driven by the residual molecular recoiling stress and long range van der Waals interactions, underwent a dewetting rupturing process when annealed to form tiny droplets on substrate. By recording the variations of the incipient hole's morphological features, the elastically released molecular recoiling stress was measured. The molecular recoiling stress was found to decrease exponentially with time when aged at 110°C , a temperature slightly higher than T_g of the bulk, but showed no changes at 80°C and 90°C (slightly below the bulk T_g). The film instability also revealed a significant dependence on substrate Hamaker constant in that on attraction substrates (Hamaker constant > 0) the films not only had better stability but also had slower stress relaxation rate. In this case, the large pre-existing molecular recoiling stress would relax upon prolonged annealing such that incipient dewetting holes healed ultimately. For the relaxed films where the elastic stress release measurements were difficult to carry out, the local stress relaxation was estimated via a Maxwell model from temporal local topographic changes. The derived viscosity, despite of the increasing recoling force, increased strongly as film thickness decreased, indicating the important influences of interfacial bonding (adhesion and friction) to the chain motions in ultrathin polymer films.

Introduction:

When the polymer thin film's thickness is less than 100 nm, the fundamental properties of polymer chains vary remarkably as compared to the bulk. Specifically, most of the ultrathin polymer films were prepared by spin-coating during which solvent evaporate quickly, compelling the the polymer chain to contract or inter-penetrate in order to maintain the pressure balance in the ambient conditions. This produces a frozen state of the polymer chains in which the molecular coils are substantially stretched and a large residual stress develops in the thin film [1]. Upon annealing at a higher temperature than T_g when the polymer chain attain enough

kinetic energy to return to the thermal equilibrium state, the chains recoil and drive the dewetting phenomenon initiated from defects of the film [2,3]. The molecular recoiling stress can be calculated from

$$p = \frac{E\delta_0}{2\nu\tau \sin \theta}$$

where E is Young's modulus, δ_0 is max crest height, ν is Poisson's ratio, τ is film thickness, and θ is surface angle of the dewetting holes [4]. Generally, the dewetting process consists of several steps. First, incipient holes emerge at some locations of the film upon annealing. Then, the holes grow in sizes to expose the underlying substrate and simultaneously laterally expand to connect with each other. Interconnected ridges thus form and subsequently break down by Rayleigh instability to form droplets on the substrate [5-17]. This process is driven by the molecular recoiling force as well as by the long range van der Waals interactions operative in the film. The dewetting process may stop or even reverse when stress relaxation takes place in the film. This is the main subject to be explored and reported here.

Experimental Procedures:

In this study, we choose the polystyrene as the solute, with molecular weight of 90,000 g/mol. The solvent is toluene, the substrate is Si wafers, and SiO_x coated wafers. After the solvent and polymer were mixed and filtration cleaned (0.2 μm pores), the solution was spin coated on substrate to produce the polymer films. When the solvent evaporate completely, the samples were annealed at 170°C for various time periods to observe and record the film dewetting process using optical and atomic force microscope (AFM). Molecular recoiling stresses of the ultrathin polymer films were measured by studying the morphological changes of the dewetting hole topography acquired by AFM.

Aging experiments using a lower temperature than 170°C were conducted in order to investigate the stress relaxation in the ultrathin films. These aged samples were then put at 170°C to dewet for measuring the molecular recoiling stress. Alternatively, the temporal variations of the morphological features associated with the dewetting holes were detected by AFM and analyzed using a Maxwell model to calculate the variations of molecular recoiling stresses.

Results and Discussions:

During the long annealing time, the 40nm PS films' dewetting hole density increased at the beginning. It then decreased shortly later. But the 10nm PS films' dewetting hole density kept increasing (Figure 1). This is attributed to the relaxation of the molecular recoiling stress in the 40nm films. The stress was measured to be

around 5 MPa, too small to drive the dewetting process continuously to the final droplet fomration.

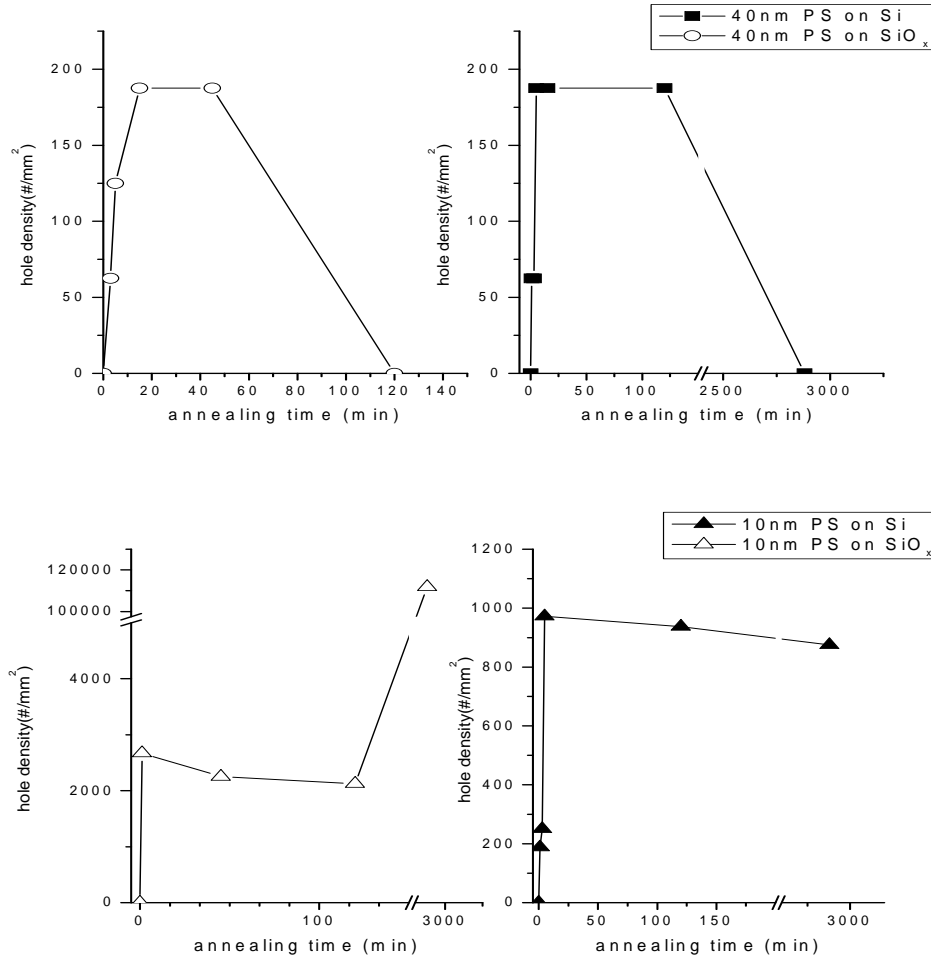


Figure 1. Hole density versus annealing time for various film thicknesses on different substrates

From Figure 1, we also can see that the hole healing rates of the 40nm thin films on SiO_x were higher than on those on the Si wafer. This indicates that on the substrates with smaller surface energy has a higher stress relaxation rate. Because the 10nm films has a larger recoiling stress (~17MPa) than the 40nm films, the 10nm films produce more dewetting holes. This observation provides the evidence that dewetting processes need enough recoiling stress to be driven. If the recoiling stress was too small at beginning, then the driving force of dewetting would not be enough to complete the whole dewetting process. The different substrates affect the hole density of the 10nm films as well. We found that the hole density on the SiO_x is much larger than that on the Si wafer. This indicates that polymer chain easily moved on the

low surface energy substrate, therefore they also have faster stress relaxation rates.

For the morphological changes of the dewetting hole, the surface angle decreased as the increasing annealing time increased, as shown in Figure 2. By regarding the surface angle as the shear strain caused by molecular recoiling stress, then the differential of the slope in the plot has become the evidence of stress relaxation. As the variations of the surface angle was smaller at greater annealing times, the strain rate and the shear stress obviously decayed. The fact that the films' surface angle decrease rate on the SiO_x was higher than that of the Si wafer indicates that polymer chains were easily to slide on the low surface energy substrate, so it has a faster strain rate decay and stress relaxation.

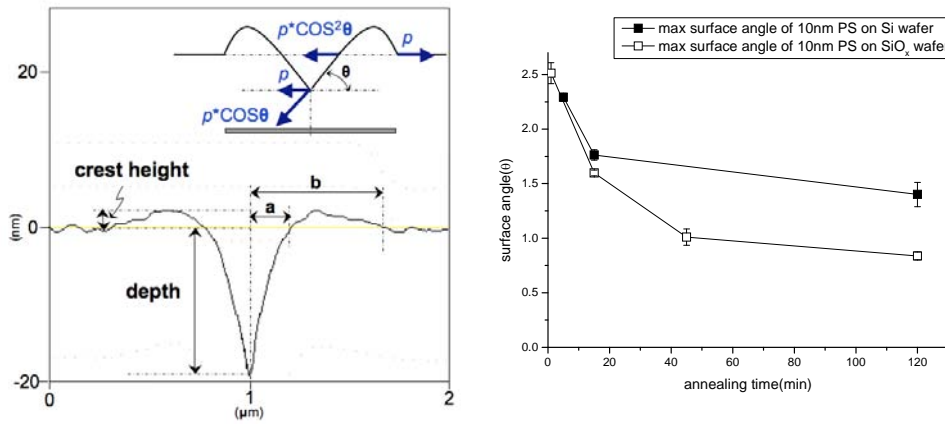
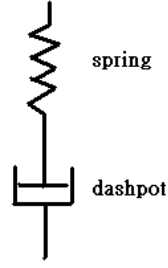


Figure 2. Hole's morphology and the plot of max surface angle versus annealing time.

We found that the surface angle exponentially decreased with annealing time, as shown in Figure 2. Since the polymer chains behaved viscoelastically, a simple Maxwell model was used to analyze its variations. In the Maxwell model as shown in Figure 3, we assumed that the molecular recoiling stress frozen in the films to be the tensile stress operative on the spring and dashpot that were connected in series. The stress esapplied in the sping and the dashpot are equal. During the stress relaxation, the strain in the dashpot increased slowly, absorbing deformation from the sping which recoiled, until the stress was fully relaxed at which point the dashpot strain reached the maximum [18]. The variation of the strain in dashpot thus can be used to estimate the stress level applied to the system during the stress relaxation. If we take the surface angle of a dewetting hole as the dashpot strain, its variation with relaxation time would yield information of the stress applied to the whole Maxwell unit. This approximation is reasonable as each point of the ultrathin films confined by the rigid substrate can be regarded approximately as independent to each other. Thus, the position where a single dewetting hole nucleated and grew should provide representative mechanical information of the whole film.



	Stress	Strain
Spring	σ_s	e_s
Dashpot	σ_d	e_d
Total	σ_t	e_t

$$e_t = e_s + e_d = \text{constant}$$

$$\sigma_t = \sigma_s = \sigma_d$$

Figure 3. The Maxwell model

From the Maxwell model, the stress would exponentially decayed and can be calculated by:

$$\sigma_t = \sigma_0 \exp\left(-\frac{Et}{\eta}\right) = \sigma_0 \exp\left(-\frac{t}{\lambda}\right)$$

Assuming the surface angle as the strain of dashpot:

$$\frac{de_d}{dt} = -\frac{d\theta}{dt}, \quad \theta = \theta_0 e^{-t/\lambda}$$

Substitution to the dashpot's strain rate, we can calculate the viscosity finally:

$$\begin{aligned} \sigma_d &= \eta \frac{de_d}{dt} \\ \frac{\sigma_0}{\eta} \exp\left(-\frac{t}{\lambda}\right) &= \frac{\theta_0}{\lambda} \exp\left(-\frac{t}{\lambda}\right) \\ \Rightarrow \eta &= \frac{\sigma_0}{\theta_0} \lambda \end{aligned}$$

Where σ_0 is the initial recoiling stress, which we can calculate from hole morphology at short annealing times. θ_0 is the initial surface angle and λ is the time constant in which both can be obtained from the plot of $\ln\theta$ versus annealing time, as shown in Figure 4.

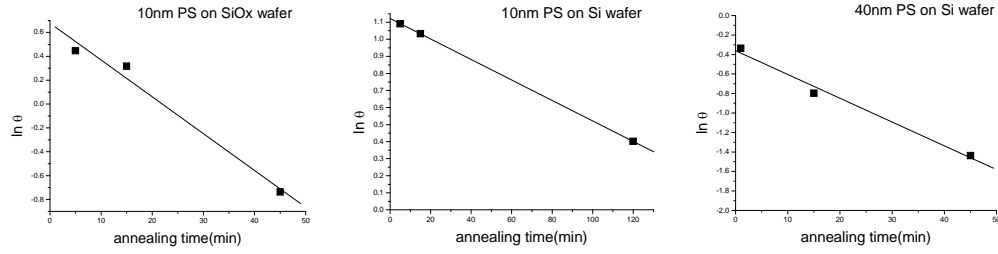


Figure 4. The surface angle versus annealing time

The results as shown in table 1. The experiment results are much greater than the bulk viscosity that was calculated by the WLF equation. The thinner the films, the greater the viscosity is, providing the evidence that polymer chain's motion is restricted by the substrate.

	$\eta(\text{Pa s})$
10nm PS on SiO _x	1.800×10^7
10nm PS on Si	1.666×10^7
40nm PS on Si	7.034×10^5
Calculated by WLF equation [19]	3.713×10^3

Table 1 Viscosities calculated from AFM topographic variations and by the WLF equation

Because the dewetting holes would change shape during long annealing time, we cannot measure the molecular recoiling stress directly. The second experiment is designed to measure the molecular recoiling stress after stress relaxation. First, we put the sample at a temperature (110°C) higher than T_g but not enough to produce dewetting holes. Aging it for several days allows the polymer chains enough time to undergo conformation re-arrangements, and thus to relax the residual recoiling stress. Then the sample was annealing at 170°C for a very short period of time to nucleate dewetting holes that were used to measure the recoiling stress. The experiment results as shown in Figure 5.

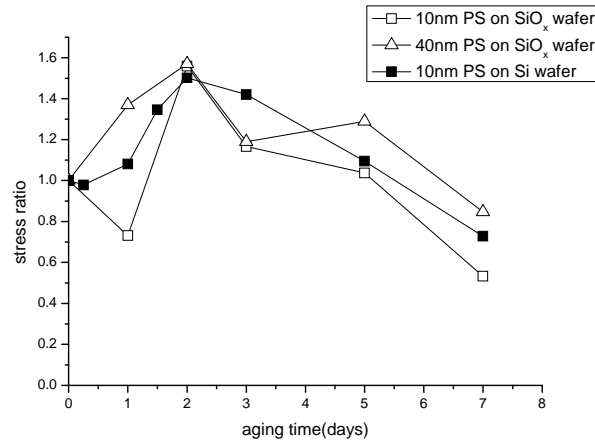


Figure 5. The normalized molecular recoiling stress ratios (to the initial residual stress) versus aging time at 110°C

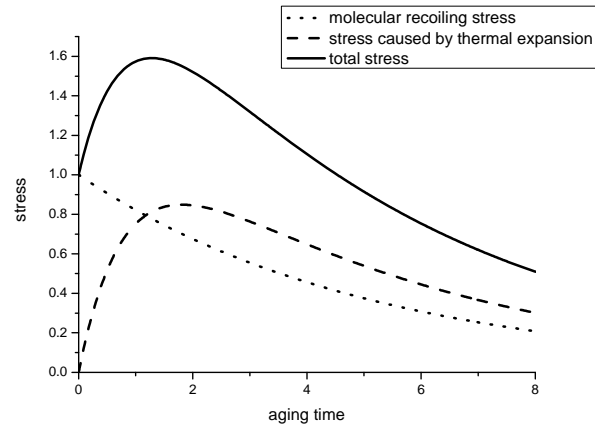


Figure 6. The total stress, summation of the molecular recoiling stress and that caused by thermal expansions

From the experiment results, we conclude that the stress will increase first and then decrease. Our suggestion is that, because polymers have strong negative thermal expansion coefficients [20-26], and there is enough time to allow the polymer stretching by the substrate's thermal expansion, the polymer chain would be stretched at first, increasing the stress. After long aging time, the stress relaxation occurs causing both the thermal expansion stress and the molecular recoiling stress to decrease. The model is depicted in Figure 6.

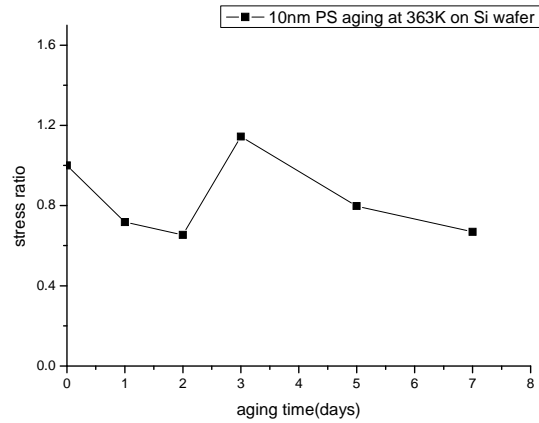


Fig. 7 The PS thin films aging at 90°C.

With the understanding that the stress in a viscoelastic solid, such as the ultrathin polymer films, relaxes exponentially, the data were analyzed with this assumption and the results were in good agreement with our assumption. The stress relaxation rates were almost independent of the film thickness for 10 or 40 nm. This was apparently due to a cancellation between the effects of a higher recoiling stress and also a greater restriction from substrate.

It was clear that the polymer chains in the ultrathin films were capable to move around and the stress relaxed substantially when aged at a temperature higher than the bulk T_g . However, when the films were aged at 90°C there were no stress relaxation measurable within days, the time scales used by this experiment. This indicates that the T_g of PS in the ultra-thin films is greater than 90°C and below 110°C, similar to that of the bulk.

Conclusions:

The higher the molecular recoiling stress, the easier the nucleation of dewetting hole can occur. If the molecular recoiling stress is too small, then after stress relaxation the dewetting of the polymer film cannot be driven and the dewetting holes are healed. When the polymer was aged at a temperature higher than that of the bulk glass transition temperature, the molecular recoiling stress decreased exponentially with annealing time. The decay rate depends on the restriction placed by the substrate. On the lower surface energy substrate, the polymer chain yields higher movement. The stress relaxation is faster on the low surface energy substrate. Although the thinner films have a greater molecular recoiling stress, there is also a greater viscosity, which indicates higher restriction from the substrate. Finally, the T_g of ultrathin films

appear to be independent of the film thickness in the regime explored here.

References:

1. G. Reiter and P. G. deGennes, *Eur. Phys. J. E*, 2001. **6**: p. 25.
2. M.H. Yang et al., *Phys. Rev. Lett.*, 2006. **96**: p. 066105.
3. M. H. Yang, Doctoral Thesis, Department of Materials Science and Engineering, National Tsing Hua University, Taiwan.
4. Y. L. Chang, Master Thesis, Department of Materials Science and Engineering, National Tsing Hua University, Taiwan.
5. G. Reiter, *Phys. Rev. Lett.*, 1992. **68**: p. 75.
6. G. Reiter, *Macromolecules*, 1994. **27**: p. 3046.
7. J.-L. Masson and P.F. Green, *J. Chem. Phys.*, 2000. **112**: p. 349.
8. G. Reiter and A. Sharma, *Phys. Rev. Lett.*, 2001. **87**: p. 166103.
9. H.S. Khesghi and L.E. Scriven, *Chem. Eng. Sci.*, 1991. **46**: p. 519.
10. R. Segalman and P.F. Green, *Macromolecules*, 1999. **21**: p. 801.
11. R. Limary and P.F. Green, *Langmuir*, 1999. **15**: p. 5617.
12. J.-L. Masson, R. Limary, and P.F. Green, *J. Chem. Phys.*, 2001. **114**: p. 10963.
13. R. Konnur, K. Kargupta, and A. Sharma, *Phys. Rev. Lett.*, 2000. **84**: p. 931.
14. P.-G. de Gennes, *C. R. Acad. Sci. B*, 1979. **228**: p. 219.
15. F. Brochard-Wyart, C. Redon, and C. Sykes, *C. R. Acad. Sci.*, 1992. **314**: p. 19.
16. G. Reiter and R. Khanna, *Phys. Rev. Lett.*, 2000. **85**: p. 2753.
17. G. Reiter and R. Khanna, *Langmuir* 2000. **16**: p. 6351.
18. McCrum, Buckley, and Bucknell (2003): "Principles of Polymer Engineering".
19. L. H. Sperling : "Introduction to Physical Polymer Science" 3rd edition.
20. G. Reiter, *Macromolecules* 27, 3046 (1994).
21. G. Reiter and P. G. deGennes, *Eur. Phys. J. E*, 2001. **6**: p. 25.
22. Orts, W. J., van Zanten, J. H., Wu, W. -L. & Satija, S. K. *Phys. Rev. Lett.* 71, 867–870 (1993).
23. M. Mukherjee, *et al. Phys. Rev. E* 66, 061801 (2002).
24. T. Kanaya, *et al. Polymer* 44, 3769–3773 (2003).
25. T. Miyazaki, K. Nishida, T. Kanaya, *Phys. Rev. E* 69, 022801 (2004).
26. H. Richardson, C. Carelli, J. L. Keddie, M. Sferrazza, *Eur. Phys. J. E* 12, 437–441 (2003).

Part B: Derivation of Surface Tension and Shear Modulus of Polymer

Thin Films Using a Model Based upon Power Spectral Density

Abstract

This work was intended to reveal the relationship between the reported shear modulus of polymer thin films and the residual stress due to the conformation distortion of polymer coils induced by nanometer scale confinement. The shear modulus was measured by power spectral density methods from the film topography acquired by atomic force microscopy. Polymer films of various thicknesses were explored.

Introduction

It has been reported that the glass transition temperature of polymer thin films decreases substantially as the film thickness decreases below some threshold values, around 10 – 20 nm for polystyrenes. In a close relation to this, it was also reported that the elastic modulus of ultrathin polymer films measured from atomic force microscopy topography relaxation by power spectral density (PSD) methods was two orders of magnitude smaller than the bulk values. However, research reports of contradictory conclusions were also found by other researchers. Recently, we unveiled the existence of large molecular recoiling stresses in ultrathin polymer films arising from molecular deformation of the macromolecules confined in the nanometer scales. It is thus interesting to explore the relationship between these PSD elastic modulus and recoiling stress, which will shed important light on the physical states of ultrathin polymer films.

Professor Ophelia K. C. Tsui published in the revue *Macromolecules* (2008, 41, 1465-1468) a paper entitled “Equilibrium Pathway of Spin-Coated Polymer Films” where she proposed a model to represent PSD curves. Thanks to this model, it is possible to derive the physical properties of polymer thin films cited above.

In the following sections we will provide more details about how we proceeded to deduce surface tension and shear modulus from the PSD: how to use the model of professor Tsui, but also what experiments are required. We then describe the results we have obtained, explain the problems encountered, and how we want to avoid it.

Approach and experimental methods

As indicated in the introduction, our work is based on a paper published by professor Tsui. The following model was what she had proposed:

$$A_q^2(t) - A_q^2(0)\Theta(q^* - q) \cong \frac{k_B T}{\gamma q^2 - A_{\text{eff}}/2\pi h_0^4 + 3\mu_0/h_0^3 q^2} \quad (4)$$

To calculate the surface tension and the shear modulus we first needed some data. AFM (Atomic Force Microscope) pictures were taken for 4 different sets of samples. We chose 2 molecular weights (2k and 90k) that were utilized with 2 thicknesses (10nm and 40nm). We defined annealing times: 60, 300, 1200, and 5400 seconds for 2k; and 60, 200, 1000, 4000, 14400 seconds for 90k. The 2k sample was likely to dewet faster than 90k, therefore requiring shorter annealing times. Also, because of the difference between these two molecular weights we took 85°C and 170°C for the 2k and 90k samples, respectively.

When we took the AFM pictures, we tried to avoid anything (dust particles or dewetting holes) that could have affected the model given above.

From the AFM pictures we obtained a PSD curve of our sample. We then use a fitting function similar to the model proposed by professor Tsui. We set:

$$A_q^2(t) - A_q^2(0)\Theta(q^* - q) \cong 1/(a^*x^*x - A_{\text{eff}}/2\pi h_0 + b/(x^*x))$$

Thus, by fitting this function we obtained the two parameters “a” and “b” that are proportional to the surface tension and the shear modulus. By a simple calculation these two values can be determined.

The scan size used here is 20 micrometers. When we checked the scan size effect it appeared that there is no difference in the results, unless we use a small one: 5 micrometers was not good enough, even with 10 micrometers some problems could occur. Indeed, the larger the scan size is, the more useful points we have for the PSD fitting. Very small values of the wave vector must be neglected, and large values of it does not give us more details. Indeed, the PSD levels off relatively fast with increasing values of the wave vector. However, the larger the scan size is, the more difficult it is to avoid dust particles and creating dewetting holes.

Thus, 20 micrometers seems to be a valid compromise for our work.

Obtaining the fitting results from the PSD curves is a relatively straightforward method. Therefore, it does not require a long time. Nevertheless, it is requiring many AFM pictures. For each annealing time, we dewetted 2 samples, and took 3 pictures of each.

Here, the PSD is used to deduce other physical properties of the material studied. From the paper, the model appears to be very accurate; except for a few points: the first and last ones of the PSD curve, which have to be neglected. Moreover, the method described here is simple to use.

These two points make the method potentially very interesting.

Results and Discussions

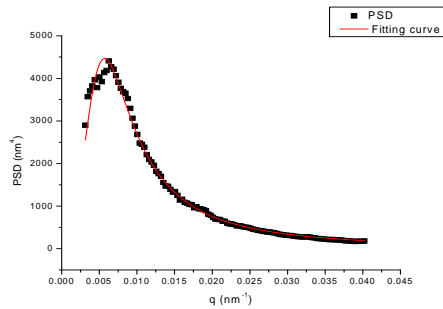
By applying the method to fit PSD data described above, we obtain curves similar to the following one:

The red line is the fitting curve we get. The dark points are given by the AFM pictures. This curve is just an example to illustrate our results. As explained previously, from this fitting we can calculate the surface tension and shear modulus of the sample studied.

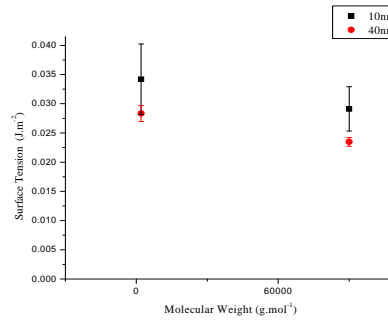
In the next pages we present the result of our calculation for the various annealing times given previously. We first show the surface tension, and then the shear modulus results. The problems that occurred will be exposed in the next section.

In this graph we show the time averaged surface tension for each set of samples. The red points are used for 40nm thickness, and the dark points refer to the 10nm thickness. For all the sets of samples the surface tension is steady through the different annealing times, which is why we plot here a time averaged value.

We have to note that on this graph and the next one (shear modulus), for each point we show a range equal to two times the standard error. Hence, 95% of the points are included in that range.



Example of the fitting of a PSD curve

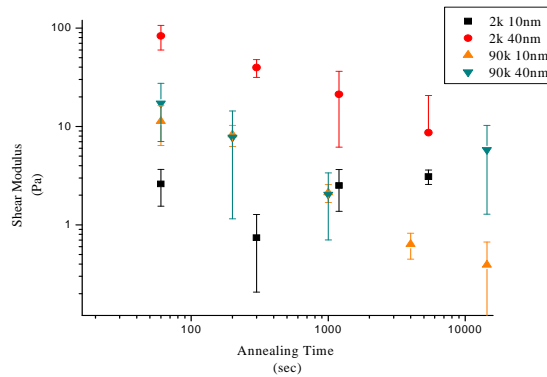


Time averaged Surface Tension

From this graph we can remark that the surface tension is slightly smaller for the sets of samples with a thickness of 40nm. However, this observation is probably due to the fitting. Indeed, when the thickness is 10nm the range in the results is broader. Also, in her paper, professor Tsui explains that for the times inferior to ~100 seconds, the surface tension is less stable than for longer times. We also observe this phenomenon in our data, especially for h=10nm (“h” refers to the thickness of the samples). This results in higher results for the time 60 seconds. Considering the fact that this phenomenon is more marked, it could explain the differences between 10nm and 40 nm.

The surface tension appears to be constant with different molecular weights. Its

average value is around 0.03 J.m^{-2} , and our results are included between 0.02 J.m^{-2} and 0.04 J.m^{-2} . This is consistent with professor Tsui's results. She obtains a constant value for surface tension, with different molecular weights and different annealing times. However, her values are higher: usually between 0.03 J.m^{-2} and 0.04 J.m^{-2} .



Shear Modulus depending on annealing time

In this graph we can observe the behavior of the shear modulus with increasing annealing time. The two sets of samples 2k-40nm, and 90k-10nm show a similar behavior to what describes professor Tsui: a decrease with time. However, for the two other sets of samples, it is not the case.

For the 2k-10nm, the shear modulus appears to be constant with annealing time. But we encountered problems to take the AFM pictures for the 2k-10nm. It was not possible to avoid the presence of dewetting holes, that could have disrupted the PSD curves, and so the fitting. Thus, we will prepare new samples for the conditions of 2k and 10nm, and be very careful in the preparation. Indeed, the dewetting holes are present at all the annealing times, even the shortest ones. Therefore, a problem related to the preparation is a very plausible explanation for the occurrence of these holes. About the samples of 90k and 40nm thickness, we first should note that for the time 4000 seconds the point is out of scale (-7.62). Then, the last point is not what we would expect, because it has a value close to the shear modulus of the second time. Again some problems related to the AFM pictures could explain this result: with this set of samples, in the last time, some dust particles appeared, and so the quality of the pictures is not good.

In her paper, professor Tsui shows a decrease with time for the shear modulus, except for high molecular weights (212k and above), where it first levels off, and then decreases. For two sets of our samples, we get a similar behavior. Nonetheless, our results show much smaller values (for 90k, almost 10 times smaller than 115k in professor Tsui's paper). This discrepancy might originate from two different reasons:

the temperatures we used are higher (for 90k, 20°C up to the temperature she used). In her paper, professor Tsui shows two plots for 2.3k and 18nm thickness, with 85°C and 100°C. It points out that the shear modulus for T=100°C is much smaller.

The other explanation is that, generally, professor Tsui chose to do her experiment on thicker films. For instance, the thickness she used for 115k is 103nm.

Another problem encountered is that we sometimes get negative results for the shear modulus (even when the average is positive). To limit this problem we used a smoothing function on all the PSD curves. It helped, but did not eradicate the problem.

The negative shear modulus sometimes intervenes in short times. These negative values could be explained by the presence of residual stress. Nonetheless, samples with 90k and h=10nm would be the more likely to show this behavior, but we did not obtained any negative result for this set of samples.

So, this behavior could be due to the quality of the pictures. Nevertheless, a low quality for a picture does not imply a negative value. We could also think that it shows the limitations of the fitting. We did not check this point yet, but, perhaps the amplitude of the peak in the PSD curves is more important, or the roughness shows a higher value in this situation.

Conclusions

The model based on the PSD to deduce the surface tension and shear modulus is of high interest because these properties of the materials are very important. Moreover, this model is relatively easy to use.

The surface tension values obtained are consistent with what could be expected, and with professor Tsui's data.

However, we still have some problems with the shear modulus. In order to obtain a coherent behavior, the AFM pictures have to be as good as possible. Some fitting values become negatives. This phenomenon does not seem to be real, and its origin remains unclear. We should investigate in two directions: the quality of the AFM pictures, and the limits of the fitting model.

References

1. "Equilibrium Pathway of Spin-Coated Polymer Films"; Ophelia K. C. Tsui,^{*,†} Yong Jian Wang,[‡] Fuk Kay Lee,^{†,§} C.-H. Lam,[§] and Zhaohui Yang[†]; *Macromolecules* 2008, *41*, 1465-1468

2. “Dewetting of Thin Polymer Films”; Gunter Reiter; Physical Review Letters, Volume 68, Number 1
3. “Molecular Recoiling in Polymer Thin Film Dewetting”; M. H. Yang, S.Y. Hou, Y. L. Chang, and A. C.-M. Yang*; PRL 96, 066105 (2006)
4. “Spinodal-like dewetting of thermodynamically-stable thin polymer films”; C. Bollinne, S. Cuenot, B. Nysten, and A.M. Jonasa; Eur. Phys. J. E 12, 389–396 (2003)
5. “Residual stresses in thin polymer films cause rupture and dominate early stages of dewetting”; GUNTER REITER, MOUSTAFA HAMIEH, PASCAL DAMMAN, SE’VERINE SCLAVONS3, SYLVAIN GABRIELE, THOMAS VILMIN AND ELIE RAPHAË; Nature Materials 4, 754 - 758 (2005).

Part C: Macromolecule Condensation during Formation of Ultrathin Films

Abstract

We propose a molecular model to describe the film formation processes of ultrathin polymer films prepared by spin coating. Coupled with the theoretical explorations, the effect of molecular weight was investigated in details in the light of solvent evaporation and thin film instability (dewetting). For polymers of higher molecular weights, solvent evaporates slower from the coil interiors to lend more time for the chains to adjust their conformation. The residual stress is thus minimized and the systems ultimately achieve local free energy minimum and film stability. Associated with the low chain mobilities, the high molecular weight chains tend to self-contract and undergo only low degree re-entanglements during the solvent evaporation stage. In contrast, for polymers with low molecular weights, the solvent evaporation rates are faster, thus the polymer coils tend to be frozen into solid films in their extended states. Thus, the molecular recoiling stresses residual in these films are higher, and the films are subjected to a much higher dewetting instability. The morphological observations and recoiling stress measurements by atomic force microscopy have revealed consistent results that are in excellent agreement to support this proposed model.

Introduction

Polymer thin films play a crucial role in a wide diversity of disciplines and application fields. These include many applications in our daily lives, for example, the clothes we wear or the plastic bags we use. In the technological area, for example, of the semiconductor industries [1], the resistance layers and dielectric layers are made

of polymers. Application attempts in the emerging fields, such as photoelectronics [2, 3], solar energy [4] and biomaterials [5], are gaining significant grounds to the ultimate successful realization of the polymer-based technologies. As required by the progress of new techniques, polymer thin films are becoming thinner and thinner. These ultrathin polymer films are almost invariantly prepared by using the convenient spin coating method. Although highly ubiquitous to both the industrial world and the academia, the molecular processes of thin film formation enroute of spin coating have been little known [6]. It, obviously, is an important subject that needs to be fully explored.

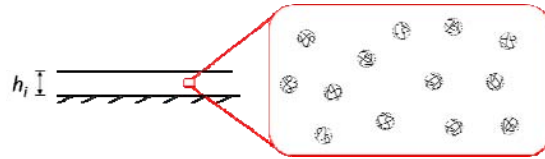
Therefore, we try to propose a new model to depict the polymer film formation processes and explain the dewetting mechanisms [7, 8] to discuss the molecular weight effects. In this research, we tried three experiments to observe the molecular weight effects on film formation processes and dewetting mechanisms. The first one is critical concentration test. We prepare ultra dilute solution to spin coat on silicon oxide wafer and utilize atomic force microscope to observe whether there is any difference between high and low molecular during film formation processes. The second experiment is solvent evaporation rate measurement. We try to measure the weight loss during solvent evaporation to simulate the spin coating process and find out the differences between high and low molecular weight. The third experiment is recoiling stress measurements. We dewet the specimens and calculate recoiling stress for different molecular weight.

The Proposed Model

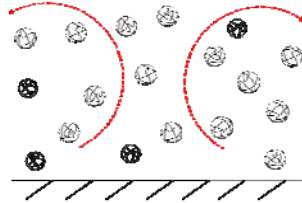
Here, we try to propose a model to interpret the film formation processes of polymer with volatile solvent. The figures below are the illustrations for several stages during film formation processes. Originally, the polymer solution with initial concentration C_o was deposited on the substrate and spin casted, the balance of centrifugal force and viscous force determined the quantities remained on the substrate. In the stage 1, the concentration of residual liquid film C_o was much lower than C^* and every swollen polymer coil was far away from each other. Then, the residual liquid film with initial thickness h_i was proceeding with solvent evaporation and kept shrinking film thickness as increasing time. In the stage 2, solvent evaporates from the free surface and there is convective transportation called plume [9, 10]. Here, we assumed that the solvent firstly evaporate from the interstitial site than from the interior of polymer coils, therefore, these upward flows bring more solvent to the free surface and make interstitial solvent evaporate uniformly from top to bottom. As interstitial solvent keeps evaporating, the concentration increases gradually and approaches to C^* at stage 3. In this stage, the polymer coils contact with each other

and pile up with liquid film thickness h^* . Then, the solvent evaporates from the interior of polymer coils near the free surface and causes the formation of skin layer [11]. The upper portion of polymer coils contract or collapse due to the evaporation of solvent inside. As the solvent from interior of coils keep evaporating, the skin layer extends downward to the bottom plate in the stage 4. The polymer chains interdiffuse as most of solvent evaporates completely from interior of coils. In the stage 5, the solvent evaporates completely to form a final glassy film with thickness h_0 .

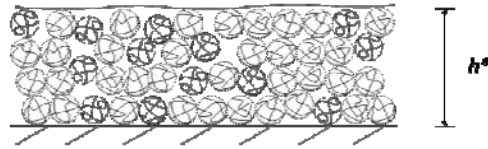
Stage 1



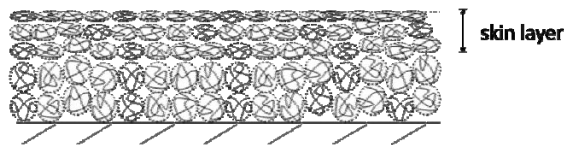
Stage 2



Stage 3



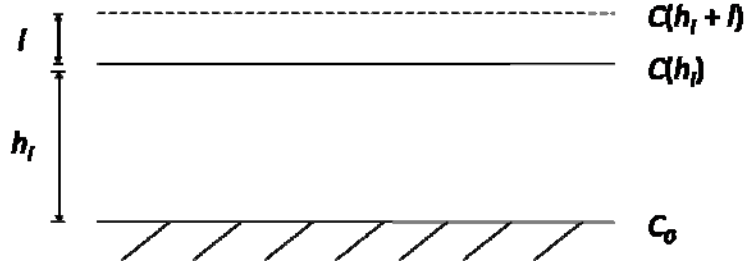
Stage 4



Stage 5



In the stage 2, there is mass transportation of solvent evaporation from liquid film to the air with a diffusion coefficient D_{air} . The illustration figure of liquid film is as following:



The flux of solvent evaporate to the air, J_a , could be approached by Fick's 1st law:

$$J_a = -D_{air} \frac{C(h_i + l) - C(h_i)}{l} \quad (1)$$

where D_{air} is the diffusion coefficient of solvent in air, and l is the thickness of diffusion boundary layer approximated by linear concentration profile of solvent. $C(h_i)$ and $C(h_i + l)$ are the concentration of solvent at h_i and $h_i + l$, respectively. For an instant equilibrium, the partial gas pressure of solvent is equal to the equilibrium gas pressure p_e , and could be replaced with pure solvent vapor pressure $p_v(T)$ in the dilute system[de Gennes]. Therefore, the concentration at the free surface $C(h_i)$ could be expressed as:

$$C(h_i) = \frac{p_v}{kT} \quad (2)$$

The scaling estimate of D_{air} is proportional to $v_{th}\lambda$, where v_{th} is thermal velocity and λ is mean free path of solvent molecules under the atmospheric pressure. We approach the mean free path, λ , by idea gas law and obtained D_{air} as:

$$D_{air} \sim v_{th}\lambda = v_{th} \cdot \frac{kT}{a^2 p_a} \quad (3)$$

where a is the size of one solvent molecule and p_a is the atmospheric pressure.

Substitute (2), (3) into (1), we obtained:

$$J_a = \frac{v_{th}}{a^2 l} \cdot \frac{p_v}{p_a} \quad (4)$$

For the film part, the flux of solvent diffuse from bottom plate to surface, J_f , could be expressed as:

$$J_f = -D_{coop} \frac{C(h_i) - C_0}{h_t} \quad (5)$$

where D_{coop} is the cooperative diffusion coefficient[de Gennes' book] and C_0 is the concentration at the bottom plate, equal to the initial concentration. Due to the mass

conservation, the flux J_a , should be equal to J_f . Therefore, the concentration difference between bottom plate and free surface is:

$$C_0 - C(h_f) = \frac{W_{th}}{a^2 D_{eff}} \cdot \frac{h_f}{l} \cdot \frac{P_2}{P_1} \quad (6)$$

Experimental Procedures

Series of hydrogenous polystyrene (h-PS) from high molecular weight to low molecular weight were used to prepare samples with nano-scale film thickness. Polystyrene first was dissolved in toluene and filtered through 0.2 μ m filter, then the solution was spin casted on the silicon oxide as substrate. Changing solution concentration and fixing the rotating speed at 4500 rpm to control the film thickness. Put the prepared samples under atmospheric environment for 2 days to make the residual solvent evaporate completely. After drying, the films were annealed at 170°C for different time.

Micrographs of the PS thin film specimens were recorded with AFM by using contact mode. The standard probes of Veeco tips were used to measure the information of the specimens. The cantilever, with silicon-tip on nitride lever, had a spring constant of 0.03 mN. The image obtained under the constant force mode and the measurements were done in the atmospheric pressure and room temperature. Part of experiments containing PS specimens with ultra-thin film (1~3 nm) were finished by tapping mode to minimize tip-induced sample degradation. Several images were obtained for each sample. The scan range was 5 μ m \times 5 μ m or 10 μ m \times 10 μ m to achieve the best resolution.

Results and Discussions

Solvent Evaporation Rates

The Skin layer effect was first considered. In the proposed model, we assumed that interstitial solvent evaporates before solvent inside the polymer coils. Then, we try to measure the solvent evaporation rate test to distinguish the differences between interstitial solvent and the solvent inside the polymer coils. On the other hand, molecular weight effect could be observed by this test as well if the solvent evaporation rate of high and low molecular weight are really different.

The testing molecular weights we choose are 2M and 50k polystyrene. The solution is prepared with initial concentration 10mg/mL and deposited volume 0.3mL. The following pictures are plots of weight loss per minute versus time for 2M and

50k.

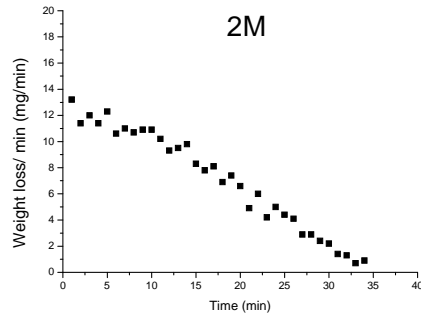


Fig 1. Weight loss rates for 2M.

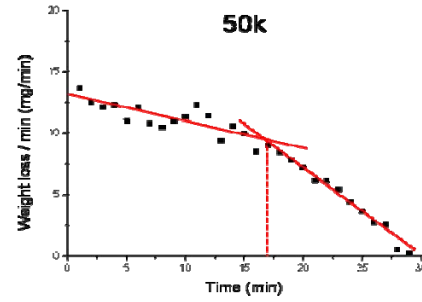


Fig 2. Weight loss rates for 50k.

From Figs 1 and 2, the weight loss per minute decrease with increasing time for both 2M and 50k. But for 50k, the values of weight loss per minute are higher at former part and then decreases quickly at later part. It means that there is apparently two-stage change of weight loss at roughly 17 minutes. Therefore, we can conjecture that the interstitial solvent evaporate first until all of the interstitial solvent evaporate up. Then, solvent evaporate from the interior of polymer coils and skin layer start to form to hinder further evaporation of lower layers. The skin layer effect cause the decrease of weight loss can be explained by two-stage weight loss behavior, and the changing point is corresponding to the polymer volume fraction of C^* of 50k, roughly 4%. As for 2M, there is not apparent two-stage behavior in the plot because the critical volume fraction of 2M is 0.2%, very close to the volume fraction of initial concentration. Therefore, almost all of the evaporation processes occur at later part.

Molecular Weight Effects

The Fig 3 is the comparison of 2M, 50k and pure solvent with the same initial concentration and deposited volume.

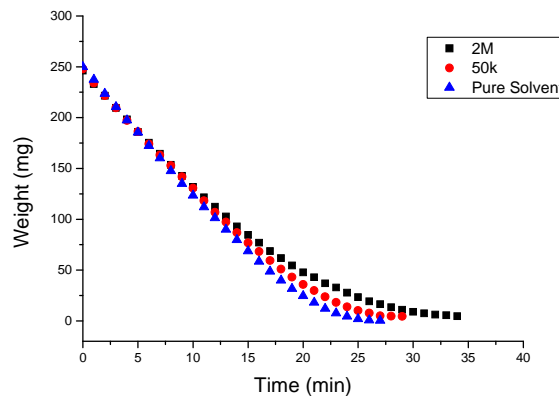


Fig 3 The direct weight versus time for 2M, 50k and pure solvent.

We can see that the direct weight decreases with increasing time for three different solutions, but 2M has the slowest solvent evaporation rate and pure solvent has the fastest one. On the other words, polymer with high molecular weight has better solvent retention ability than lower one. Therefore, 2M polymer coils have longer time to adjust the instabilities during the relatively slow evaporation rate, while solvent escape from the inside of low molecular weight polymer coils.

Critical Concentration Tests

Fig 4 shows AFM images of polymer films which are formed near the critical concentrations of 2M and 90k molecular weight, the initial concentrations are 0.8, 0.5, and 0.2 mg/mL, respectively.

At 0.8 mg/mL, both 2M and 90k polymer solutions formed polymer films with whole surface and no clear pore. Therefore, the concentration which is over 0.8 mg/mL could form complete films. When the concentration is degraded to 0.5 mg/mL, there are different morphologies of two polymer solutions. It is a complete film and only a few small pores appear for 2M, while there are many pores but most of film is complete for 90k. It suggests that the critical concentration for forming films is between 0.5 ~ 0.8 mg/mL for polystyrene. When the concentration decayed to 0.2 mg/mL, both two molecular weight polymer solution can not form a film. Most of films were broken, and it was more serious for 90k.

According to the film theory, it suggests that the molecular chains had longer time to adjust and shrink due to the slower solvent evaporation rate of the polymer coils of 2M polymer in the dilute concentration. Thus, to compare with 90k polymer, 2M polymer is more stable. Then because of its longer chains and larger volume, it has low mobility, polymer coils are difficult to move after shrink. Therefore, the smaller pores for 2M are relative to the mobility of the molecular chains.

2M

90k

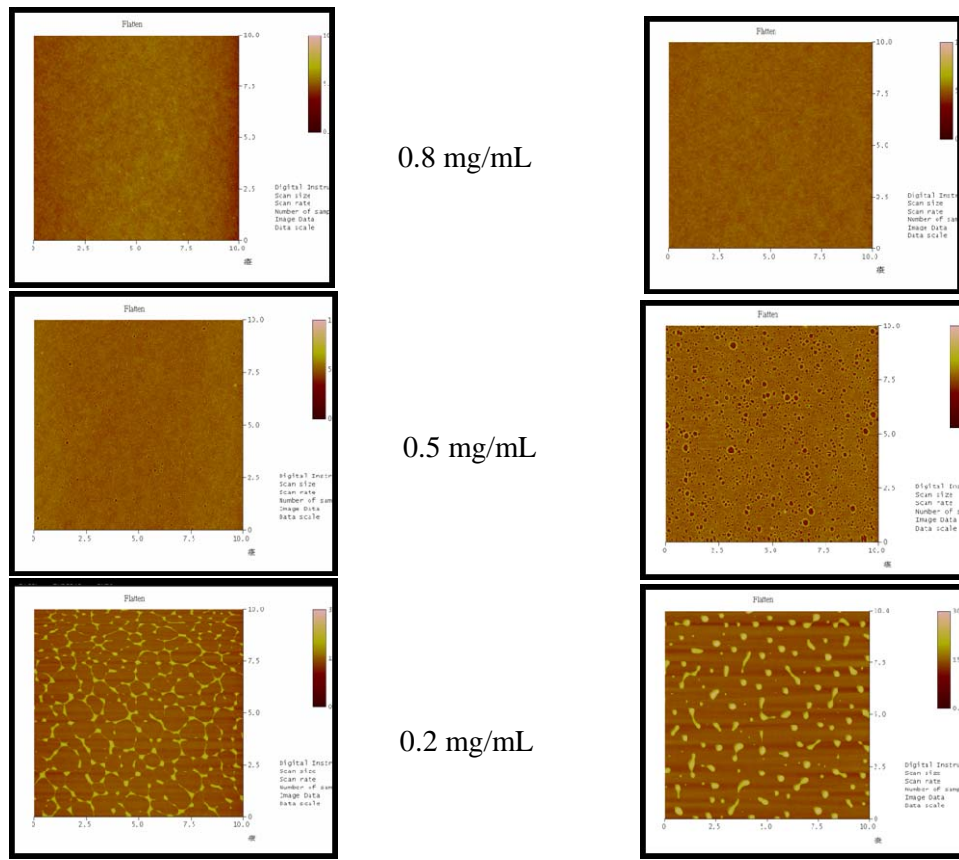


Fig 4 AFM images of polymer films for different initial concentrations.

In contrast, the solvent evaporated quickly from the polymer coils of the low molecular weight PS, the molecular chains had shorter time to adjust itself. Most of chains were collapsed directly and were not stable. But due to its shorter chains and high mobility, it can move easily and entangles with other chains, and the pores are larger.

Fig 5 is AFM images of dewetting samples from 0.8 mg/mL polymer solution of 2M and 90k molecular weight. The samples were heated by 30s, and 1, 2, and 5 min.

After 30 s heating, there are some pores in the 2M polymer film. Then after 2 min heating, there were more pores and became larger. After 5 min heating, the film was broken seriously, but the arrangement was more compact. For 90k polymer film, it was broken much more after 30 s heating. Then after 5 min heating, the pores became larger and the film was incomplete.

2M

90k

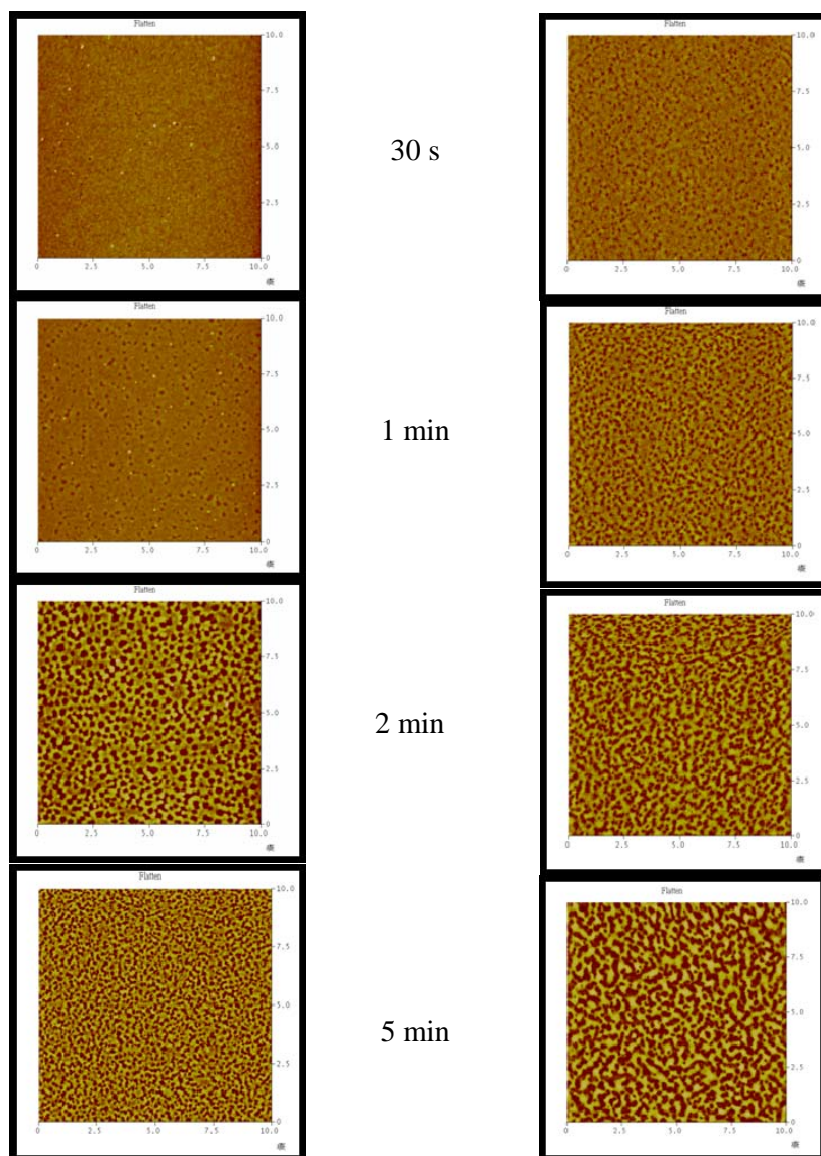


Fig. 5 AFM images for different heating time with initial concentration 0.8 mg/mL.

The Effect of Molecular Weight

In experiment III, the film thickness was fixed. Fig 6 indicates the relationship between recoiling stress and molecular weight, the film thicknesses are 10 nm and 40 nm.

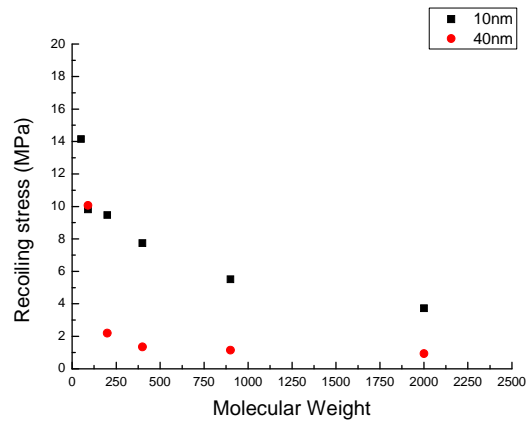


Figure 6. Recoiling stress vs. molecular weight.

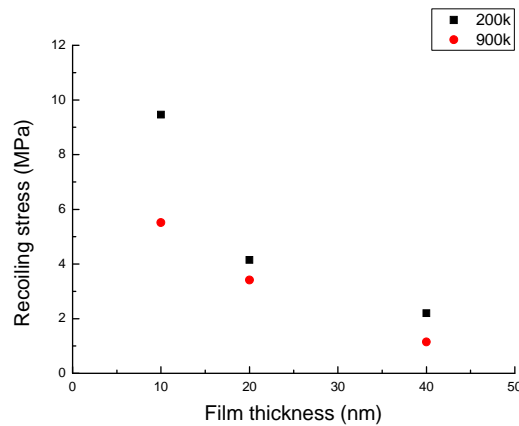


Figure 7. Recoiling stress vs. film thickness

From Fig 6, no matter the film thickness, with increasing molecular weight the recoiling stress tended to decrease. The recoiling stress decreased much when the molecular weight is between 50k and 200k.

In another experiment, we selected two molecular weights, 200k and 900k, to observe the effect of film thickness on recoiling stress in Fig 7. In Fig 7, with increasing film thickness, the recoiling stresses decreased from 10 to 2.5 MPa for 200k and from 5.5 to 1 MPa.

5. Conclusions

From the solvent evaporation rate test, the two-stage weight loss behavior of 50k show the skin layer effect on hindering solvent evaporates from the interior of polymer coils. The comparison of 2M, 50k and pure solvent shows the molecular

weight effect on solvent evaporation. Polymer with higher molecular weight has slower solvent evaporation rate to adjust the instabilities caused from the solvent escaping, so the polymer chains have more time to adjust and self-contract. However, with the characteristics of low mobility for high molecular weight polymer, they tend to be low degree re-entanglement. Therefore, when high molecular weight polymer is processing dewetting experiments, they are relatively well-adjusted to release the residual stress, so the recoiling stress of high molecular weight is small. From the observation of AFM graphs, 2M thin film has less holes and the distance of droplet is small. For polymer with low molecular weight, such as 50k, solvent evaporates too fast for polymer chains to adjust the instabilities, so they tend to collapse directly. Low molecular weight polymer is easy to re-entanglement with other chains due to the high mobility. As dewetting the polymer film, many the holes quickly appear because of higher recoiling stress. From the AFM images, there are much more holes for 50k and the droplet distance is longer.

6. References

- [1] M. Ishikawa, I. Sakamoto, M. Ishii, J. Ohshita, *J. Polym. Sci. A* **31**, 3281 (1993).
- [2] Rodrigo E. Palacios, Paul F. Barbara, *J. Fluor.* **17**, 749 (2007).
- [3] Dehong Hu, Ji Yu, Paul F. Barbara, *J. Am. Chem. Soc.* **121**, 6936 (1999).
- [4] K. M. Coakley, M. D. McGehee, *Chem. Mater.* **16**, 4533 (2004).
- [5] K. J. L. Burg , S. Porter , J. F. Kellam, *Biomaterials* **21**, 2347 (2000).
- [6] B. S. Dandapat, P. Daripa, P. C. Ray, *J. Appl. Phys.* **94**, 6 (2003).
- [7] G. Reiter, *Phys. Rev. Lett.* **68**, 75 (1992).
- [8] G. Reiter, *Macromolecules* **27**, 3046 (1994).
- [9] P.G. de Gennes, *Eur. Phys. J. E* **6**, 421(2001).
- [10] P.G. de Gennes, *Eur. Phys. J. E* **7**, 31 (2002).
- [11] D. E. Haas, J. N. Quijada, S. J. Picone, D. P. Birnie, in *SPIE Proc. 3963, Sol-Gel Optics*, V. B. Dunn, E. Pope, H. K. Schmidt, and M. Yamano, Editors, 280 (2000).

Chapter 5: Viscoelastic Thin Polymer Films under Transient

Residual Stresses: Two-Stage Dewetting on Soft Substrates

(Published at *PHYSICAL REVIEW LETTERS* **100**, 178301 (2008))

Abstract:

A nonmonotonic, two-stage dewetting behavior was observed for spin coated thin viscoelastic polymer films on soft elastic substrates. At times shorter than the relaxation time of the polymer ($t < t_{\text{rep}}$), dewetting generated deep trenches in the soft rubbery substrate which, in turn, almost stopped dewetting. At later stages ($t \gg t_{\text{rep}}$), dewetting accelerated, accompanied by an unstable rim. However, holes nucleated at $t < t_{\text{rep}}$ showed only this second-stage behavior. Our observations are attributed to large elastic deformations in the substrate caused by transient residual stresses within the film.

Introduction:

The stability of ultrathin polymer films on various substrates has attracted broad interest due to their ubiquitous applications in numerous fields and the possibility of unveiling molecular processes and the corresponding physics that govern the behavior of polymers under confinement [1–20]. On nonwetttable substrates, such ultrathin films (thickness, $h < 100$ nm) may undergo dewetting driven by capillary (intermolecular) forces [1–13] and residual stresses within these films [14–21]. However, only recently the causes and consequences of residual stresses in ultrathin films, generated by the process of spin coating which is often employed for thin film preparation [14,20], were investigated systematically. In a physical aging experiment, residual stresses were found to play a prominent role in controlling nucleation and growth of dewetting holes in the thin viscoelastic films [16]. Theoretically, it was shown that films experiencing lateral stress undergo an instability initiated by an anisotropic diffusion of the polymer molecules which can lead to the formation of dewetting holes [17]. Substantial residual stresses, also dubbed molecular recoiling stresses, were determined by dewetting experiments as a function of molecular weights and film thickness in thin polymer films [16–20]. One of the striking revelations discovered in these recent experiments is the surprisingly large magnitude of the molecular recoiling force, which can amount up to several times the capillary force [18,20]. In the here presented dewetting experiments, we attempt to temporarily store part of the corresponding energy in the form of deformation energy of an elastic substrate and so try to make the magnitude of these stresses visible. In addition, we anticipate that the transient contribution of the molecular recoiling force in dewetting

of viscoelastic thin films on deformable soft elastomeric substrates should give rise to a host of remarkable dewetting scenarios. Taking into account knowledge of liquid-liquid dewetting, film-soft substrate interactions [3,5], as well as liquid droplet spreading on viscoelastic surfaces [22–27], we therefore explore the dewetting behavior based on a strong mechanical coupling between a viscoelastic film and a soft elastic substrate. In particular, we report the first detailed study on how dewetting on a soft substrate depends on the relaxation time of the retracting polymer.

Experimental Section:

For our experiments, monodisperse, high molecular weight polystyrene (PS) ($M_w = 0.2, 0.4, 0.9, 1, 2, \text{ and } 5 \text{ Mg/mol}$, $M_w/M_n < 1.10$, Pressure Chemicals Company, USA and PSS, Mainz, Germany) were used for the formation of ultrathin viscoelastic films of thickness (h) ranging from 20 to 80 nm. The substrates used for most of the experiments presented here were prepared by spincoating a heptane or toluene solution of polydimethylsiloxane (PDMS) silicone rubber (Sylgard 182 or Sylgard 184, Dow Corning) onto polished silicon wafers. The resulting thickness (e) ranged from 20 nm to about 2 μm . The Young's modulus of the silicone cured for 1 h at 150 $^{\circ}\text{C}$ was 2 MPa [28]. On top of this silicone layer, we spin coated the ultrathin PS film.

We note that the results presented below did not change significantly when the PS film was prepared on a bare silicon wafer, floated off on water and then transferred onto the silicone layer. However, as this transfer process contains the risk of creating many imperfections in the films (stresses, deformations, ripples, folds, weak contact, inclusions of air gaps, etc.), we used such samples only for control experiments. To investigate the effect of substrate softness, we used a Si-wafer coated with a thin monolayer of irreversibly adsorbed PDMS (thickness 10 nm). The film thickness and roughness of the PS films were measured by ellipsometry and atomic force microscopy (AFM). Dewetting was performed in a vacuum oven or on a nitrogen-purged microscopy hot-stage at temperatures ranging from 130 $^{\circ}\text{C}$ to 200 $^{\circ}\text{C}$.

The dewetted samples were examined under an optical microscope and by AFM (Digital Instruments Nanoscope IIIA/D3100) at ambient conditions.

Results:

Previous experiments (e.g., [2,7,10]) on nondeformable, nonwetable substrates showed the appearance of many holes, randomly distributed across a thin polymer film which was heated above its glass transition. A distinct rim was associated with

each hole and typically these holes grew until they eventually coalesced and formed polygon ridges which ultimately disintegrated into droplets via a Rayleigh instability [10,29]. However, in the here presented experiments a different behavior was observed (Fig. 1). Initial holes grew rapidly at the beginning, but subsequently slowed down significantly and came to an apparent standstill. In contrast, holes nucleated at later stages [for example, after several hours at 170°C in Fig. 1(a) and 1(b)] did not show such a slowing down but rather exhibited rim instabilities and an acceleration of the dewetting velocity. With the early formed holes remaining almost stationary, these later ones grew so rapidly that they eventually covered almost the whole film. Interestingly, at about the same time as these secondary unstable holes appeared, the early stage holes also slowly restarted to grow in diameter and developed fingers.

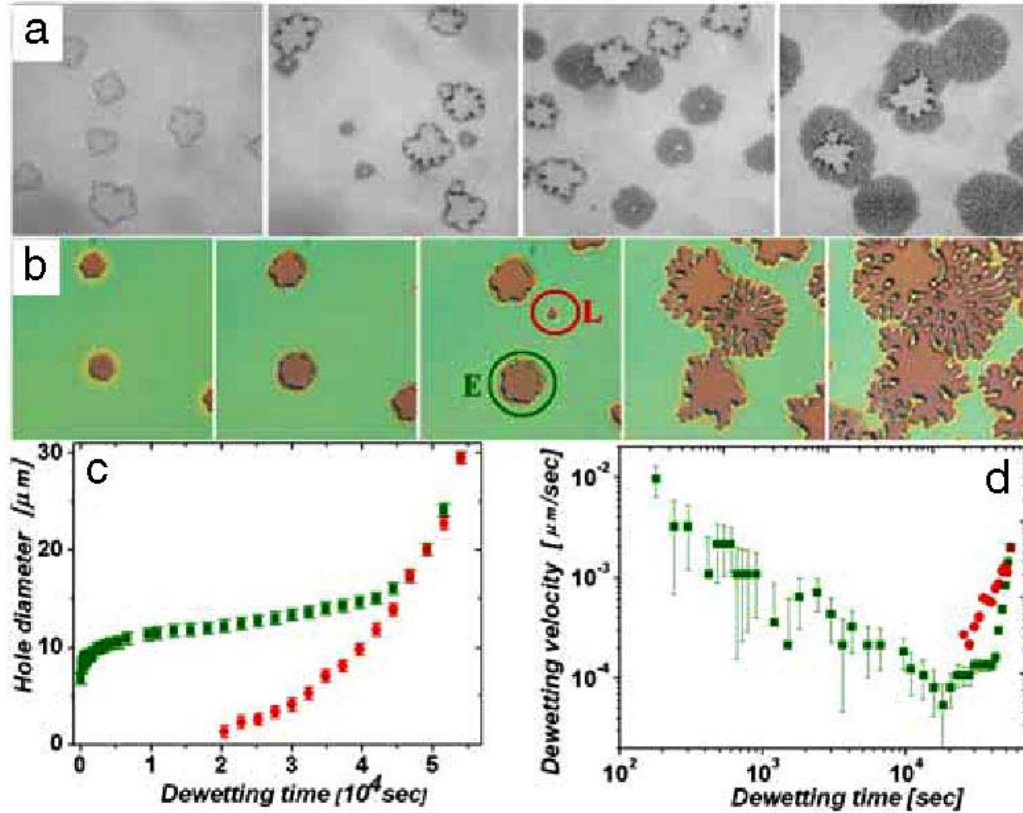


FIG. 1 Optical micrographs showing dewetting of (a) of different samples of a 40 nm PS film ($M_w = 0.9$ Mg/mol) on a 2 μm PDMS layer at 170°C ($t_{\text{rep}} = 2700$ sec) for (from left to right) 5 360 480 and 540 min (size of images: 206 x 206 μm^2) and (b) a time series from a single 40 nm PS film ($M_w = 1.0$ Mg/mol) on a 200 nm PDMS layer at 180 °C ($t_{\text{rep}} = 1200$ sec) for (from left to right) 2, 110, 380, 800, and 900 min (size

of images: $58 \times 58 \text{ m}^2$). (c) Hole diameter (for uneven holes, a mean diameter of the enveloping perimeter of the hole was taken), and (d) dewetting velocity for the holes labeled by **E** (squares) and **L** (circles) in panel (b).

Such a difference in dewetting behavior between early and late holes, but also the possibility to nucleate holes in thin films after many hours of annealing, was never observed on hard substrates. Thus, we examined the influence of the soft substrate by systematically varying the thickness (e) of the rubbery PDMS layer. From Fig. 2, it becomes quite obvious that, with respect to hard substrates, dewetting on soft substrates was slowed down significantly. For example, at annealing times longer than about 10^4 sec, a quasistatic hole diameter was observed which did not depend significantly on the dewetting temperature [see the 360 nm thick PDMS layer in Fig. 2(a)]. Solely, at the significantly higher temperature of 180°C , this diameter was reached much faster. From Fig. 2(b), one can conclude that the hole diameter decreased with increasing PDMS layer thickness. In contrast to the behavior on a hard substrate (compare with the results on Si-wafer coated with a PDMS monolayer), dewetting holes created on a cross-linked PDMS layer of $1.5\mu\text{m}$ did not grow beyond a diameter of about $5 \mu\text{m}$, even after long annealing times (but shorter than the bulk reptation time (t_{rep}) of the polymer at that dewetting temperature [30]). We conclude that dewetting of PS films on thick enough soft substrates seems to be confronted with a limiting diameter of the opening holes.

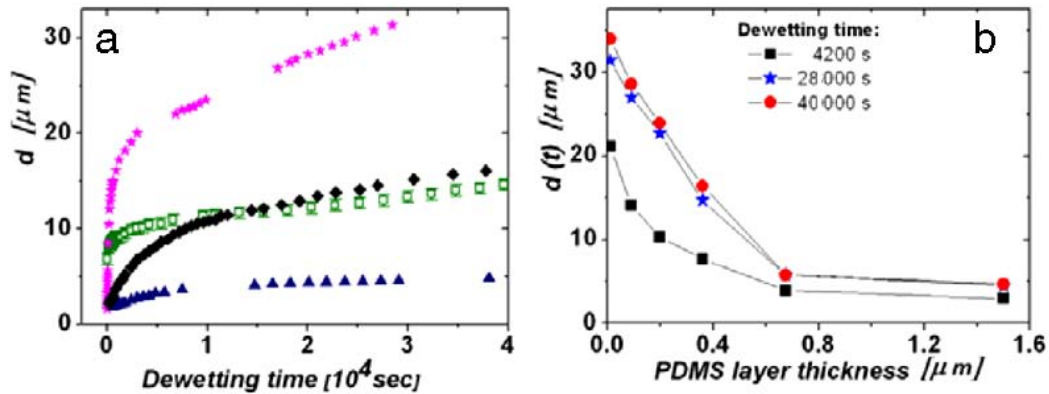


FIG. 2. (a) Hole diameter (d) as a function of dewetting time (for uneven holes, a mean diameter of the enveloping perimeter of the hole was taken) for a 55 nm PS film ($M_w = 1.0 \text{ Mg/mol}$) dewetting at 130°C ($t_{\text{rep}} = 1.2 \times 10^6 \text{ sec}$) on a 10 nm monolayer of irreversibly adsorbed PDMS molecules (stars), a 360 nm thick (lozenges) and a $2\mu\text{m}$ thick cross-linked PDMS layer (triangles). For comparison, the data from hole “E” of Fig. 1 (open squares) are replotted (b) Hole diameter as a function of the

thickness of the soft rubbery PDMS layer for a 55 nm PS film ($M_w = 1.0$ Mg/mol)

dewetting at 130°C measured after different dewetting times as indicated in the figure.

Detailed inspection of the dewetting hole topography by atomic force microscopy (Fig. 3) unveiled that the depth of the holes could be much deeper than the film thickness. This indicated that significant substrate deformations incurred by dewetting, manifesting a strong mechanical coupling between visco-elastic film and soft substrate. The deformation of the substrate proved to be elastic and was fully recoverable as verified by removing the PS film via a solvent rinse. Large deformations in the PDMS layer occurred only during stages of dewetting when the PS film was deformed elastically, i.e., at times shorter than t_{rep} . Consequently, for experiments at low temperatures close to the glass transition the influence of film elasticity persisted for longer times. Pushed aside by the opening forces, the material from within the dewetted hole generated a visible rim at the hole perimeter, and simultaneously a similar rim on the substrate side, which we call an “elastic trench” as it deformed the rubbery PDMS layer underneath. Most importantly, this substrate deformation engendered an elastic restoring force which counteracted the driving capillary and molecular recoiling forces in the film. The existence of a trench also caused an increase in frictional resistance for the opening of the hole by augmenting significantly the contact area between PS and PDMS which is proportional to the perimeter of the trench. The shape of the dewetting hole and the depression in the PDMS layer thus have to be related to the balance of the driving dewetting forces in the viscoelastic film, the frictional resistance at the film-substrate interface, and the counteracting elastic substrate deformation. All together caused the slowing down of dewetting with the increase of the thickness of the deformable soft PDMS layer and ultimately allowed only the formation of comparatively small quasistatic holes.

component of the capillary force (i.e., $\gamma \sin\theta$, with γ being the surface tension of PS and θ being the contact angle [23]) was left. At that point, most resistance due to deformation of the rubbery PDMS film was removed and the PS film slipped on the PDMS substrate. Consequently, the dewetting rim became unstable due to a dewetting velocity which now depended on the width of the rim [31]. This rim instability [31,32] generated fingerlike threads of PS which eventually decomposed into droplets.

It was already demonstrated previously [13,18,20] that residual stresses resulting from film preparation can be significantly larger than capillary forces and, at times shorter than t_{rep} , are responsible for the formation of highly asymmetric rims in elastically deformed polymer films. These rims were much larger than ones generated by capillary forces alone [15,16]. As a first approximation, the substrate depression (D), measured inside the hole (see Fig. 3), can be considered as a direct indicator of the local strain in the PDMS layer inside the hole, from which the total dewetting force exerted on the film can be estimated [15–20]. As shown in Fig. 4, the systematic analysis of D made it clear that D reached a maximum value within relatively short time. Later on, D slowly started to decrease. The late stage dewetting process, characterized by a renewed increase in hole diameter and the nucleation of rapidly growing 2nd-stage holes, set-in when the substrate depression decreased substantially. However, in Fig. 4 this stage was only reached for the shorter polymer where the dewetting time exceeded t_{rep} . It is quite revealing that for $t < t_{\text{rep}}$ the hole diameter for both samples in Fig. 4(b) (differing in chain length by a factor of 5) reached about the same quasistatic value of approximately 20 μm . The vanishing of the depression in the soft substrate reflects both the decrease of the residual stresses and the transition to a viscous behavior at times longer than t_{rep} , causing a transition from the initial elastic trench [Fig. 4(c)] to the final viscous trench [Fig. 4(d)]. Holes which were nucleated only after the relaxation of residual stresses were never surrounded by large rims and correspondingly never caused large deformations of the soft substrate. Therefore, equilibration of the trench was fast and the transition to a viscous dewetting behavior occurred soon after hole nucleation.

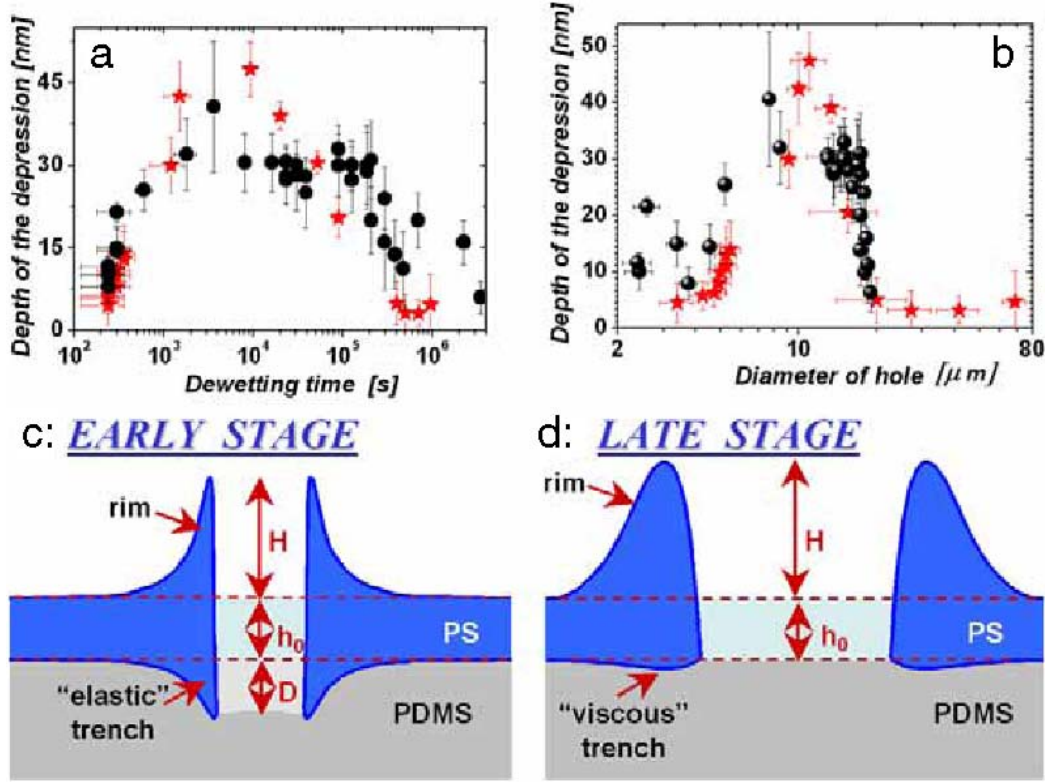


FIG. 4. Depth of the depression within the hole (a) versus dewetting time and (b) versus the diameter of the holes for the samples of Fig. 3 (stars) and a 55 nm PS film ($M_w = 5.0$ Mg/mol) on a 360 nm PDMS layer, dewetting at 130°C (spheres, $t_{rep} = 2.9 \times 10^8$ sec). (c),(d): Schematic representation of the shape of the rim and the trench of a dewetting hole in a PS film deforming the soft rubbery PDMS layer underneath. Because of elastic deformation of the PS film at early stages the corresponding elastic trench is digging into the soft PDMS under-layer quite deeply. At late stages, after the relaxation time t_{rep} , only a small deformation (viscous trench) due to the normal component of the capillary force at the three phase contact line is left in the PDMS layer.

Conclusions:

In conclusion, a novel dewetting behavior of thin polymer films on soft substrates exhibiting two distinctly different stages was revealed. The transition from early to late stage dewetting was found to be governed by relaxation processes in the dewetting viscoelastic film. At times shorter than t_{rep} , due to elastic deformation of the dewetting film amplified by residual stresses [15,16,19], a considerable trench was induced in the deformable substrate. The size of the trench was much larger than what capillary forces alone could have achieved. If such an elastic deformation could be

maintained indefinitely, holes would never grow beyond a maximum diameter determined by the balance of forces driving dewetting and the counteracting elastic force resulting from the induced elastic deformation of the rubbery substrate. However, the elastic behavior of the dewetting film vanished at times longer than τ_{rep} and thus the elastic trench disappeared. At this stage, the polymer behaved like a viscous fluid and dewetting was controlled by slippage, which induced a Rayleigh-type rim-instability [31,32] and led to droplet formation. Consequently, by using deformable substrates, long-lasting metastable films containing only tiny holes can be achieved for times shorter than τ_{rep} . In potential applications, one may take advantage of the often very long relaxation times of polymers. In such cases, one can obtain almost stable films for extended periods of time by simply using soft instead of rigid substrates.

References:

- [1] P.-G. de Gennes, F. Brochard-Wyart, and D. Quéré, *Capillarity and Wetting Phenomena: Drops Bubbles, Pearls, Waves* (Springer, New York, 2003).
- [2] C. Redon, F. Brochard-Wyart, and F. Rondelez, *Phys. Rev. Lett.* **66**, 715 (1991).
- [3] F. Brochard-Wyart, P. Martin, and C. Redon, *Langmuir* **9**, 3682 (1993).
- [4] F. Brochard-Wyart and P. G. de Gennes, *J. Phys. Condens. Matter* **6**, A9 (1994).
- [5] P. Lambooy, K.C. Phelan, O. Haugg, and G. Krausch, *Phys. Rev. Lett.* **76**, 1110 (1996).
- [6] A. Sharma and R. Khanna, *Phys. Rev. Lett.* **81**, 3463 (1998).
- [7] K. Jacobs, S. Herminghaus, and K. R. Mecke, *Langmuir* **14**, 965 (1998).
- [8] S. Herminghaus, K. Jacobs, K. Mecke, and J. Bishcof, *Science* **282**, 916 (1998).
- [9] R. Seemann, S. Herminghaus, and K. Jacobs, *Phys. Rev. Lett.* **86**, 5534 (2001).
- [10] G. Reiter, *Phys. Rev. Lett.* **68**, 75 (1992).
- [11] G. Reiter, *Phys. Rev. Lett.* **87**, 186101 (2001).
- [12] J.-L. Masson and P. F. Green, *Phys. Rev. Lett.* **88**, 205504 (2002).
- [13] K.Y. Suh and H. H. Lee, *Phys. Rev. Lett.* **87**, 135502 (2001).
- [14] G. Reiter and P. G. de Gennes, *Eur. Phys. J. E* **6**, 25 (2001).
- [15] T. Vilmin and E. Raphaël, *Eur. Phys. J. E* **21**, 161 (2006).
- [16] G. Reiter, M. Hamieh, P. Damman, S. Slavons, S. Gabriele, T. Vilmin, and E. Raphael, *Nat. Mater.* **4**, 754 (2005).
- [17] T. Vilmin and E. Raphaël, *Phys. Rev. Lett.* **97**, 036105 (2006).
- [18] M. H. Yang, S.Y. Hou, Y. L. Chang, and A. C.-M. Yang, *Phys. Rev. Lett.* **96**, 066105 (2006).
- [19] P. Damman, S. Gabriele, S. Slavons, S. Desprez, D. Villers, T. Vilmin, E. Raphael, M. Hamieh, S. A.

- Akhrass, and G. Reiter, Phys. Rev. Lett. **99**, 036101 (2007).
- [20] A. C.-M. Yang, M. H. Yang, Y. L. Chang, S.Y. Hou, S.-K. Su, G. Reiter, and A. C. Su (to be published).
- [21] A. C.-M. Yang, B. D. Terris, and M. Kunz, Macromolecules **24**, 6800 (1991).
- [22] A. Carre´ and M. E. R. Shanahan, Langmuir **11**, 24 (1995).
- [23] A. Carre´, J.-C. Gastel, and M. E. R. Shanahan, Nature (London) **379**, 432 (1996).
- [24] D. Long, A. Ajdari, and L. Leibler, Langmuir **12**, 5221 (1996).
- [25] M. E. R. Shanahan and A. Carre´, Colloids Surf. A **206**, 115 (2002).
- [26] M. Voue´, R. Rioboo, C. Bauthier, J. Conti, M. Charlot, and J. De Coninck, J. Eur. Ceram. Soc. **23**, 2769 (2003).
- [27] E. Verneuil, J. Clain, A. Buguin, and F. Brochard-Wyart, Eur. Phys. J. E **10**, 345 (2003).
- [28] A. C.-M. Yang, J. E. Ayala, and J. C. Scott, J. Mater. Sci. **26**, 5823 (1991).
- [29] Lord Rayleigh, Proc. London Math. Soc. **s1-10**, 4 (1878).
- [30] A. Bach, K. Almdal, H. K. Rasmussen, and O. Hassager, Macromolecules **36**, 5174 (2003).
- [31] G. Reiter and A. Sharma, Phys. Rev. Lett. **87**, 166103 (2001).
- [32] S. Gabriele, S. Sclavons, G. Reiter, and P. Damman, Phys. Rev. Lett. **96**, 156105 (2006).

Chapter 6: Grafting Conjugated Macromolecules to Percolated Carbon Nanotubes Network Templates for Optoelectronic Functions

Abstract

To investigate the single molecule behavior and chain conformation effect in the nanocomposites comprised of conjugated polymers and carbon nanotubes, conjugated polymers, poly (3-hexylthiophene) (P3HT) and poly [2-methoxy-5-(2'-ethyl-hexyloxy)-1, 4- phenylene vinylene] (MEH-PPV), were grafted to percolated multiwalled carbon nanotubes via various surface grafting reactions. The grafted conjugated polymers wrapped the nanotubes behaving as a nanometer scale thin film and contributed considerably to the resistivity of the nanocomposites. The resistivity of these polymer thin film can be estimated by a percolation theory. Various polymer coating thickness were prepared via controlling the reaction conditions and the thickness effect on resistivity of the nanocomposites was studied. For comparison, a saturated polymer, polystyrene (PS), was also studied for the unique thickness and percolation effects.

Introduction

Due to the intrically small sizes and high aspect ratios, as well as the various superb physical and mechanical properties¹⁻⁶, carbon nanotubes (CNTs) have been widely explored in blends with other materials in order to fabricate novel nano-composites for significantly improved mechanical, electrical and thermal properties. When CNTs are well mixed with the matrix, they will form a statistical network that percolate the electrical, thermal, or even the mechanical stimuli. Because of their high aspect ratio and high electrical conductivity, a little amount CNTs can provide a percolated network to efficiently increase the electrical conductivity of materials, and therefore CNT networks could be applied in flexible transparent electrodes⁷⁻⁸. The resistivity of CNT networks is composed of two sources: (1) the intrinsic resistivity of CNT and (2) the contact resistivity from the junction between CNTs⁹. However, the van der Waal forces between carbon nanotubes is very strong, so the dispersion of carbon nanotubes is a problem for polymer/CNTs composites. To solve the dispersion problem, polymer is often grafted on CNT to improve dispersion. After grafted with polymer, the resistivity of CNTs junction becomes higher. This will seriously affect the conductivity of polymer/CNT composites and therefore the CNTs junction is an important subject to study. In this study, CNTs was functionalized by surface grafting to improve the dispersion of CNT. Different conjugated polymer coating thickness and material systems were explored.

Experimental Section

MWCNT acid treatment

The MWCNT which was produced by chemical vapor deposition (CVD) (1g) was mixed with H_2SO_4 (98 wt%) and HNO_3 (16M), the volume ratio between H_2SO_4 and HNO_3 is 3:2. The reaction system was refluxed under 150 °C for 1.5 hours to create carboxyl group (-COOH) on the surface of MWCNTs¹⁰. The product was washed with deionized (DI) water by filtration until the solution become neutral, and then dried in the oven with 80 °C.

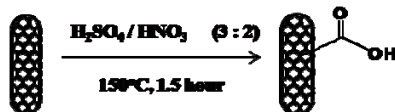


Fig. 1: MWCNT acid-treatment

MWCNT grafting 2-(3-thienylethanol)

The acid-treated MWCNT (100mg) was mixed with thionyl chloride (SOCl_2) and reacted with reflux at 70 °C for half hour. After pumping out the surplus SOCl_2 , 2-(3-thienylethanol) (0.1ml) and pyridine (0.1ml) were added into the reactor, DMAC for the solvent, and reacted for 1day at 90 °C¹¹. The product was washed with toluene and chloroform, and then dried in the oven at 80 °C.

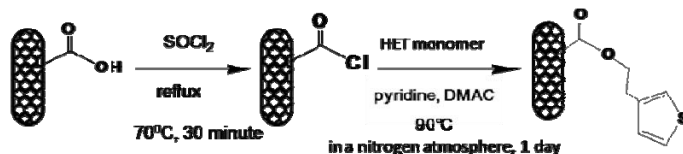


Fig. 2: MWCNT grafting 2-(3-thienylethanol)

MWCNT grafting poly(3-hexylthiophene) step I

MWCNT grafting 2-(3-thienylethanol) (1mg) and 3-hexylthiophene (0.16ml) was dispersed in 7.5ml acetonitrile by ultrasonic cleaner for 3 hours and then added into the FeCl_3 (0.325g) solution which had been dispersed in 2.5ml acetonitrile and added more 30ml chloroform, reacted at 2 °C for half hour. The product was precipitated with methanol and dissolved in toluene. After taking out the free poly (3-hexylthiophene) (P3HT) by centrifuge, MWCNT-g-P3HT was obtained.

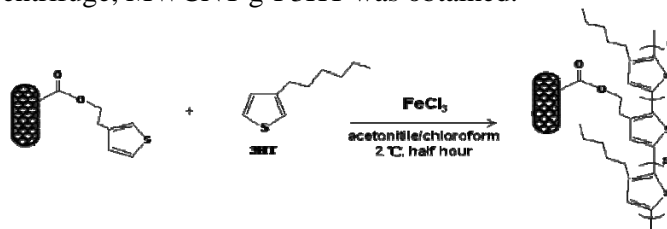


Fig. 3: MWCNT grafting poly (3-hexylthiophene) step I

MWCNT grafting poly(3-hexylthiophene) step II

The product of MWCNT grafting poly (3-hexylthiophene) step I was collected and dispersed by ultrasonic cleaner and added FeCl_3 to increase the coating thickness of P3HT. The product was precipitated with methanol and dispersed in toluene. Free poly (3-hexylthiophene) was removed by centrifuge. Table 1 is the reaction conditions summary of MWCNT grafting poly (3-hexylthiophene) step I and II.

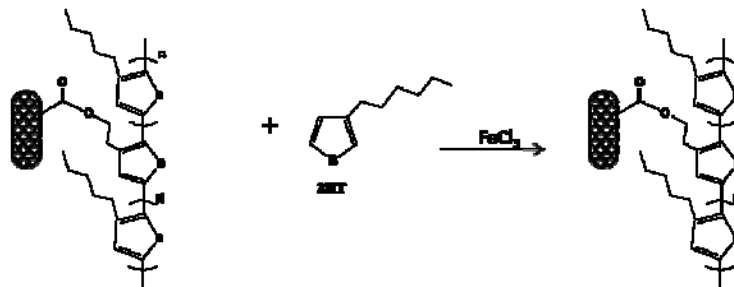


Fig. 4: MWCNT grafting poly (3-hexylthiophene) step II

Sample	Monomer volume (ml)	The amount of FeCl_3 (g)	Volume of CH_3CN (ml)	Volume of CHCl_3 (ml)
Step I	0.16	0.325	10	30
Step II-A	0.16	0.325	0.4	39.6
Step II-B	0.16	0.65	0.4	39.6
Step II-C	0.16	0.65	0	40

Table 1: Summary of conditions to synthesize P3HT grafting on the surface of MWCNTs

MWCNT grafting MEH-PPV

Acid-treated MWCNTs were added with MEH-PPV monomers and pyridine to graft the monomers on the MWCNT surface with ultrasonication in THF solvent. After grafting MEH-PPV monomer on MWCNT, MEH-PPV monomers and (MEH-PPV monomer)-grafted MWCNT were mixed evenly in THF. By slow addition of potassium tert-butoxide (tBuOK)¹² under dark condition at 5°C for 4 hours to grow MEH-PPV on MWCNT surface.

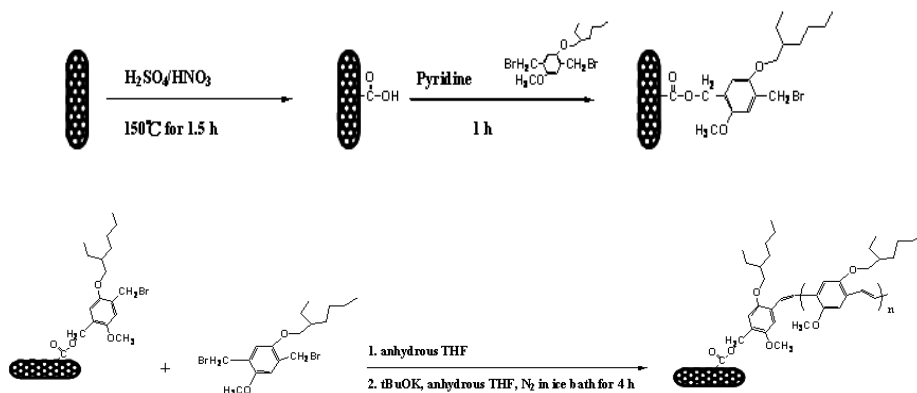


Figure 5: MWCNT grafting MEH-PPV

MWCNT grafting polystyrene (PS)

MWNT-COOH was reacted with sodium ethoxylate (EtONa) under sonication for 1 h to generate MWNT-COONa. MWNT-COONa and 1 ml 4-vinylbenzyl chloride (VBC) were mixed under sonication for 2 h to form MWNT-COOCH₂(C₆H₄)CHCH₂ through eliminating sodium chloride (NaCl). Into a 25 ml flask equipped with a reflux condenser and a magnetic stir bar, MWNT-COOCH₂(C₆H₄)CHCH₂ made from above procedure were added with 3 ml styrene monomer and 5 mg 2,2'-azobis-isobutyronitrile (AIBN) as an initiator at 100°C for 3 h to grow PS chains grafting on MWNTs (PS-MWNT).

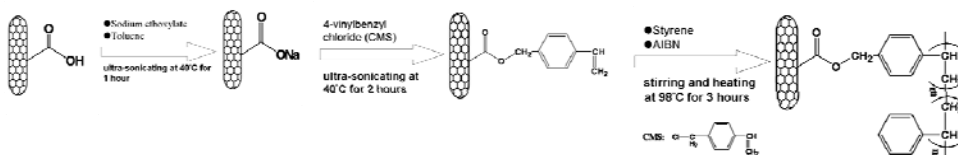


Figure 6: MWCNT grafting PS

Sample for resistivity measurement

Monodisperse PS ($M_w/M_n = 1.3$) of molecular weight $M_w = 2000000$ (Pressure Chemical Co., U.S.A.) was used as the polymeric matrix to blend with different weight ratio MWCNT-P3HT, MWCNT-MEHPPV and MWCNT-PS to form MWCNT-P3HT/PS, MWCNT-MEHPPV/PS and MWCNT-PS/PS composites.

Analysis instrument

The change in the surface chemical bonding of the MWCNTs and the grafting behavior of the hybrid was recorded by Fourier-transformed infrared

spectrophotometry (FT-IR). The morphology and polymer coating thickness were measured by transmission electron microscopy (TEM), JOEL JEM-2010. The weight percentage and of polymer was measured by Perkin-Elmer thermal analysis TG/DTA system at a ramp rate of $10^{\circ}\text{C min}^{-1}$ under argon flow. The photoluminescence spectra of MWCNT-g-P3HT randomly dispersed in toluene were recorded using a Perkin-Elmer LS55 Photoluminescence spectrometer. The absorption spectra of the hybrid randomly dispersed in toluene were obtained using an ultraviolet – visible (UV-vis) spectrometer. The molecular weight of P3HT grafted on the surface MWCNTs was obtained by using Gel Permeation Chromatography (GPC) Waters. Source meter, Keithley 2400, was used to measure the resistivity of polymer-g-MWCNT composite.

Results and Discussions

FTIR spectra

The FTIR spectra of CH stretching frequency region (~ 2800 to 3000 cm^{-1}) and C=H stretching region (~ 3000 to 3200) of MWCNT-COOH, MWCNTs-COCl, MWCNTs-g-HET are shown in figure 7. From the figure it is apparent that the OH stretching frequency shows in MWCNTs-COOH sample and disappears in MWCNTs-COCl, MWCNTs-g-HET. It is clear that every $-\text{COOH}$ group on MWCNTs grafted with monomer HET. The 1450 cm^{-1} peak of MWCNTs-g-HET corresponds to the stretching vibration of thiophene ring.

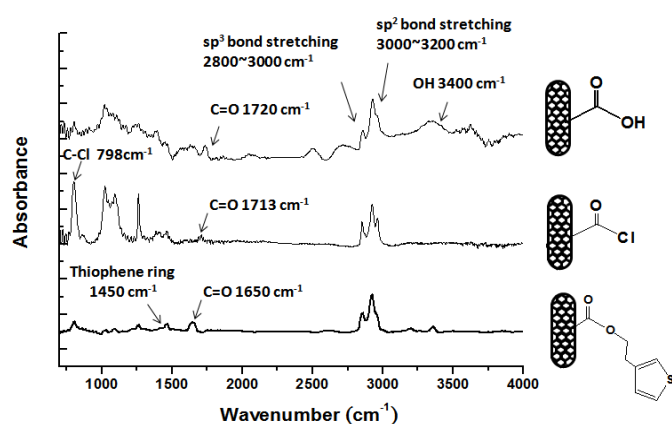


Figure 7: FT-IR spectra of MWCNTs-COOH, MWCNTs-COCl, MWCNTs-g-HET

TEM Observations

Because of the dispersion ability of CNT in different solvent, we need to carry out the polymerization process with 2 steps. First, for the 1st step, acetonitrile was

introduced into the reaction system because of well dispersion of CNT in acetonitrile. Acetonitrile can dissolve FeCl_3 and decrease the reactivity of FeCl_3 ¹³. Figure 8 is the TEM micrographs of step I sample, the coating thickness is about 2.1nm. Figure 9 is the TEM micrographs of step 2 - sample A, the coating thickness is about 3.6nm. From sample A to sample B (figure 10), the thickness doesn't change. We can find the sample C has the thickest coating about 6 nm; however, there're many unremovable particles (figure 11). The possible reasons we have unwashable particles are the crosslink between polymer grafted on CNT and another polymer grafted on CNT and there're polymers wrap around FeCl_3 that we can't wash. To remove the particles have FeCl_3 , the resulting reaction mixture was poured into methanol, and a precipitate formed. This was filtered off and washed with methanol. After that, using ammonia dedoping to remove Cl^- and ethylenediamine tetraacetic acid (EDTA) to remove Fe^{3+} , as suggested by Anderson et.al.¹⁴. From the calculation, the distance between 2 CNTs is about $3.6\mu\text{m}$. It's further than distance for 2 polymers can reach each other. According to the dynamic of CNTs, if we have CNTs touch each other and chemical reaction happens, there's possibility to become crosslinking. To avoid the crosslinking, the ultra-sonic will be used to polymerize in. It's nescessary to separate every MWCNTs-g-P3HT with each other to know clearly the its properties according to the interaction between CNT and P3HT.



Figure 8: TEM micrographs of MWCNTs-g-P3HT of step 1 (error bar: ± 0.6 nm).

(a) The uniform coating of P3HT grafted on CNTs, (b) (c) The network of MWCNTs-g-P3HT.

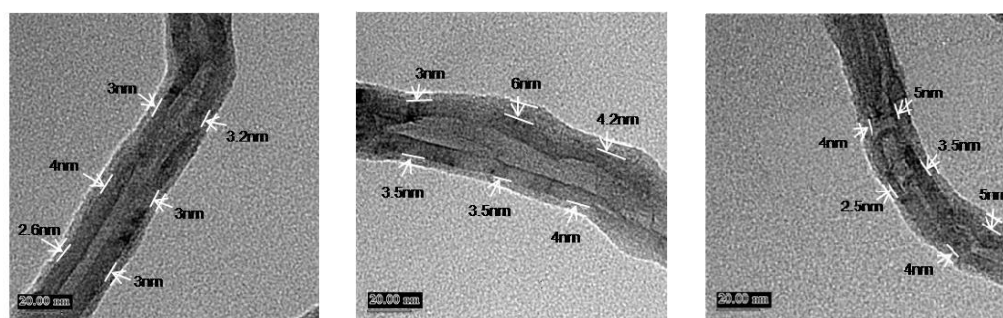


Figure 9: TEM micrographs of MWCNTs-g-P3HT – step 2 of sample A (error bar: \pm

1.1 nm)

Figure 12 shows the MEH-PPV coated MWCNT, the MEH-PPV coating thickness is about 2.9nm. Figure 13 is the SEM micrographs of well dispersed MWCNT-g-PS and the PS coating thickness is about 2nm.

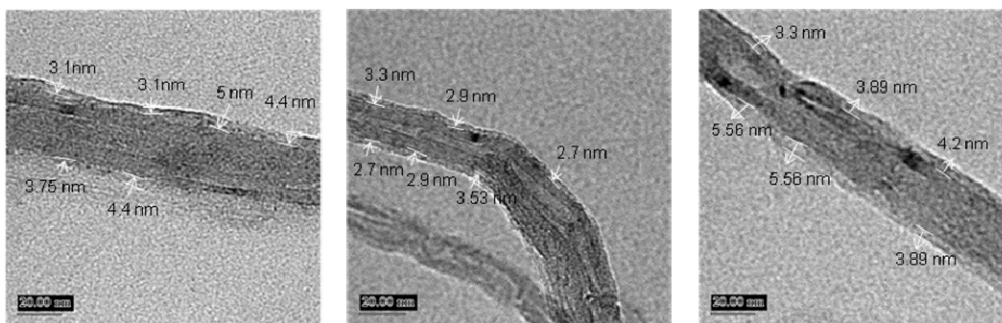


Figure 10: TEM micrographs of MWCNTs-g-P3HT - step 2 of sample B

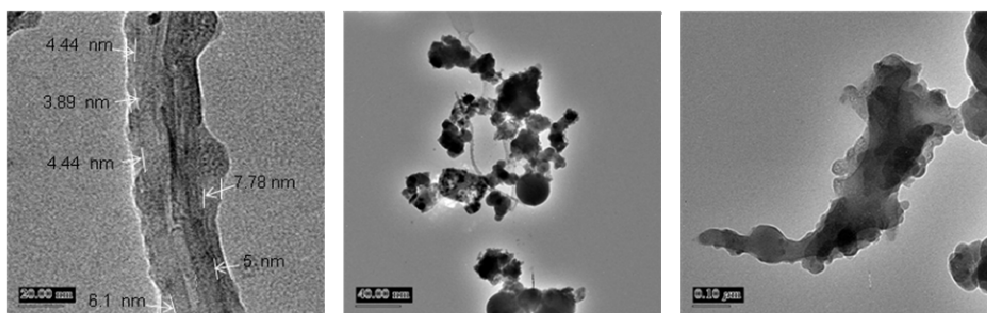


Figure 11: TEM micrographs of MWCNTs-g-P3HT - step 2 of sample C.

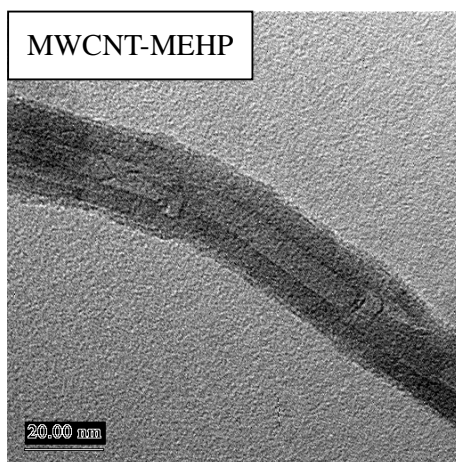


Figure 12: TEM micrograph of MWCNT-MEHPV

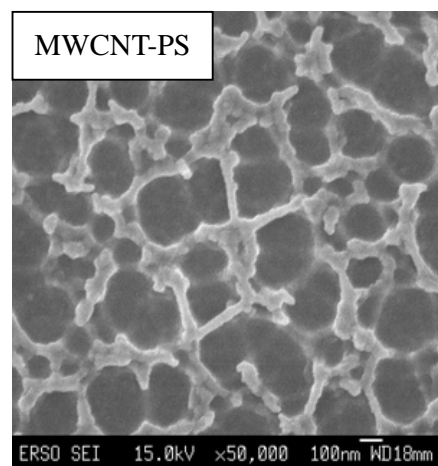


Figure 13: SEM micrograph of MWCNT-PS

Thermogravimetry analysis

Figure 14 is the thermogravimetry analysis data for sample of step I and step II of sample A. Blue line is the P3HT which was defunctionalized from MWCNT-g-P3HT. From the TGA, we can find that P3HT is decomposed from 100°C to 250°C. For sample of P3HT step I and step II of sample A, there also exists obvious weight change in the same range. At 250°C, the weight loss of P3HT step I sample and sample II of sample A are 14% and 24% respectively. From the TGA for MWCNT-MEHPPV and MWCNT-PS, the weight loss of MEHPPV and PS are 18% and 10% (Figure 15).

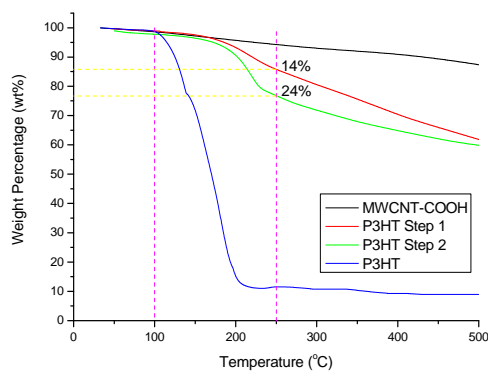


Figure 14: TGA for MWCNT-P3HT step I and step II of sample A

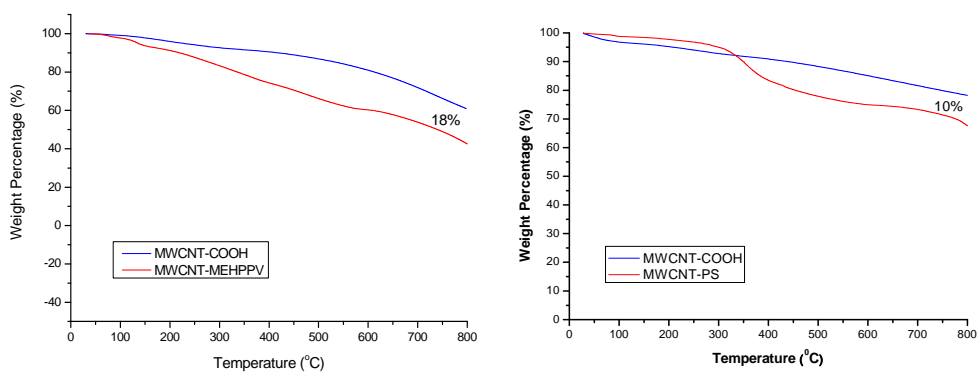


Figure 15: TGA for MWCNT-MEHPPV and MWCNT-PS

Method of thickness measurement	MWCNT-P3HT step1	MWCNT-P3HT step2	MWCNT-MEHPPV	MWCNT-PS
TEM observation	2.1 nm	3.6 nm	2.9 nm	2 nm
TGA estimation	1.4 nm	2.6 nm	1.8 nm	1 nm

Table 2: Polymer coating thickness of MWCNT-P3HT, MWCNT-MEHPPV and MWCNT-PS

By geometry calculation, the coating thickness can be estimated from weight percentage of polymer. The estimated thickness for P3HT step I is 1.4nm; for step II of sample A is 2.6nm. The estimated polymer coating of MWCNT-MEHPPV and MWCNT-PS is about 1.8nm and 1nm respectively. Table 2 is a summary of coating thickness for different polymer grafted MWCNT systems.

Photoluminescence spectra

Figure 16 and 17 show the PL and PLE spectra of step I sample and step II-sample A. The emission peaks of these two samples are around 540nm. Band gap can be found by the cross point of PL and PLE spectra. For step I sample, the band gap is 2.62eV; for step II –sample A, the band gap is 2.58eV.

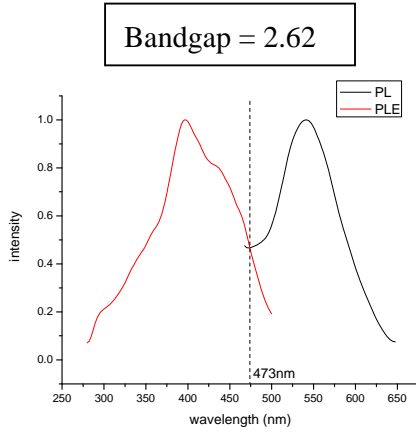


Figure 16:
PL and PLe spectra of MWCNT-g-P3HT
(2.1nm)

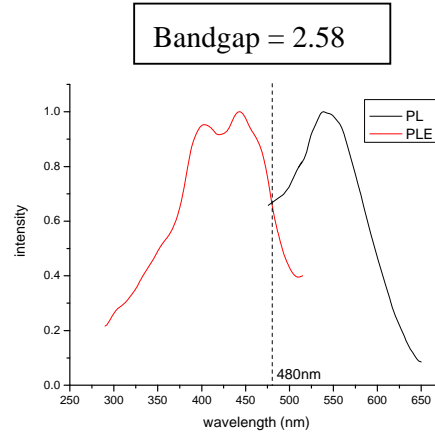


Figure 17:
PL and PLe spectra of MWCNT-g-P3HT
(3.6nm)

Resistivity measurements

The resistivity of polymer-g-MWCNT will be measured via the following method. The polymer-g-MWCNT/PS was prepared as a film between two ITO electrodes and the resistivity was measured by Keithley 2400 source meter. Extra pressure is used to avoid air voids between sample and electrodes. Figure 19 is the chart of different pressure versus resistivity for 100nm PS thin film. Because of air voids, the resistivity is much higher than the resistivity of PS (10^{13} - 10^{16} Ω -cm) when the extra pressure is lower than 1600 Pa. When the extra pressure is larger than 1600 Pa, the resistivity become saturated and approaches to the exact resistivity of PS. From this result, we can find that the air voids will be avoided when the extra pressure

is higher than 1600 Pa.

By means of this method, the resistivity of different MWCNT-g-polymer weight fraction can be measured and the resistivity of MWCNT-g-polymer material will be estimated by percolation theory. Figure 20 is the resistivity of MWCNT-PS with different weight fraction. By the percolation theory¹⁵⁻¹⁸,

$$\rho_{composites} = \rho_c (f - f_c)^{-t}$$

$\rho_{composites}$ is the resistivity of composites for different weight fraction, ρ_c is the resistivity of MWCNT-g-polymer material, f is the weight fraction, f_c is the percolation threshold and t is a constant. For the MWCNT-PS/PS system, f_c and t are 0.05% and 2.7 respectively, and the ρ_c which is calculated from percolation theory is about 2×10^5 (Ω -cm). The contact resistance, R_c , between neighboring nanotubes along the percolated conducting path was presented by Li *et al.*¹⁹ The equation is given by:

$$R = R_c + L \times 6000 (k\Omega/\mu m)$$

which L is the nanotube length meaning the length from one contact point to another one, and the resistivity along MWCNT could be obtained from the result found by Foygel *et al.*²⁰ For MWCNT-PS system the contact resistance, R_c , is about 2.12×10^{12} (Ω -cm) and the contact resistance is contributed from PS thin film which is coated on MWCNT. The thin film resistivity will be measured by device method to compare with the resistivity of PS thin film on MWCNT and the thickness effect of resistivity will also be studied. In the future, the resistivity of MWCNT-P3HT and MWCNT-MEHPPV system will be measured and discussed about the divergence of resistivity for different material.

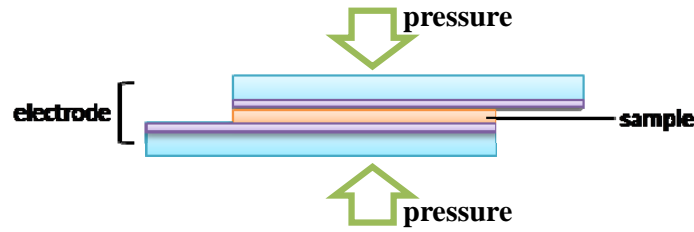
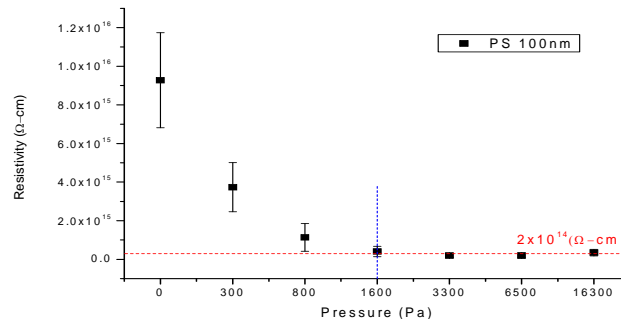


Figure 18: Structure of the device



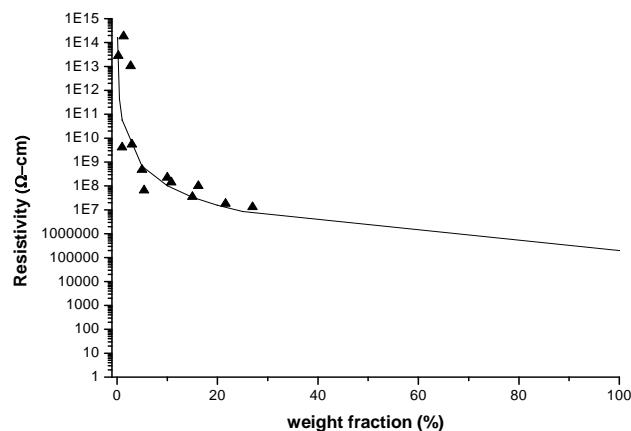


Figure 20: Resistivity of MWCNT-PS/PS

Conclusions

The novel materials, conjugated polymer/MWCNTs (MWCNT-g-P3HT and MWCNT-g-MEHPPV), were synthesized by chemical functionalization method. From TEM observation and TGA estimation, the polymer coating thickness can be well controlled via tuning the reaction conditions. By means of percolation theory and the equation presented by Li *et al.*,¹⁷ the contact resistivity of MWCNT-g-polymer material can be measured. This contact resistivity is contributed by the polymer thin film on MWCNT. In the future, the resistivity of pure polymer thin film will be measured by device method to compare with the resistivity of polymer film on MWCNT. The resistivity of different polymer system and different coating thickness will also be measured to study for the material and thickness effect.

References

- [1] Dalton, A. B.; Collins, S.; Muñoz, E.; Razal, J. M.; Ebron, V. H.; Ferraris, J. P.; Coleman, J. N.; Kim, B. G.; Baughman, R. H. *Nature* **2003**, 423, 703.
- [2] Kilbride, B. E.; Coleman, J. N.; Fournet, P.; Cadek, M.; Drury, A.; Blau, W. J. *J. Appl. Phys.* **2002**, 92, 4024.
- [3] Sandler, J. K. W.; Kirk, J. E.; Kinloch, I. A.; Shaffer, M. S. P.; Windle, A. H. *Polymer* **2003**, 44, 5893.
- [4] F. Leonard; J. Tersoff, *Phys. Rev. Lett.* **1999**, 83, 5174.
- [5] Biercuk, M. J.; Llaguno, M. C.; Radosavljevic, M.; Hyun, J. K.; Fischer, J. E.; Johnson, A. T. *Appl. Phys. Lett.* **2002**, 80, 2767.

- [6] Wei, C.; Srivastava, K.; Cho, K. *Nano Lett.* **2002**, 2, 647.
- [7] Musumeci, A. W.; Silva, G. G.; Liu, J. –W.; Martens, W. N.; Wacławik, E. R., *Polymer* **2007**, 48, 1667
- [8] Ramasubramaniam, R.; Chen, J.; Liu, H., *Appl. Phys. Lett.* **2003**, 83, 2928.
- [9] David, H.; Hu, L.; Grüner, G., *Appl. Phys. Lett.* **2006**, 89, 133112.
- [10] Lin, T. S.; Cheng, L. Y.; Hsiao, C. C.; Yang, A. C. M. *Mater. Chem. Phys.* **2005**, 94, 438
- [11] Philip, B.; Xie, J.N.; Chandrasekhar, A. *Smart Mater. Struct.* **2004**, 13, 295
- [12] Wudl, F.; Srdanov, G. *U.S. Patent*, **1993**, 5, 136
- [13] Olinga, T.; Francois, B. *Synthetic Metals* **1995**, 69, 297.
- [14] Anderson *Macromolecules* **1994**, 27, 6503-6506.
- [15] Muhammad, S. *Applications of percolation theory* **1994**
- [16] Stauffer, D. *Introduction to percolation theory* **1985**
- [17] Deutscher, G.; Zallen, R. *Percolation structure and processes* **1983**
- [18] Grimmett, G. *Percolation* **1989**
- [19] Li, S. D.; Yu, Z. ;Rutherglen, C.; Burke, P. J. *Nano Lett.* **2004**, 4, 2003
- [20] Foygel, M.; Morris, R. D.; Anez, D.; French, S.; Sobolev, V. L. *Phys Rev B* **2005**, 71

Chapter 7: Nano-Mechanical Interactions between Single-Walled Carbon Nanotubes (CNTs) and Entangled Glassy Polymer Chains

Part A. Single-Walled Carbon CNTs Nanocomposites

Abstract

Single-walled carbon nanotubes (SWCNTs) were grafting-functionalized with polystyrene macromolecules and blended into two model polymers: polystyrene (PS, a loose entanglement chain network) and poly (phenylene oxide) (PPO, a tight entanglement chain network). Although the functionalized SWCNTs were drawn into the deformation zones upon imposing external deformation, the mechanical interactions in the length scales of chain entanglements are qualitatively different during the ductile (shear yielding, in PPO matrix) or brittle (crazing, in PS matrix) nanoplastic process. In the dense entangled chain system of PPO, the SWCNTs interacted with the plastic flow by significantly limiting the extensibility of the entanglement network while being drawn into the shear deformation zones (SDZs). This eventually had led to embrittlement of the nanocomposite materials. In contrast, the SWCNTs drawn into the crazes in the loose entanglement system of PS had shown no effects on the extensibility of the entangled chains, behaving as if they are phantom participants to the deformation. The observations shed important light on the fundamental behavior of glassy polymer chain during plastic flow and illustrate fundamental characteristics of the mechanical interactions between glassy polymer chains and the finely dispersed SWCNTs in this type of nanocomposites.

Introduction

It is well-known that glassy polymers under an external stress would yield, undergo plastic flows, and develop plastic deformation zones before their ultimate fractures.¹⁻¹⁶ Crazes and shear deformation zones (SDZs) are the local plastic deformation zones, precursors of brittle and ductile polymers, respectively. Crazes are crack-like defects that are bridged by many fine fibrils (diameters 6~20 nm) between the two surfaces and embedded in voids. The fibrils are drawn from the strain-softened polymer bulk at a constant value of fibril extension ration λ_{craze} (~400% for polystyrene) that are load-bearing.¹⁻¹³ Yang et al. used the atomic force microscopy method and discovered that crazes produced by micronecking process.⁷⁻⁸ However, if the micronecking mechanism can be suppressed, the superplastic behavior occurred, the brittle film become very tough material.⁸ Shear deformation

zones (SDZs) are not fibrillated as in a craze but consists of polymer drawn to a uniform extension ration λ_{SDZ} (~200% for poly (phenylene oxide)). No voids and fibrils structure observed in SDZs.¹⁴⁻¹⁶ The occurrence of crazes or SDZs depends on the entanglement density (v_e) of the load-stretched polymer network.

The strong interest in polymer composite materials based on carbon nanotubes (CNTs) dispersed stems from their extraordinary mechanical, electrical, and thermal properties. However, to date in most case, the carbon nanotube reinforced polymer composites their modulus and strength have shown only least 2 orders of magnitude lower than the theoretically predicted by composite theory.¹⁷ Which strongly depends on the molecular level interaction between CNTs and polymer chains. Therefore, to unveil the load-bearing status of the CNTs with polymer chain in composites is a major work present-day, which provides the opportunity of the function optimization for CNTs in composites.

Previously, the interaction between the nanoplastic flow and the uniformly dispersed surface-grafted multiwalled carbon nanotubes (MWCNTs) during micronecking process (nanoplastic flows) was explored in two model polymer systems, polystyrene (PS) and poly (phenylene oxide) (PPO), representing respectively brittle and ductile polymer.¹⁸⁻²⁰ The results revealed that stretched the glassy polymer of low entanglement density (in PS system), in which movement scale the polymer chains only slipped MWCNTs. Between polymer chains and carbon nanotubes has no mechanical forces connection. Therefore, the micronecking process in these glassy polymer chains was not altered by MWCNTs. On the contrary, in a ductile polymer with high entanglement density system (in PPO system), between carbon nanotubes and polymer chains have strongly nanomechanical interaction, during micronecking process. Consequently lead to the competition between carbon nanotubes local bending and local debonding, and shows different hardened behavior.

Consistent with MWCNTs, Single-walled carbon nanotubes (SWCNTs) also show extremely high tensile modulus (~1TPa) and high fracture strains (estimated to be 10-30%).²¹⁻²² Nevertheless, SWCNTs has a lager aspect ratio than MWCNTs in a same length, because of the diameter of SWCNT was only 1 to 2 nm, which very close to the diameter of the confining tube for a single polymer chain ($D_{chain} = 0.94nm$ for a PS chain). In this study, further investigation of the interaction between the surface-modified single-walled carbon nanotubes and glassy polymer chains during the nanoplastic flows of crazing or shear yielding in nanocomposites. On the other

hand, the effect of polymer entanglement density (ν_e) was also explored in PS/PPO blend nanocomposites.

Experimental Section

Monodisperse PS of molecular weight (Mw) of 2000k g/mol. (Pressure Chemical Co., U.S.A.) and PPO polymer with Mw = 244k g/mol. (Aldrich Chemical Co.) were used as-received. The SWCNTs (AETC Co., Taiwan) purified to >95% and average outer diameter around 1-3 nm and a length in the range of 10-20 μ m.

Synthesis of Surface-grafted SWCNTs

The method used here for preparing the surface grafted SWCNTs with long PS chains (PS-g-SWCNTs) was carried out with three successive steps. First, SWCNTs were surface-treated to anchor carboxylic acid groups onto the external tube surfaces (SWCNTs-COOH). Esterification of the carboxylic acid groups was then carried out by reactions with 4-vinylbenzyl chloride to produce -COOR groups grafting on the tube surfaces (SWCNTs-COOR). Finally, polymerization of the styrene monomers with SWCNTs-COOR grew PS chains on SWCNTs. The free polymers (unbounded polymers) were removed by a series of solvent washes. The average molecular weight of the grafted PS in PS-SWCNTs was measured to be around 38k g/mol (polydispersity=2.2) from gel permeation chromatography after the defunctionalization process.²³ The weight fraction of grafted PS on the SWCNT was determined from thermogravimetric analysis (TGA), to be approximately 61 wt%. The average length of PS-g-SWCNTs is around 2-5 μ m. Figure 1a shows a TEM image of the surface-grafted SWCNTs with PS. The surfaces of SWCNTs are covered by amorphous materials, which attributed to the attached PS chains. However, due to the large van der Waals force stemming from large surface areas, the SWCNTs often forms bundles even after surface modification. In this study the diameter of the surface-grafted SWCNT bundles range from 2 to 5 nm.

Preparation of Nanocomposite Thin Films

To fabricate free-standing composite films onto a supporting copper grid for mechanical experiments,^{1,5,7,18-20} the grafted SWCNTs were then mixed with the neat PS (or PPO, or PPO-PS blends) in toluene and spincoated on clean glass slides from the solution with film thickness controlled approximately 0.5 μ m (τ_0). The weight

fraction (c_0) of SWCNT in composite films were from 0 to 15 wt% (equal to 0 ~11.7% in volume fraction). Before the mechanical testing, aging at 120°C for 1h was routinely carried out for SWCNTs/PPO, PPO-PS and SWCNT/PPO-PS blend films to enhance the strain localization required for growing DZs.¹⁴⁻¹⁵

Microdeformation Zones Characterization

Microdeformation zones (crazes and SDZs) are studied by copper grid technique and reported elsewhere.^{7,8,18-20} The applied strain rate was restricted about 2×10^{-4} /s. To characterize the depth and width of deformation zones, the stretched samples were then examined under an AFM (Digital Instrumental, Nanoscope IIIa).^{4-8,18-20} The AFM topographic data were used to calculate the local stress and strain information in the deformation zones.^{4-8,18-20} A transmission electron microscope (TEM, JOEL JEM-2010, with acceleration voltage of 200 KeV.) was used to obtain images of SDZs or crazes of the stretched samples, which were cut a section from the copper grid.^{4-5,7,18} The widening velocities of SDZs or crazes were obtain from the images of the deformation zones growing that was recorded by a video camera attached to an optical microscope.²⁰

Results

Stretching entangled glassy polymer under external stress, the localization of strain is induced by intrinsic strain softening and evolved into nanoplastic flow of crazing or shear yielding, which depends on the entanglement density ν_e . Specifically, in a loose polymer network with $\nu_e < 4 \times 10^{25}$ chains/m³ undergo craze deformation, leading to brittle failure. On the contrary, for a tight polymer network with $\nu_e > 8 \times 10^{25}$ chains/m³ shear deformation zone prevails, while both craze and shear yielding coexist in the regime of $4 \times 10^{25} < \nu_e < 8 \times 10^{25}$.^{4-6,24-26}

Effects on Morphology and Chain Friction in Crazes

In the pristine PS films (of Mw = 2M g/mol. , $\nu_e = 3.3 \times 10^{25}$) is a classic loose chain network, which undergo craze deformation at room temperature. The crazes initiated at approximation 1% strain (ϵ) and the crazes were generally straight, craze depth d increased linearly with craze width w until the width reached a critical value w_c (for 0.5 μ m thick PS, $w_c \sim 2.5\mu$ m) above which the craze necking becomes mature.^{7-8,18-20} The local fibril breakdowns within the craze at strain increased to approximately 8%

and maximum width of crazes could reach approximately 20 μm (Figure 2a).¹⁸⁻²⁰ It is known that the mechanism of craze failure is due to the existence of concentrating stress at intrinsic weak site and lead to fibrils breakdown within the craze. The fibril breakdown in PS crazes always initiated at the craze–bulk polymer interface.⁵ From the TEM observe (Figure 1b) within the craze in pristine PS film, clearly shows that fibrils and voids are existence inside craze.

The morphology of the SWCNTs/PS composites with different SWCNTs content (c_0), c_0 's from 2 to 15 wt% were show quite different with pure PS. In contrast, the crazes were generally narrow and short in the SWCNTs/PS films (Figure 2 parts b to e). On the other hand, the number of local deformation zone gradually increased with c_0 and only very local breakdowns were observed at strains greater than 20%. From AFM craze topography, in SWCNTs/PS films the craze depth d increased linearly with craze width w , and reached w_c the depression becomes leveling (d_s). The leveling depth d_s is related to fibril draw ratio (λ_{craze}) in craze.^{2-5,9-13} It was found to follow almost the same d versus w curve of the pristine PS (Figure 3a). These results strongly indicated that the incorporation of the SWCNTs in the nanoplastic flow the micronecking characteristic was not influenced by the presence of SWCNTs (Figure 3a inset), which corresponding to the extensibility of fibril was no changed. However, embrittlement occurs at $c_0 > 20$ wt% (Figure 2f).

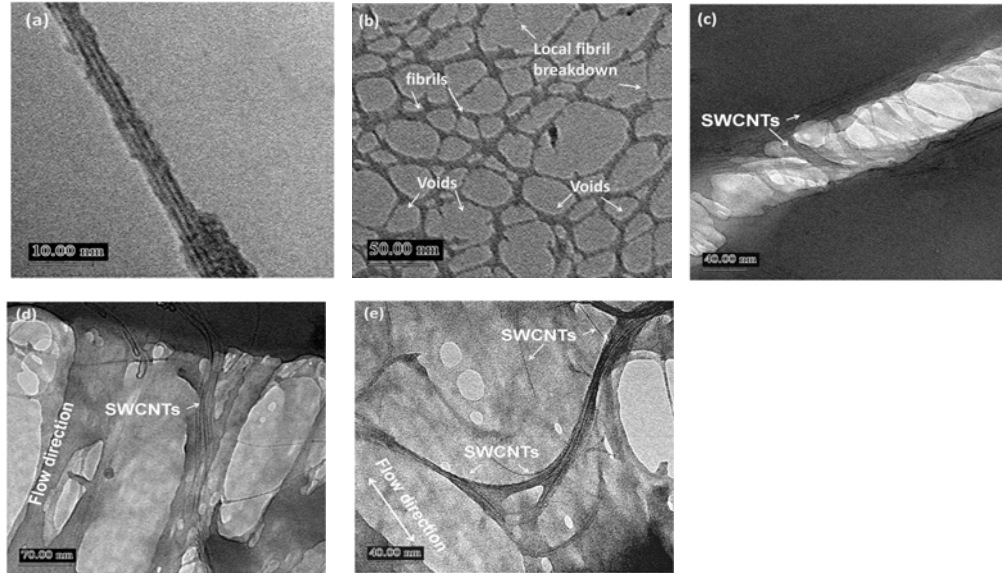


Figure 1. TEM micrographs of (a) SWCNTs-grafted PS, (b) craze microstructure, (c) a craze tip in SWCNTs/PS films ($c_0=15\text{wt\%}$), (d) and (e) wider crazes in SWCNTs/PS films ($c_0=15\text{wt\%}$).

From the TEM observed of embedded SWCNTs in PS (Figure 1 parts c to e, $c_0=15\text{wt.}\%$). Figure 1c shows a TEM micrograph of craze tip penetrates through the SWCNTs, and which seem no effect on the growth of the craze. This phenomenon is due to that the SWCNTs can strain elastically in the narrow crazes ($w>0.6\mu\text{m}$), which was also observed in the MWCNTs/PS composites.²⁰ Within the wider crazes (Figure 1d and e) the SWCNTs were found to draw into the crazes. On the other hand, it also shows that the SWCNTs are very flexible they can be buckled inside the crazes. The AFM topography (Figure 3b) of the mildly etched craze by oxygen plasma,^{18,20} it did not show any protrusions at the craze boundaries. Clearly, the SWCNTs were not pileup at the boundaries of the craze. This result was consistent with the TEM observation, SWCNTs can be drawn by the nanoplastic flow into the craze.

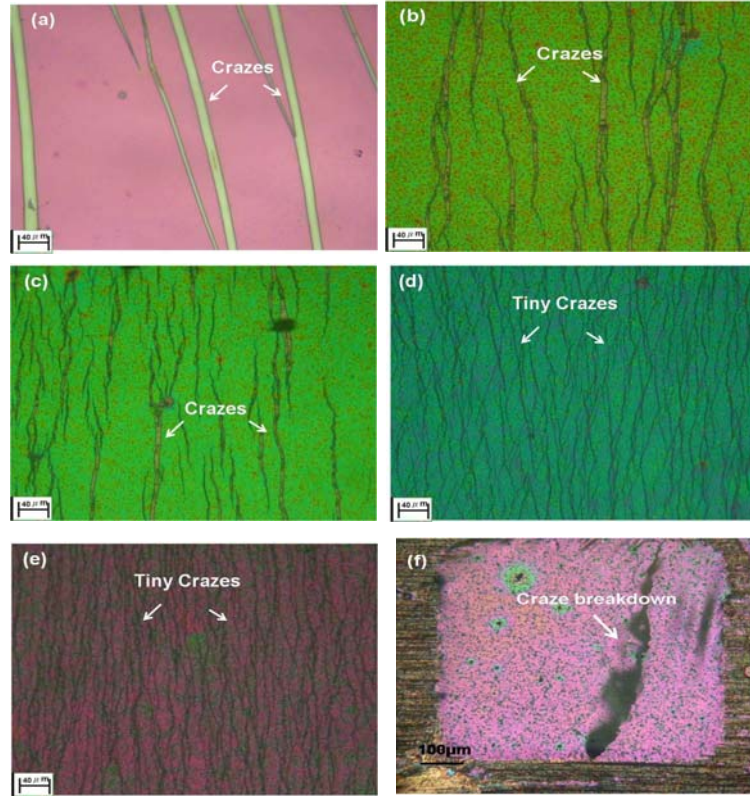


Figure 2. Optical micrograph of stretched (a) pristine PS films and SWCNTs/PS composite film (b) $c_0 = 2\text{ wt}\%$, (c) $c_0 = 5\text{ wt}\%$, (d) $c_0 = 7\text{ wt}\%$, (e) $c_0 = 15\text{ wt}\%$, (f) $c_0 = 20\text{ wt}\%$

The chain friction coefficient (ζ_T) of the nanoplastic flow in deformation zones can be estimated by using a Rouse chains model.²⁰ For a constant force (f) applied to a polymer chain and pulled it with constant sliding velocity (v) during the nanoplastic flow process. The total frictional coefficient relation force and velocity can be described as $f = v \zeta_T$.^{27,20} The pulling force f can be determined from the drawing

stress during crazing and the cross-sectional area of the confining tube of single polymer chain.²⁰ On the other hand, the chain sliding velocity was calculated from the craze widening speed.²⁰ Figure 3c shows the chain sliding velocities during the nanoplatic flow process in pristine PS and SWCNTs/PS films, the v 's were decreases slightly with craze winding until it levels (v_s) as w reached the critical width w_c . The decrease of v apparently is due to strain hardening during the micronecking. However, the chain sliding velocities at steadily state in both pristine PS and SWCNTs/PS films were almost constant (~ 6000 nm/s).

The chain friction coefficient ζ_T of the nanoplatic flow in pristine PS was increased with craze width and in the steady-state necking regime ($w > w_c$) was calculated to be $\zeta_T = 1.1$ kg/s (Figure 3d). The incorporation of SWCNTs in the nanoplatic flow, the chain friction coefficient ζ_T was found to gradually increase with c_0 . The addition of the SWCNTs 15 wt % in PS had raised the chain friction to $\zeta_T = 6.9 \times 10^{-5}$ kg/s. However, increased the chain friction coefficient will restricted the widening of existing crazes and forcing other regions produce new crazes to absorb the applied strain which toughened the SWCNTs/PS films (Figure 2 parts, a to e). Nevertheless, when SWCNTs content increase to above 20 wt% the craze initiation would eventually be suppressed and embrittlement occurred.

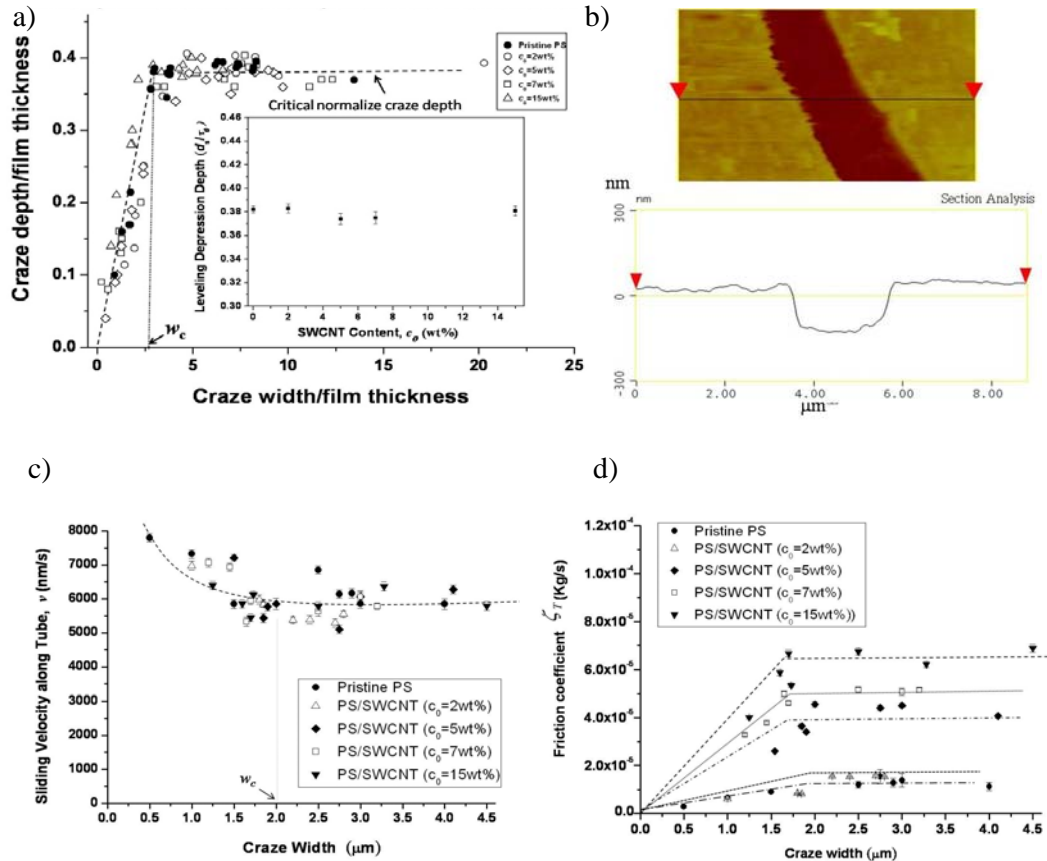


Figure 3. (a) Craze depth d vs craze width w in the PS and SWCNT/PS films. Inset: The Leveling depression depth vs c_0 , (b) AFM micrograph of stretched and etched SWNTs/PS film ($c_0=15\text{wt}\%$), (c) the tube sliding velocity of a PS chain versus craze width in pristine PS and SWCNT/PS films, and (d) the friction coefficient of a PS chain versus craze width in pristine PS and SWCNT/PS films.

Effects on Morphology and Chain Friction in SDZs

The PPO has a tighter entanglement network ($v_e=1.5\times 10^{26}$) compared to the PS. In pristine PPO film shows that the SDZs initiated at approximately $\epsilon = 2\%$, generally straight and broke down to from void for ϵ up to 13%. Before crack the maximum width of SDZs could reach approximately $40\text{ }\mu\text{m}$ (Figure 4a). Figure 4d shows a TEM micrograph of SDZ, the SDZ was different from crazes, smoothly and no voids as well as fibrils structure could be observed in SDZ. However, shear yielding is also a micronecking process.^{15,20}

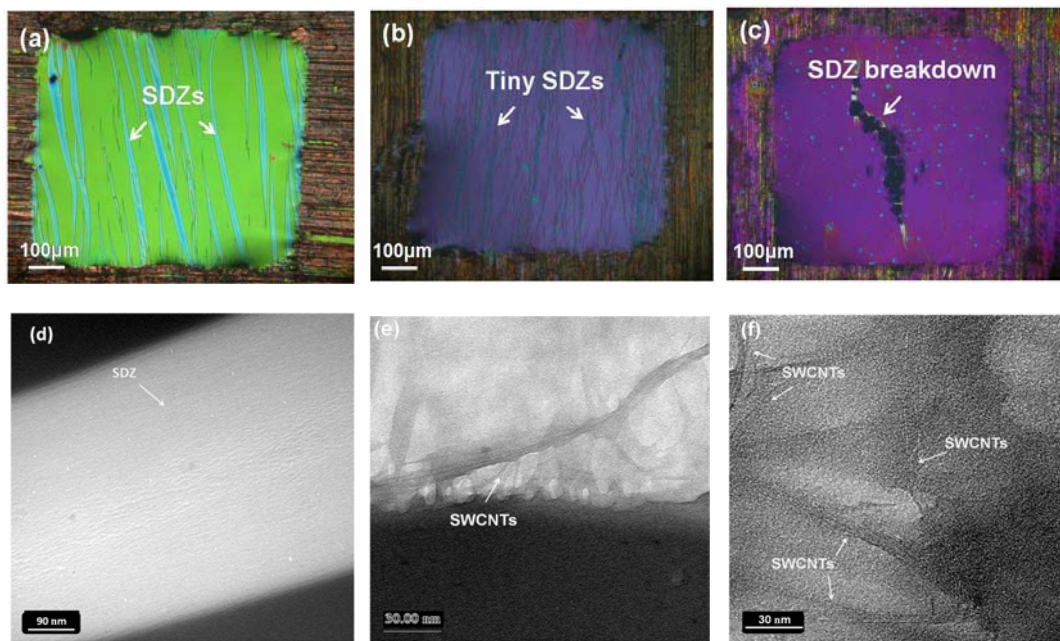


Figure 4. Optical micrograph of stretched (a) pristine PPO films, SWCNTs/PPO composite film (b) $c_0 = 2\text{ wt}\%$, (c) $c_0 = 5\text{ wt}\%$. and (d) TEM micrograph of SDZ in PPO film, (e) and (f) TEM micrographs of SDZ in SWCNT/PPO film ($c_0=2\text{wt}\%$).

Incorporation SWCNTs into PPO matrix, however the morphology of SDZs was quite different as pristine PPO film. The SDZs become more short and narrow ($w < 15\mu\text{m}$) for $c_0=2\text{ wt\%}$ (Figure 4b) and the film undamaged for strain up to 16%. On the other hand, similar to the SWCNTs/PS system, the SWCNTs were can be drawn into the SDZs via plastic flow process (Figure 4e and 4f, $c_0=2\text{ wt\%}$). Nevertheless, a quite different to that observed in MWCNTs/PPO system,²⁰ no local debonding could be observed at the interfaces between the SWCNTs and polymer matrix. This result was due to that the SWCNTs have a small bending moment compared with MWCNTs, thus the deformation between SWCNTs and polymer chain become more identical during the plastic flow. Figure 5a shows the SDZs depth d versus w curve of the pristine PPO and SWCNTs/PPO nanocomposties. In both systems the SDZs depth d also increased linearly with craze width w , and reached w_c the depression becomes leveling (d_s), but the slopes are show different. These results were due to that embedded of SWCNTs in the nanoplastic flow of SDZs could be accelerated strain hardening of the flow. In addition, the leveling depression d_s decreased as c_0 increased (Figure 5a and inset). The leveling depth d_s is related to the draw ratio of plastic flow (λ_{SDZ}) in SDZs, $\lambda_{\text{SDZ}} \sim \tau_0/(\tau_0-2d_s)$.^{9-11,20} The decrease of (d_s/τ_0) from 0.25 ± 0.03 to 0.11 ± 0.01 for pristine PPO film to $c_0=5\text{wt\%}$, according to λ_{SDZ} decrease from $200\pm28\%$ to $128\pm3\%$. However, these results strongly suggest that the SWCNTs not only can affect the micronecking process but reduced extensibility of the entanglement network of the PPO matrix. Embrittlement occurred at $\epsilon = 6\%$ as the SWCNTs content increase to 5 wt% (Figure 4c).

Both in pristine PPO and SWCNTs/PPO systems, the tube sliding velocities (v 's) measured from the SDZs widening, and show in Figure 5b. The v 's in both systems were show slowly decrease with w and leveling at $w > w_c$, they were almost constant ($\sim 1200\text{ nm/s}$). On the other hand, the chain friction coefficient ζ_T in plastic flow was also estimated by use of the Ruse chains model. For pristine PPO films, the chain friction coefficient in the steady-state necking region was calculated to be $\zeta_T = 4.3 \times 10^{-5}\text{ kg/s}$ (Figure 5c). The addition of the SWCNTs in PPO had gradually raised the chain friction with c_0 , the $\zeta_T = 6.7 \times 10^{-5}\text{ kg/s}$ was obtained in SWCNTs/PPO with $c_0=5\text{wt\%}$. However, these phenomena are quite similar to SWCNTs/PS systems.

Effect of Polymer Entanglement Density v_e

It is well know that the entanglement density (v_e) can significantly affect polymer

$$v_e = \frac{\rho N_A}{M_e}$$

mechanical behavior, ν_e can be defined as:

$$(1)$$

where ρ is the density of the polymer, N_A is the Avogadro number and M_e is the molecular weight between entanglements.^{7,9,25} In the PPO-PS blend systems, the molecular weight between entanglements $M_e(\chi)$ depends on the M_e of PS ($\sim 17,000$ g/mol.) and the fraction (χ) of the PPO in blend:³¹

$$M_e(\chi) = \frac{M_e(PS)}{1 + 3.2\chi} \quad (2)$$

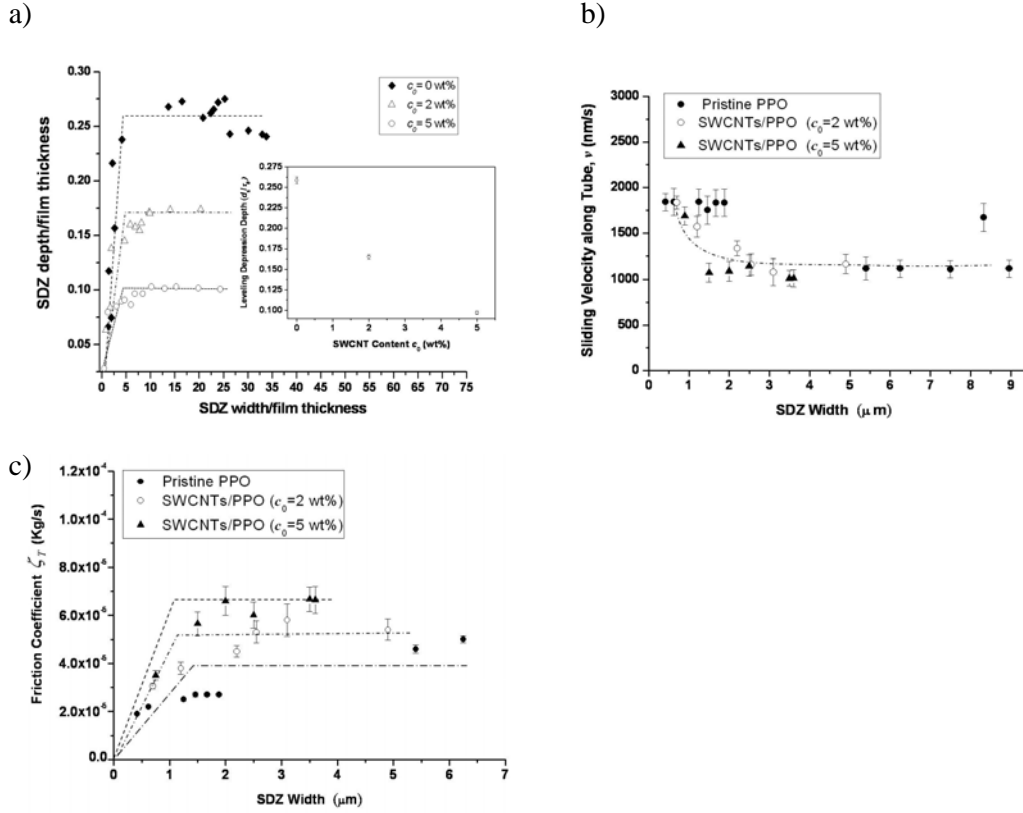


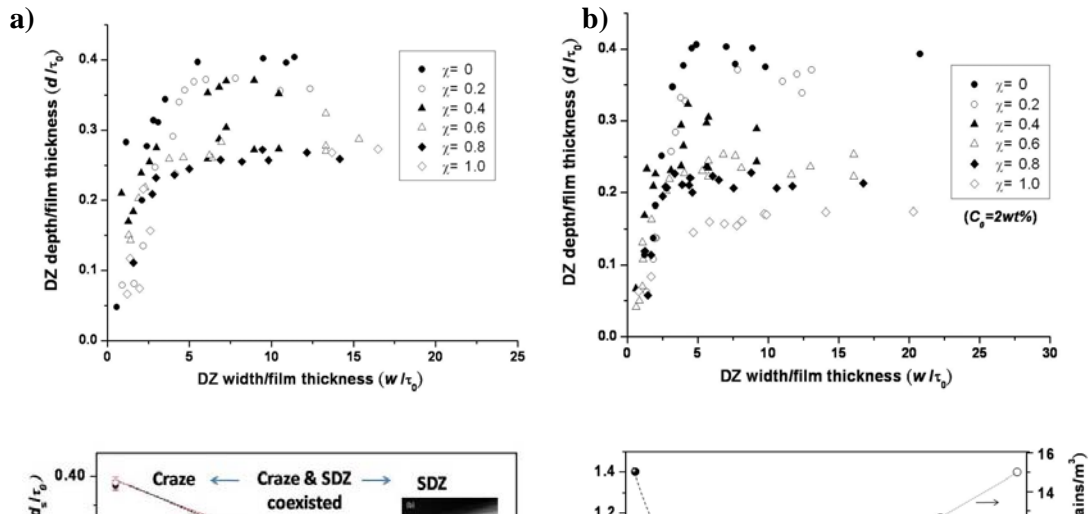
Figure 5. (a) SDZ depth d vs craze width w in the PPO and SWCNT/PPO films. Inset: The Leveling depression depth vs c_0 , (b) the tube sliding velocity of a PPO chain versus craze width in pristine PPO and SWCNT/PPO films, and (c) the friction coefficient of a PPO chain versus craze width in pristine PS and SWCNT/PPO films.

Therefore, the entanglement density of PPO-PS blends can be altered by change the blending ratio between PPO and PS (Figure 6d). In figure 6a shows that deformation zone depth d varied with deformation width w in the pristine PPO, PS and PPO-PS

blends (v_e form 1.5×10^{26} chains/m³ for pure PPO to 3.3×10^{25} chains/m³ for pure PS).

A typical micronecking characteristic was observed in all films, the deformation zone depth increased linearly with w ($w < w_c$) and d become leveling off when $w > w_c$. However, the leveling depression d_s have larger fluctuation in the PPO containing 40wt % and 60wt % of PPO-PS blends. Form the TEM observation, in these blends region crazes and SDZs are coexisting in films (Figure 6d inset). Incorporation of SWCNTs ($c_0=2$ wt %) in PPO-PS blends, d also increased with w when $w < w_c$ and saturated in the steady-state necking regime (Figure 6b). However, the leveling depression d_s are dramatically different between the neat PPO-PS and SWCNTs/PPO-PS blends in high entanglement density regions ($v_e > 8.07 \times 10^{25}$ chains/m³, $\chi > 0.4$). The leveling depression d_s versus weight fraction of PPO (χ) show in Figure 6c.

In the neat PPO-PS blends, the d_s were decreased as χ increased. When $\chi \leq 0.2$ only crazing shown in blends, χ between 0.4 and 0.6 the crazing and shear yielding coexisted. When $\chi \geq 0.8$ only shear yielding was observed in blends. This is a typical craze-SDZ transition curve.^{2,9} In the SWCNT/PPO-PS blends ($c_0=2$ wt%), at low entanglement density v_e samples ($v_e < 6 \times 10^{25}$, $\chi \leq 0.2$) the leveling depression d_s almost the same trend as in neat PPO-PS blends. However, the d_s are dramatically different between the neat PPO-PS and SWCNTs/ PPO-PS in high entanglement density blends ($\chi \geq 0.4$). The upper and lower limit of d_s in PPO-PS blend (with $\chi=0.4$) are 0.345 and 0.306 respectively, that dramatically reduced to 0.315 and 0.251, for $c_0=2$ wt%. On the other hand, in the PPO-PS blend with $\chi=0.6$ and $c_0=2$ wt%, the crazing can be suppressed by addition the SWCNTs, only SDZs can be observed in composite film. These results reveal that the SWCNTs affect extensibility of the entanglement network strongly depends on the entanglement density v_e of polymer matrix.



c)

d)

Figure 6. (a) SD depth d vs SD width w in the PPO-PS blends, (b) in the SWCNT/PPO-PS blends ($c_0=2\text{wt}\%$), (c) Leveling depression depth as function of PPO in PPO-PS and SWCNT/PPO-PS blends, and (d) Entanglement density and Hardening strain as function of PPO in PPO-PS.

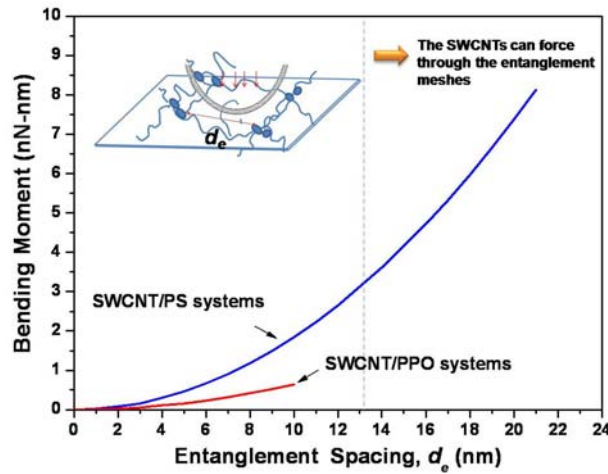


Figure 7. Bending moment vs entanglement spacing d_e .

Discussions

Plastic Flow Induced SWCNT Bending

The glassy polymer chains in the nanoplastic flow of crazing or shear yielding were able to pull the SWCNTs into the local deformation zones. However, in plastic flow of crazing, the draw ratio of the entanglement chain network and the micronecking characteristic were not altered by SWCNTs. In contrast, the SWCNTs within the shear deformation zones (SDZs) considerably limited the PPO chains extension during the nanoplastic flow process and altered the micronecking characteristic. Actually, the draw ratio of plastic flow was strongly depending on the effective

entanglement density (v_{eff}) of polymer matrix.³² Therefore, the draw ratio of plastic flow was reduced by SWCNTs also can associate with that the v_{eff} was increased by incorporated SWCNTs. During the plastic flow process, the shear force should trigger the SWCNTs readily bend under flow, and eventually the SWCNTs were aligned to the flow direction. However, the v_{eff} can be affected by the bend situation of SWCNTs which depending strongly on the geometry of flows and SWCNTs. The microstructure of a craze in a polymer films (films thickness > the order of 10^2 nm) can be described as a three-dimensional fibrils structure with voids between fibrils.^{2,9-13,33} Accordingly, the SWCNT must entail significant modification when it was drawn into the craze. This modification could occur by plastic flow induced the SWCNT bending.

The flow induced deformation of single fibers with high aspect ratio in simple shear flow has been theoretically and experimentally studied.³⁴⁻³⁷ They were show that the bending situation of fibers in shear flow strongly depends on the flow properties as well as geometry of suspending fibers. Here the entangled plastic flow induce SWCNTs bending, we can consider that the SWCNTs directly interact with polymer network during the plastic flow. Which are similar to the SWCNTs interact with high porosity membrane.³⁸ Therefore, the bending moment of SWCNT in plastic flow can be calculated by the bending beam supported on both ends model:³⁹

$$M_b = FL/8 = \tau AL/8 \quad (3)$$

Where F is the bending force by plastic flow, τ is the steadily state necking stress of plastic flow ($\tau = 94$ MPa for PS, $\tau = 33$ MPa for PPO), L is the suspended length (may correspond to mesh size of polymer network d_e), A is the cross-sectional area. From the theoretical calculated by eq. 3, figure 7a shows that bending moment versus the suspended length of SWCNTs in plastic flows. In both systems, if we consider the suspended length depend only on the mesh size of polymer network and no changed during the plastic flow process ($d_e = 9.6$ nm for PS and $d_e = 4.7$ nm for PPO). The M_b in PS and PPO systems can calculated to be 0.17 and 0.14 nN-nm, respectively. It is smaller than the kink moment of SWCNT (~ 13 nN-nm).⁴⁰⁻⁴¹ On the other hand, the critical bending buckling curvature k of SWCNT under bending deformation varies as inverse square of the tube radius and can be calculated as:⁴⁴

$$k = \frac{t/r^2}{\sqrt{3(1-\nu^2)}} \quad (4)$$

Where t is the effective wall thickness of the tube (varies from 0.04 to 0.07 nm depends on the inter-atomic potential and simulation details)⁴⁵⁻⁴⁶, ν is the Poisson ratio

of the tube's material ($\nu = 0.17-0.19$ for graphite), r is radius of SWCNT. From eq. 4 the k of SWCNT can estimate to be 0.1553 nm^{-1} . Which corresponding to the diameter of curvature of SWCNT $D_{\text{curvature}} = 2/k = \sim 13 \text{ nm}$. This result suggests that if mesh size of polymer network $d_e > 13 \text{ nm}$ during plastic flow, the SWCNTs can pass through the entanglement network mesh by buckling.

Modification of Entanglement Network during Plastic Flow Process

During the plastic flow process, the entanglement networks were bore large stress and stain especially for nanoplatic flow of craze. Since the generation of voids, necessary for the formation of the craze fibril structure, must entail significant modification of entanglement network (become an inhomogeneous flow). This modification could occur by chain scission, entanglement slid or disentanglement.^{9-16,42,43} For chain scission, to break a C-C bond a force of 4 nN is required which correspond to a stress acting on the chain cross-section of about 6 GPa .⁴² However, for pristine PS films the chain pulling force was calculated to be 0.065 nN corresponding to steadily state necking stress $\tau = 94 \text{ MPa}$, it is not strong enough to break the PS chain.^{18,20} Thus, we believe that the chain scission is not a dominated mechanism in PS crazing in this study. On the other hand, we consider disentanglement occurred during plastic flow of craze. However, the entanglement points average moved distance by chain disentanglement D_d roughly equal to chain contour length between entanglements l_e (40 nm for 2 M PS).

If the entanglement loss is not a dominated mechanism in craze fibrils and molecules drawn into craze fibrils just by entanglements sliding. This sliding process leads to a change in the number of chain units between entanglements. From the TEM micrograph of fibrils structure of craze (figure 1b), the entanglement points average move distance by sliding D_s was estimated to be within the range of 2.5 to 5 nm (average $\sim 3.6 \text{ nm}$). The entanglement density ν_e will increase inside the craze fibrils, which leads to entanglements friction jam (clustering). The entanglements clustering constrain the molecules to be drawn continually into the craze fibrils. Finally, the cross-tie fibrils were formed when the necking stress acting on the chain is not strong enough to break it. Base on the above discussions, we believe that the entanglements slide is a high efficiency mechanism during the plastic flow process. In PPO system have high ν_e , thus during the plastic flow process the entanglements can not slide a long distance, and it is apt to produce entanglements clustering (have low hardening strain).^{7-8,20} Therefore, no voids structure formation during plastic flow process, and the d_e of PPO can not be higher than 13 nm . If SWCNTs can not pass through the entanglement meshes during plastic flow of SDZs, which lead to effective entanglements increasing. Contrarily, in PS systems, the fact that the SWCNTs do not

produce any increase of effective entanglements strongly indicates that CNTs can easily force through the entanglement meshes. By this, entanglement clustering should have taken place during crazing, as evident from the voids between fibrils. These results are demonstrated in the PPO/PS blend systems too.

Conclusions

In conclusion, the surface-grafted SWCNTs dispersed in a polymer matrix dramatically toughen the glassy polymer by delocalization of plastic flows. Unlike in MWCNT systems, due to the SWCNT is flexible, in all PS-PPO blends were capable to draw SWCNTs into the deformation zones. However, the interaction between the SWCNTs and glassy polymer chain during the nanoplastic flow of crazing or shear yielding in nanocomposites was observed drastically different. SWCNTs in a loose entanglement (PPO-PS blends with $\chi < 0.2$) the draw ratio of plastic flow were not altered by SWCNTs. In contrast, SWCNTs in a tight network ($\chi \geq 0.4$) the draw ratio of plastic flow were altered by SWCNTs. However, these results strongly depend on entanglement density of polymer matrix. These results also bear important information about the fundamental behavior of glassy polymer chain interacted with SWCNTs.

References

- (1) Yang, A. C. M.; Kramer E. J.; Kuo, C. C.; Phoenix, S. L. *Macromolecules* **1986**, 19, 2020.
- (2) Kramer, E. J.; Berger, L. L. *Adv. Polym. Sci.* **1990**, 91/92, 1.
- (3) Yang, A. C.-M.; Kramer, E.J. *J. Polym. Sci.-Polym. Phys.* **1985**, 23, 1353.
- (4) Yang, A. C.-M.; Kramer, E.J. *J. Mat. Sci.* **1986**, 21, 3601.
- (5) Yang, A. C. M.; Kramer E. J.; Kuo, C. C.; Phoenix, S. L. *Macromolecules* **1986**, 19, 2010.
- (6) Yang, A. C. M.; Kunz, M. S.; Logan, J. A. *Macromolecules* **1993**, 26, 1776.
- (7) Lin, J. H.; Yang, A. C. M. *Macromolecules* **2001**, 34, 3698.
- (8) Lin, C. H.; Yang, A. C. M. *Macromolecules* **2001**, 34, 4865.
- (9) Kramer, E. J. *Adv. Polym. Sci.* **1983**, 52/53, 1.
- (10) Donald, A. M., Kramer, E. J. *J. Polym. Sci.-Polym. Phys.* **1982**, 20, 899.
- (11) Donald, A. M., Kramer, E. J. *J. Polym. Sci.-Polym. Phys.* **1982**, 23, 1183.
- (12) Donald A. M.; Kramer, E. J. *Polymer* **1982**, 23, 461.
- (13) Donald, A. M.; Kramer E. J. *Polymer* **1982**, 23, 457.

- (14) Yang, A. C. M, Wang, R. C., Lin, J. H.; *Polymer* **1996**, 37, 5751.
- (15) Yang, A. C.-M.; Wang, R. C.; Kunz, M. S.; Yang, I. C. *J. Polym. Sci., Polym. Phys. Ed.* **1996**, 34, 1141.
- (16) Henkee, C. S.; Kramer, E. J. *J. Polym. Sci.-Polym. Phys.* **1985**, 22, 721.
- (17) Ma, W.; Liu, L.; Zhang, Z.; Yang, R.; Liu, G.; Zhang, T.; An, X.; Yi, X.; Ren, Y.; Niu, Z.; Li, J.; Dong, H.; Zhou, W.; Ajayan, P. M.; Xie, S. *Nano. Lett.* **2009**, 9, 2855.
- (18) Hsiao, C. C.; Lin, T. S.; Cheng, L. Y.; Ma, C. C. M.; Yang, A. C. M. *Macromolecules* **2005**, 38, 4811.
- (19) Lin, T. S.; Cheng, L. Y.; Hsiao, C. C.; Yang, A. C. M. *Mater. Chem. Phys.* **2005**, 94, 438.
- (20) Lin, C. W.; Huang, L. C.; Ma, C. C. M.; Yang, A. C. M. Y.; Lin, C. J.; Lin, L. J. *Macromolecules* **2008**, 41, 4978.
- (21) Moniruzzaman, M.; Winey, K. I. *Macromolecules* **2006**, 39, 5194.
- (22) Salvetat, J. P.; Briggs, G. A. D.; Bonard, J. M.; Bacsá, R. R.; Kulik, A. J.; Stockli, T.; Burnham, N. A.; Forro, L. *Phys. Rev. Lett.* **1999**, 83, 944.
- (23) Kong, H.; Gao, C.; Yan, D. *Macromolecules* **2004**, 37, 4022.
- (24) Berger, L. L. *Macromolecules* **1989**, 22, 3162.
- (25) Whitten, P. G.; Brown, H. R. *Phys. Rev. E.* **2007**, 76, 026101.
- (26) Rottler, J.; Robbins, M. O. *Phys. Rev. E.* **2003**, 68, 011801.
- (27) Rubinstein, M.; Colby, R. H. *Polymer Physics*, Oxford University Press, Oxford, 2003; Chapter 9.
- (28) Lee, J. Y.; Zhang, Q.; Wang, J. Y.; Emrick, T.; Crosby, A. J. *Macromolecules* **2007**, 40, 6406.
- (29) Lee, J. Y.; Zhang, Q.; Emrick, T.; Crosby, A. J. *Macromolecules* **2006**, 39, 7392.
- (30) Crosby, A. J.; Lee, J. Y. *Poly. Rev.* **2007**, 47, 217.
- (31) Melick, H. G. H; Govaert, L. E.; Meijer, H. E. H. *Polymer* **2003**, 44, 2493.
- (32) Si, L.; Massa, M. V.; Veress, K. D.; Brown, H. R.; Jones, R. A. L. *Phys. Rev. Lett.* **2005**, 94, 127801.
- (33) Krupenkin, T. N.; Fredrickson, G. H. *Macromolecules* **1999**, 32, 5029.
- (34) Gibson, S. L.; Pathak, J. A.; Grulke, E. A.; Wang, H.; Hobbie, E. K. *Phys. Rev. Lett.* **2004**, 92, 048302.
- (35) Schmid, C. F.; Klingenberg, D. J. *Phys. Rev. Lett.* **2000**, 84, 290.
- (36) Xu, D. H.; Wang, Z. G.; Douglas, J. F. *Macromolecules* **2008**, 41, 815.

- (37) Kharchenko, S. B.; Douglas, J. F.; Obrzut, J.; Grulke, E. A.; Migler, K. B. *Nat. Mater.* **2004**, 3, 564.
- (38) Salvétat, J. P.; Briggs, G. A. D.; Bonard, J. M.; Bacsá, R. R.; Kulik, A. J.; Stockli, T.; Burnham, N. A.; Forro, L. *Phys. Rev. Lett.* **1999**, 82, 944.
- (39) Riley, W.; Sturges, L. D.; Morris, D. H. *Mechanics of Materials*: Wiley, Asia, 2006; Chapter 8.
- (40) Mylvaganam, K. Vodenitcharova, T.; Zhang, L. C. *J. Mater. Sci.* **2006**, 3341.
- (41) Jensen, W.; Kis, A.; Zettl, A. *Phys. Rev. B.* **2007**, 76, 195436.
- (42) Kaucsh, H. H. *Macromol. Symp.* **2004**, 214, 17.
- (43) Arlette, R. C. B.; Robbins, M. O. *Sicence*, **1996**, 26, 271.
- (44) Silvestre, N.; Camotim, D. *Nanotechnology in Construction 3: Proceeding of the NICOM3*, Springer Verlag, **2009**, p.p365.
- (45) Wang, C. Y.; Zhang, L. C. *Nanotechnology*, **2008**, 19, 075705.
- (46) Yankobson, B. I.; Brabec, C. J.; Bernholc, J. *Phys. Rev. Lett.* **1996**, 76, 2511.

Chapter 7/ Part B: Multi-Walled CNTs Nanocomposites

Nanoplastic Flows of Glassy Polymer Chains Interacting with Multiwalled Carbon Nanotubes in Nanocomposites

(Published at *Macromolecules* **2008**, *41*, 4978.)

Abstract

Interactions between glassy polymer chains and the uniformly dispersed carbon nanotubes (CNTs) in nanocomposites were investigated with surface-grafted multiwalled CNTs dispersed in two model polymer systems, polystyrene (PS) and poly(phenylene oxide) (PPO), representing respectively brittle and ductile polymers. Although significant mechanical reinforcement in the both systems was observed, drastically different microscopic interactions, engendered from variations in the fundamental behavior of entangled chains, were noted during the nanoplastic flow of crazing or shear yielding in the nanocomposites. As revealed by a local stress analysis based on atomic force microscopy, “extensibility” of the entanglement network determines not only the mode of deformation leading to either crazing or shear yielding but also how the stretched chains interact with individual nanotubes. The results bear important implications on our understanding toward the fundamental behavior of entangled macromolecules in the glassy state.

Introduction

The nanocomposites based on well-dispersed carbon nanotubes (CNTs) embedded in carefully selected polymer matrices have increasingly attracted attention due to their great potentials for innovative mechanical, electrical, thermal, and optoelectronic properties. The outstanding advantageous properties of CNTs, such as the exceedingly high Young's modulus^{1,2} and conductivities^{3,4} and large flexibility limits and fracture strains,⁵ and the simple fact that they are tiny tubules with extremely high aspect ratios have made CNT an ideal filler for most polymers. In this context, the interactions between the embedded CNTs and the surrounding polymer chains not only are very interesting in the light of unveiling the fundamental chain behavior of the entangled macromolecules. They however also are of vital importance due to requirement of controllable CNT-polymer interactions down to the nanometer scales for successful modification of the physical properties. Previous work on CNTs as fillers in polymers has been focused primarily on the low-strain elastic behavior and cracking properties.^{6–15} Little attentions had been paid to the more important plastic flows regime that constitutes the major part of the mechanical performance before

fracture. The elastic modulus and breaking stress in polystyrene (PS) were shown by Qian et al.^{9,16} to increase significantly by the addition of CNTs, pointing to the significant role of load transfer of CNTs. Watts et al.¹⁷ also identified the CNT pull-out mechanism during cracking, which effectively retarded the fracture in the CNTs-PS thin films. Apparently, observations of the CNT effects on stress transfer or failure processes strongly depend on the state of CNT dispersion and their interactions with the polymer chains.

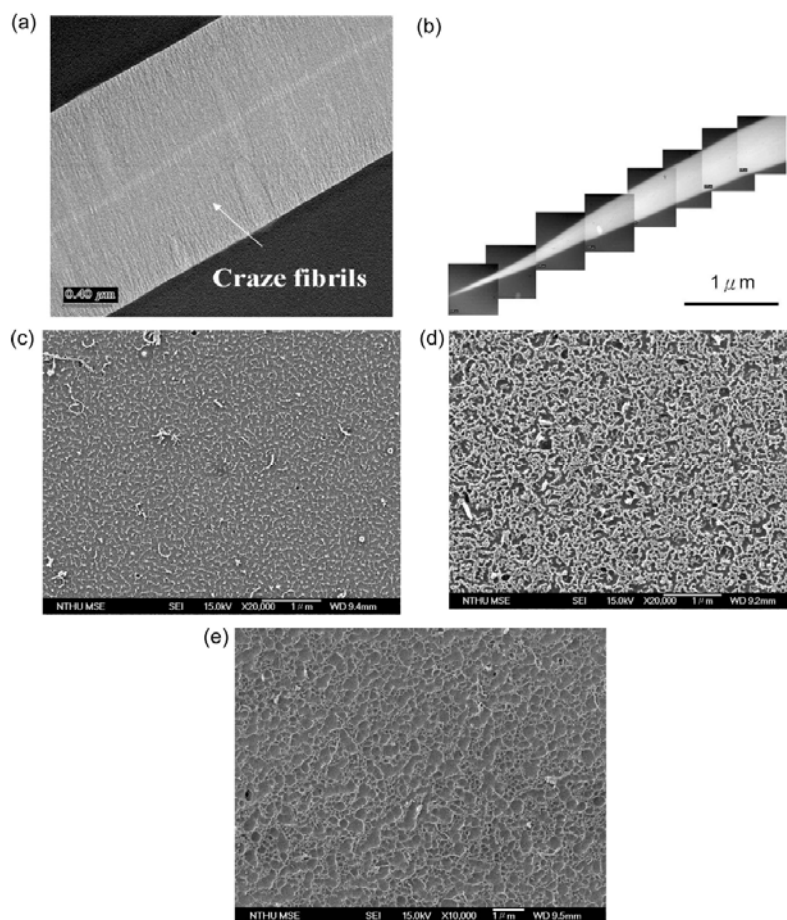


Figure 1. (a) a TEM micrograph of a craze in pristine PS film. (b) TEM micrograph of a shear deformation zone in pristine PPO film. (c-e) SEM micrographs of the plasma etched nanocomposites showing good CNT dispersion: (c) PS matrix with $c_0 = 2.0$ wt %; (d) PS matrix with $c_0 = 5.0$ wt %; (e) PPO matrix with $c_0 = 2.4$ wt %.

Moreover, given the above-mentioned reinforcement effects, it is disappointing to observe that the optimal CNT reinforcement results were always observed in the regime of a small CNT fractions (~ 1 -2 wt %)^{10,13,18-20} while the properties, like that caused by most other fillers beyond a percolation threshold, fell off considerably for higher CNTs loadings (> 5 wt %).^{11,21} It indicates the necessity of more in-depth

investigation of the CNT-polymer interactions over a wider range of deformation that includes both the elastic and plastic behavior. It is well-known that glassy polymers develop microscopic deformation zones of crazes^{22–35} or shear deformation zones (SDZs)^{22,25,27,32} before fracture (Figure 1, parts a and b). The stress-induced local plastic flow that gives rise to the formation of these microscopic deformation zones triggers extraordinarily large plastic strains (~200-300%) within the deformation zones and is the basic molecular mechanism for yielding in most glassy polymers.

The occurrence of crazes or SDZs depends on the entanglement density ν_e of the polymer matrix.^{22,30–32,34} In addition, crazing and shear yielding represent respectively the precursor of brittle and ductile fracture of glassy polymers. They are both produced by micronecking induced during the plastic flow,^{33–35,37,39} but the microstructures are quite different in that crazes are constructed by interconnected fibrils embedded in voids while SDZs are microscopically thinned smooth regions (Figure 1).^{22,25,28–32,34,36,39} The diameters of the craze fibrils are in the range of 6-20 nm, thus the local deformations are deemed to be nanoplastic flows. The microscopic reinforcement mechanisms of CNTs in glassy polymers should lie in the CNT interactions with these nanoplastic flows.

Previously, the role of multiwalled CNTs (MWCNTs) during crazing in PS-CNTs nanocomposites was explored^{38,39} and strain delocalization was identified to be the origin of fracture toughness enhancement. In these nanocomposites, most CNTs were observed to be excluded from crazes. In this study, more thorough investigation of the interactions between MWCNTs and polymer chains was undertaken by further examining the MWCNTs reinforcement in PS and in the SDZ-forming poly(phenylene oxide) (PPO). The work has led to a more complete and coherent scenario of the interactions between CNTs and polymer chains that satisfactorily explains reinforcement due to CNTs. The role of entanglement chain network during plastic flow in the nanocomposite was also unveiled, which sheds important light on the fundamental behavior of polymer chains in the glassy state.

Experimental Section

Monodisperse PS of molecular weight (M_w) 2000K (Pressure Chemical Co.) and PPO polymer with M_w 244K (Aldrich Chemical Co.) were used as-received. The MWCNTs (DESUN Nano Co., Taiwan) for this study, as determined from TEM examinations, have an average outer diameter around 10-35 nm and a length in the range of 10-30 μ m. The method of preparing the surface-grafted MWCNTs with long PS chains (PS-*g*-MWCNTs) was reported elsewhere^{38,39} and will not be

re-emphasized here. The average molecular weight of the grafted PS in PS-MWCNTs was measured to be around 60K (polydispersity \approx 2.1) from gel permeation chromatography after the defunctionalization process.⁴⁰ As determined from thermogravimetric analysis (TGA), the weight fraction of PS in PS-MWCNTs nanocomposites is approximately 60 wt %. The average length of PS-g-MWCNTs is around 1-3 μ m.

The grafted MWCNTs were then mixed with the neat PS (or PPO) in toluene from which thin films (MWCNTs/PS or MWCNTs/ PPO) with film thickness controlled at approximately 0.5 μ m were spincoated on clean glass slides from the solution. The fraction of the surface-grafted MWCNTs in the film (c_0) ranges from 0 to 10 wt %. The films were then transported and bonded to a supporting copper grid for mechanical experiments.^{30,31,34,38} Before the mechanical testing, aging at 120 C for 1 h was routinely carried out for MWCNTs/PPO films to enhance the strain localization required for growing SDZs.³⁶ During the mechanical test, the nanocomposite specimen was mounted in a strain jig, stretched under an optical microscope to observe the growth of deformation zones (crazes or SDZs).^{30,31,33-35,38} The samples were then examined under an AFM (Digital Instrumental, Nanoscope IIIa) for detailed analyses of the microdeformation, including calculations of the local stress and strain in the deformation zones.^{34,35} A transmission electron microscopy (TEM, JEOL JEM-2010) was used to obtain images of crazes or SDZs of the stretched samples. Taking advantage of the film-on-grid method,^{30,31,34,38} a large number of crazes and SDZs were examined, enabling the presentation here of typical and highly reproducible data for reliable interpretations. Widening of the microdeformation zones was monitored by using a video camera attached to an optical microscope and from the images of the growing crazes or SDZs the widening velocities were obtained. The dispersion of MWCNTs in the polymer matrix was examined by using a field-emission scanning electron microscope (FE-SEM; 4500) after gently etching the samples with oxygen plasma.^{38,39} The dispersion of MWCNTs has been excellent, as shown in Figure 1, parts c and d, such that the mechanical performance of the nanocomposites is consistent and reproducible.

Results

The plastic flow induced by local strains in glassy polymers gives rise to the formation of microdeformation zones. For brittle polymers such as PS, crazes arise from large local strains up to 300%, depending on the entanglement density.^{22,30-32} On the other hand, PPO, a model system for ductile glassy polymers, develops SDZ resulted from local strain around 100% upon application of stresses. According to Kramer's ground-breaking work, the line of demarcation between the brittle and the

ductile behaviors can be defined by a critical entanglement density v_e^c such that when $v_e > v_e^c$ (tight networks) shear deformation zones prevails, while crazes dominate in the regime of $v_e < v_e^c$ (loose networks). Under ambient conditions, $v_e^c \sim 6 \times 10^{25}/\text{m}^3$.^{22,25,27} As will be shown later, the “tightness” of the chain entanglement networks determines not only whether the glassy polymer behaves in a ductile or brittle way, but also how the imbedded MWCNTs interact with the polymer chains during the plastic flow in the deformed glass.

Crazes Morphology.

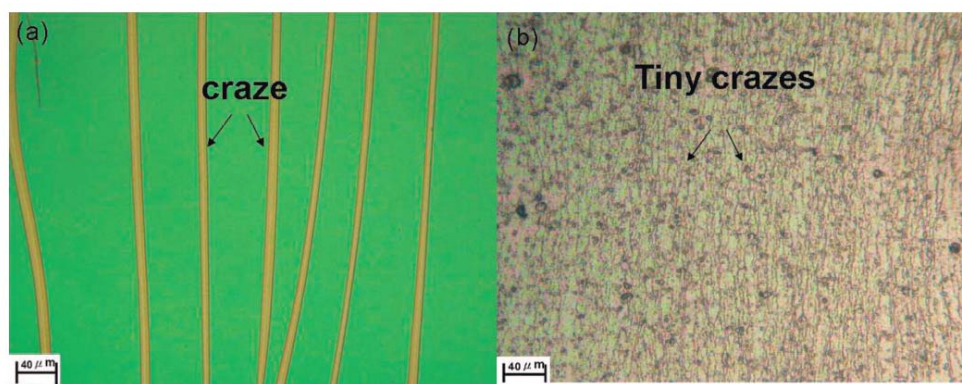


Figure 2. Optical micrographs of stretched (a) pristine PS films and (b) MWCNTs/PS composite film ($c_0 = 2$ wt %).

In the pristine PS films, crazes initiated at approximation 1% strain () and they were generally straight, widening steadily as the strain increased, and the maximum width of creases could reach approximately $20\mu\text{m}$ (Figure 2a). Local fibril breakdowns within the crazes started at approximately $\epsilon = 8\%$. Craze surface topography determined from AFM revealed that craze depth d increased almost linearly with craze width w when $w < w_c$ (see, for example, Figure 28 of ref 38). The critical width w_c is a function of film thickness (for $0.5\mu\text{m}$ thick PS film, $w_c \sim 2.5\mu\text{m}$) and representing the start of the microneck propagation.^{33–35,38,39} For $w > w_c$, craze depth became constant with w , indicating steady-state drawing of the crazing plastic flow. The films of the MWCNTs/PS composites with MWCNTs content (c_0) of 2.0 wt% demonstrated a quite different mechanical behavior in that the crazes were generally short and narrow (mostly less than $2\mu\text{m}$ wide) and no cracking was observed even at strains greater than 20% (Figure 2b). Moreover, although the craze depth d varied with craze width w following the same curve as that of pristine PS, w never reached w_c .^{38,39} It indicates that the micronecking characteristic of crazing was not altered by the presence of MWCNTs, however, the process was strongly suppressed. For films contain MWCNTs less than 1wt %, the observed effect due to MWCNTs on

the microscopic deformation behavior was not obvious and no qualitative variations from that observed in films of $c_0 = 2$ wt % were noted.

From AFM craze topography, the MWCNTs/PS nanocomposites evidently developed a concentrated plastic strain within the craze (Figure 3a, for $c_0 = 2$ wt%) with the maximum strain ϵ_p within the craze increasing with w but eventually leveling off for $w < 1 \mu\text{m}$. This is similar to the behavior of the pristine PS.^{33–35,38,39,41–43} Note that for narrow crazes ($w > 0.6 \mu\text{m}$), ϵ_p is just below 30%, a value very close to the reported elastic limit of carbon nanotubes.⁵ Figure 4a shows a TEM micrograph of a craze tip propagating into a region of densely populated MWCNTs. The presence of the MWCNTs seems to have no effect on the growth of the craze in that the craze tip penetrates right through the MWCNTs. Since ϵ_p in the narrow crazes is below the elastic limit of MWCNTs, the MWCNTs within them thus can easily survive without inflicting breakage of the MWCNTs or being forced to substantially modify the plastic flow process.

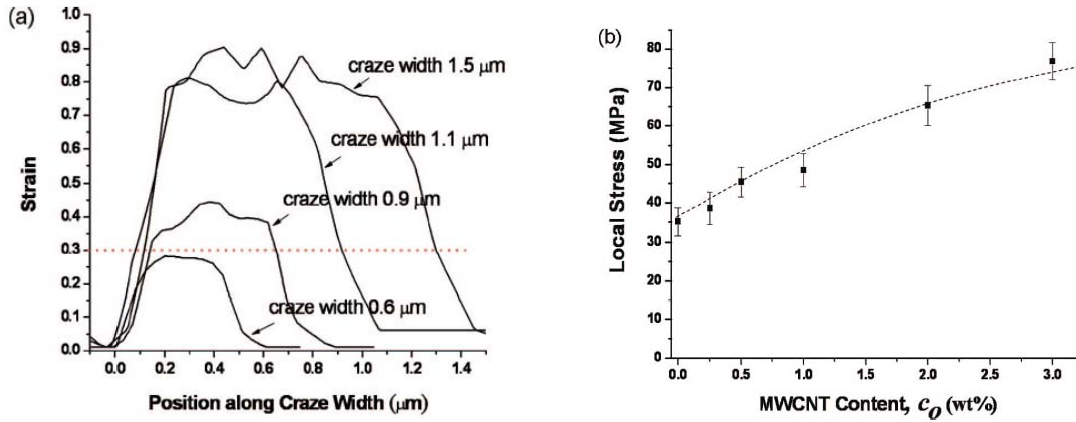


Figure 3. (a) Local strain distribution within a craze across the craze width for $c_0 = 2$ wt %, and (b) local stress within MWCNT/PS films with c_0 (for $w = 0.7 \mu\text{m}$).

In contrast, only of very rare incidence were intact MWCNTs observed within wider crazes. Generally, when craze width exceeds certain limit only broken pieces of MWCNTs were observed within the craze (Figure 4, parts b and c). Later examinations revealed that this width limit corresponds to that above which the local strain becomes significant in comparison to the extension limit of MWCNTs. The intact MWCNTs in the wider crazes were either incorporated from craze tips or from fibrillation of the “film” islands within crazes, which were formed by the merging of locally parallel crazes to traps intact MWCNTs within the new crazes. It seems quite unlikely for the plastic-flowed PS chains to pull MWCNTs across the craze boundaries into the microdeformation zones. Most MWCNTs embedded in the PS

matrix appeared to stay outside the crazes. For those MWCNTs incorporated within crazes, depending on the drawing history, they were subject to different degree of stretching. Some were broken, leaving broken ends at the boundaries (Figure 4c). The local stresses within crazes in the films determined from AFM topography were in the order of 150 MPa. Since they were significantly less than the fracture stress of CNTs, the breakages of MWCNTs were likely to have occurred at the defects sites induced during surface treatments. Moreover, in the wider crazes ($w < 0.6 \mu\text{m}$) the plateau plastic strain ϵ_p (Figure 3a) had exceeded the flexibility limit of MWCNTs, hence either forced breakage or stress-shielding of the surrounding by the incorporated MWCNTs would occur. The latter should lead to a constraint craze widening, but it only played a minor role due to the insignificant number of MWCNTs within crazes.

The exclusion of MWCNTs from crazing process was confirmed by AFM topography of the crazed films dry-etched by mild oxygen plasma,³⁸ of which protrusions arising from pileup of the slow-etched MWCNTs were observed bulging along the craze boundaries. The protrusion width, w_p , was determined by first measuring the apparent width of the protrusions as a function of etching time (inset of Figure 5a), and then the level-off value was taken as the protrusion width. The protrusion width was found to increase with craze width (Figure 5a). Correspondingly, the height of the protrusions was also found to increase with craze width, from 60 to 120 nm for w_p varying from 210 to 320 nm. This is consistent with the TEM observations (Figure 5b) that MWCNTs are excluded from crazes during fibrillation, engendering greater concentrations of MWCNTs at boundaries of the wider crazes.

Fibrillation Modified by MWCNTs.

The local concentration of MWCNTs at craze boundaries was calculated, from the AFM data, to assess quantitatively how craze fibrillation was modified by the pileup of MWCNTs. Assuming all the MWCNTs in the course of craze widening would be excluded from crazes fibrillation, the local concentration of MWCNTs at craze boundaries (c_{pu}) can be readily shown to depend on the original concentration of MWCNTs (c_0) in the film, the craze width (w), protruding width (w_p), the film thickness at the craze (τ_c), mass density of craze ($\rho = 0.8 \text{ g/cm}^3$), and the original film thickness (τ_0), as

$$c_{pu} = c_0(1 + w/\tau_c) \tau_c / 2w_p \tau_0 \quad (1)$$

Obviously, eq 1 applies only for the regime where the wide crazes effectively exclude MWCNTs from the nanoplastic flow. Figure 5c indicates that c_{pu} increased approximately linearly with craze width w . The slope, increasing with c_0 , is quite steep. For a $2 \mu\text{m}$ wide craze, for example, c_{pu} goes up four times to 8 wt % in films of

$c_0 = 2$ wt %. It indicated that the PS chains to be drawn across the craze boundaries need to pass through an increasingly denser network of MWCNTs at the boundaries. Thus, a greater drawing stress will be required for the PS chains to overcome the increasing chain frictions with the MWCNTs, and hence craze widening becomes more and more difficult. This ultimately enhances delocalization of the plastic flow of crazing.

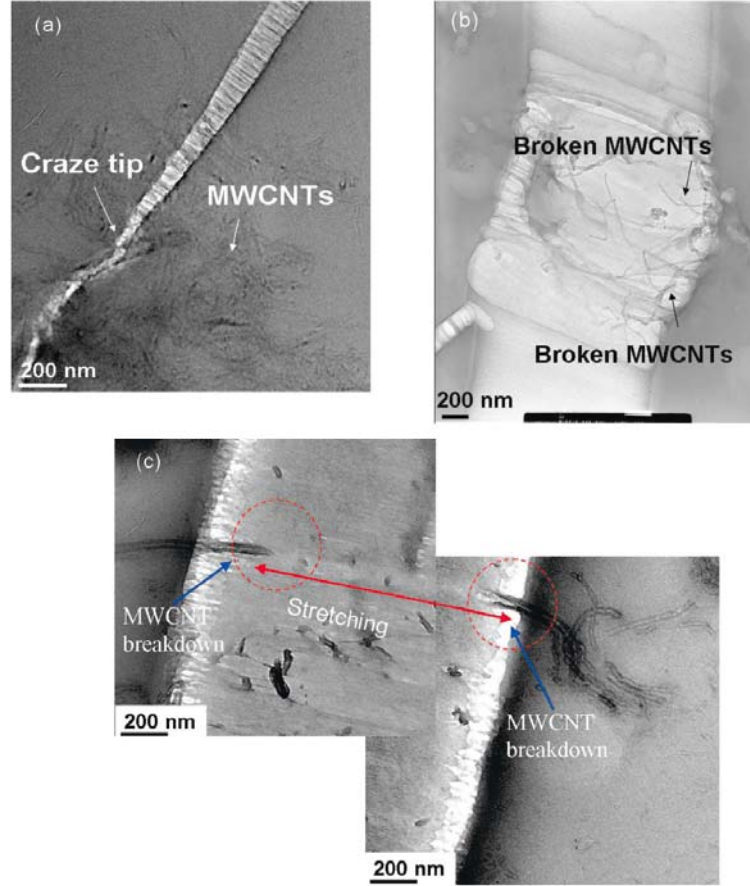


Figure 4. TEM micrographs of (a) a craze tip, (b) wider craze in MWCNT/PS films ($c_0 = 2$ wt %), and (c) fracture of nanotubes in MWCNT/PS films ($c_0 = 2$ wt %).

The increase of chain friction due to MWCNTs was estimated using a Rouse tube model.⁴⁴ During the nanoplastic flow process of a glassy polymer, the chain pulled by the necking force f was assumed to undergo a constant sliding velocity v along the “topological tube” defined by the entangled chains, where f and v are related via the total frictional coefficient ζ_R of the whole chain, as

$$f = v \zeta_R \quad (2)$$

The pulling force f can be determined from the drawing stress σ during crazing and the cross-sectional area of the chain A_{chain} by $f = \sigma A_{\text{chain}}$. The cross-sectional area A_{chain} is approximately 0.688 nm^2 for a single PS chain in the tube where a total of 22 in average share the tube space.^{44,45}

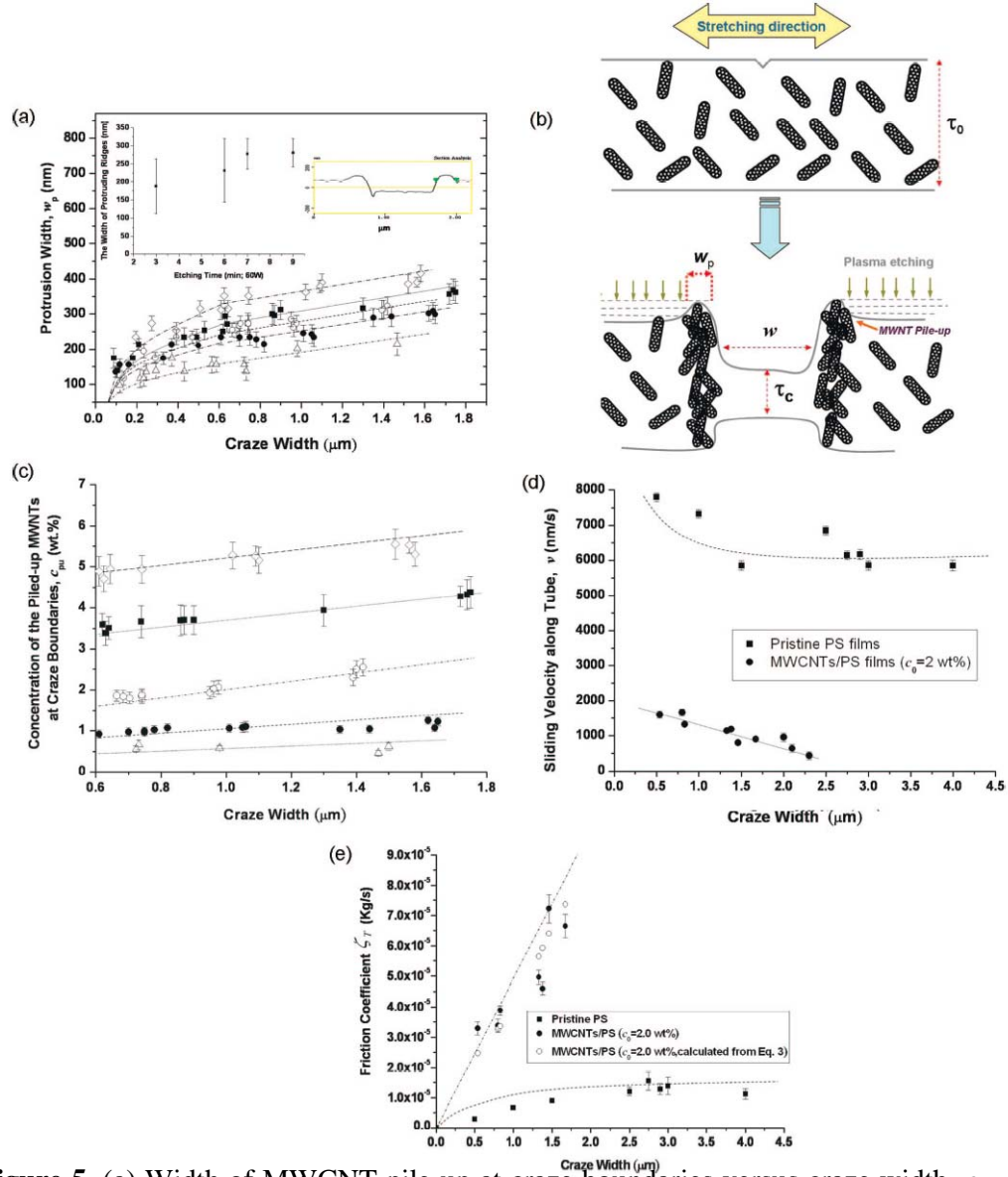


Figure 5. (a) Width of MWCNT pile-up at craze boundaries versus craze width, $c_0 = 3.0 \text{ wt \%}$ ($c_0 = 2.0 \text{ wt \%}$ ($c_0 = 1.0 \text{ wt \%}$ ($c_0 = 0.5 \text{ wt \%}$ ($c_0 = 0.25 \text{ wt \%}$. Insets: The width of the MWCNT pileup at the craze boundaries determined by AFM topographic profile and shown as a function of etching time, (b) a schematic of the MWCNT piled up at the craze boundaries, (c) the weight percentage of MWCNT protruding vs width of craze in MWNT/PS films, $c_0 = 3.0 \text{ wt \%}$; $c_0 = 2.0 \text{ wt \%}$ ($c_0 = 1.0 \text{ wt \%}$ ($c_0 = 0.5 \text{ wt \%}$ ($c_0 = 0.25 \text{ wt \%}$, (d) tube sliding velocity of a PS chain versus craze width in pristine PS and MWCNT/PS films, and (e) the friction coefficient of a PS chain versus craze

width in pristine PS and MWCNT/PS films.

For pristine PS films, the pulling force f was calculated to be $f \approx 0.065$ nN corresponding to the steady state necking stress $\tau \approx 94$ MPa determined from AFM results.^{34,35} The chain sliding velocity V was calculated from the craze widening speed, measured from video camera, at steady-state necking, which was then corrected by a factor of $N^{1/2}$ where N is the number of Kuhn monomer in the tube to take into account of the random coil chain conformation.^{44,46} For PS of $M_w = 2000K$, N is approximately 2800 (Kuhn monomer molar mass: 720 g/mol.). The craze widening velocity v was measured to be approximately 140 nm/s, the chain sliding velocity v thus is determined to be approximately 7400 nm/s. As shown in Figure 5d, v decreases slightly with craze widening until it levels as w passes the critical width w_c . The decrease obviously is due to strain hardening during the micronecking. From eq. 2, the friction coefficient of PS chain (ζ_{PS}) in the pristine polymer was calculated and found to be dependent on w . In the steady-state necking regime, $\zeta_{PS} = 1.13 \times 10^{-5}$ kg/s was obtained (Figure 5e).

For the MWCNT/PS films, MWCNT pileup at craze boundaries increases the chain frictional force during the nanoplastic flow. The friction coefficient ζ_T associated with a sliding chain going through a mixture of semidilute MWCNTs concentrations in PS where PS-CNT interactions dominate, can be described in terms of the number of nanotubes per volume v_{pu} and the MWCNT geometries (length l_{cnt} and diameter d_{cnt}) as

$$\zeta_T = \zeta_{PS} \left(1 + \frac{\pi}{30\beta} \frac{(v_{pu} l_{cnt}^3)^3}{\ln\left(\frac{l_{cnt}}{d_{cnt}}\right)} \right) \quad (3)$$

where β is a numerical factor ($\beta = 1.32 \times 10^3$).^{47,48} This equation was originally developed⁴⁷ for the rheological behavior of CNTs/polymer nanocomposites by simulating the nanocomposite as one that contains rodlike particles in a matrix. Moreover, for the sake of simplicity, the chain conformation in the MWCNTs/PS systems is assumed to be approximately the same as that in pristine PS such that the length and molar mass of the Kuhn monomer remain unchanged. Using eq 3, the chain friction ζ_T during the nanoplastic flow can be calculated from ζ_{PS} , measured from AFM, and the nanotube geometrical constants ($l_{cnt} = 1.4 \mu m$, $d_{cnt} = 35$ nm). As shown in Figure 5e, ζ_T increased almost linearly with craze width w for $0 < w < 2.0 \mu m$. Within the same craze width range, the chain sliding velocity v , readily obtained from ζ_T and the necking force f (from AFM stress analysis) using eq 2 (Figure 5d), was found to decrease steadily as craze widened, and for $w > 2.5 \mu m$, v became

approximately zero, consistent with experimental observations that virtually all crazes in the MWCNTs/PS films were narrower than $2\mu\text{m}$. The chain friction during the nanoplastic flow can also be obtained directly from craze widening measured by video taping using eq 2. The frictional coefficient τ so-obtained was found in excellent agreement with that determined based on MWCNT pileup (c_{pu}) at craze boundaries (Figure 5e). This result strongly supports that the pileup of MWCNTs at craze boundaries caused an increase in chain friction, thus restricted the widening of existing crazes, forcing new craze initiation in the other regions to absorb the applied strain.

Embrittlement Induced by MWCNTs.

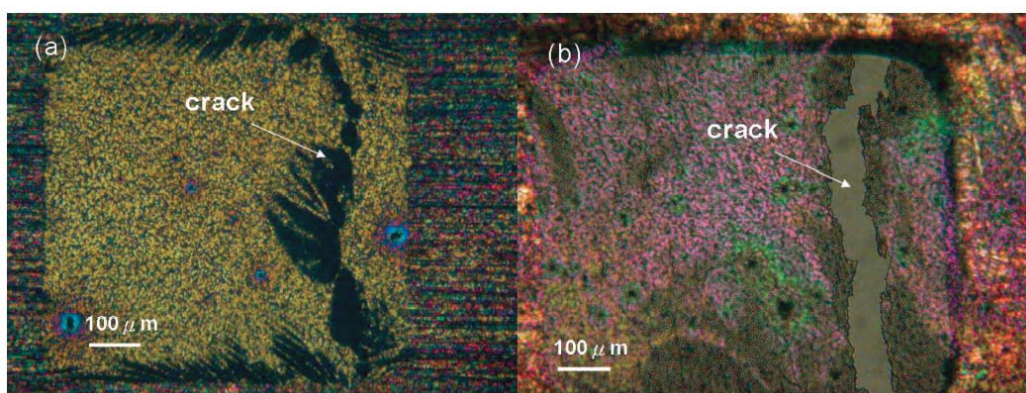


Figure 6. Optical micrographs of stretched MWCNT/PS films at high MWCNTs content: (a) 3 and (b) 5 wt %.

The exclusion of MWCNTs from the nanoplastic flow had increased the difficulty of chain fibrillation and forced a competition between initiation of new crazes and widening of the existing crazes, leading to a substantial reduction in craze widths. Since the probability of craze breakdown increases exponentially with craze width,^{30–32} delocalization of crazing reinforced the mechanical stability of the nanocomposite. Nevertheless, embrittlement ensued as the MWCNTs content increases to above 3 wt % (Figure 6). On the basis of the analyses above, the embrittlement was owing to the increased difficulty of craze initiation and the subsequent growth that follows the initiation. The local strain and stress within the incipient crazes, as shown in Figure 3, parts a and b, for $c_0 = 2$ wt %, increased with c_0 such that craze initiation would eventually be suppressed. When fewer crazes were available to absorb the deformation energy, cracking ultimately became preferentially favored.

Straining of MWCNTs within SDZs.

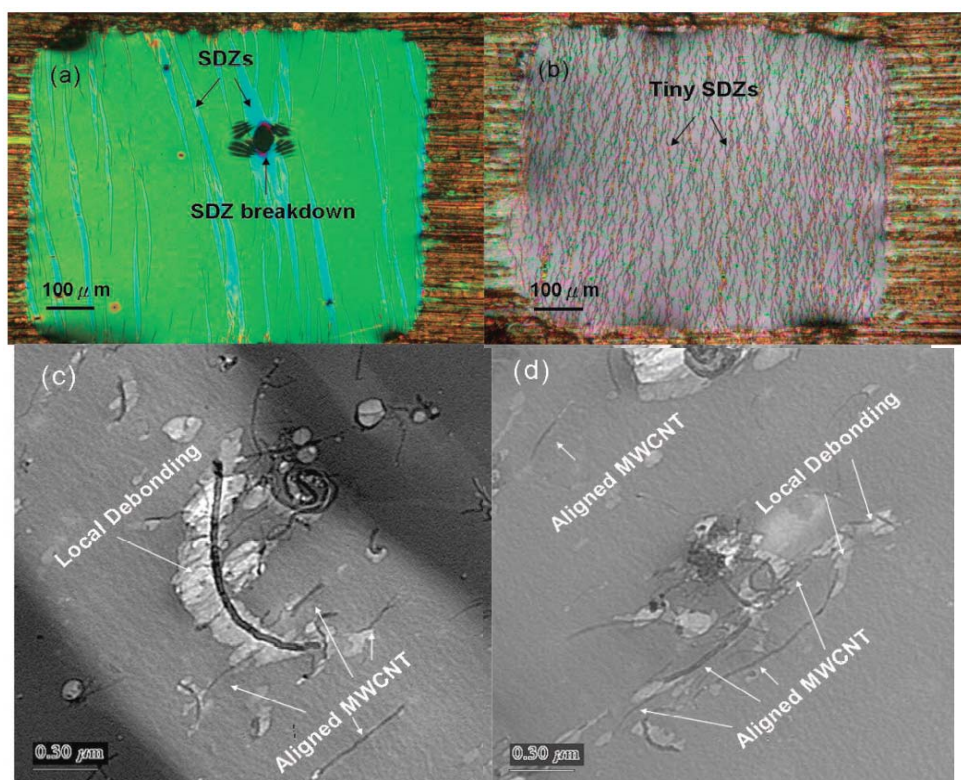


Figure 7. Optical micrographs of stretched (a) pristine PPO films, (b) MWCNTs/PPO composite film (weight fraction of MWCNT is 1.5 wt %), and (c) TEM micrographs of narrow SDZ, and (d) TEM micrograph of a wider SDZ in MWCNT/PPO films ($c_0 = 1.5$ wt %).

With straight and sharp boundaries under an optical microscope, SDZs nucleated in the neat PPO films at approximately 2%. They widened steadily as strain increased and eventually broke down to form cracks for $\epsilon > 13\%$ (Figure 7a). Before voids were initiated, however, the SDZ could grow to a width as wide as $40\mu\text{m}$. The depth d of the SDZs, measured by AFM, followed a typical micronecking characteristic in that d increased linearly with w up to $w = w_c$, thereafter leveling to a constant depression (Figure 8a). The SDZs were generally smooth, under the TEM, with some secondary wavy striations lying perpendicular to the stretching direction.

The incorporation of the MWCNTs in the nanoplastic flow, furthermore, produced an accelerated strain hardening of the flow in that the leveling depression ds decreased as c_0 increased (Figure 8, parts a and e). It decreased from 0.26, of the original thickness for the neat resin, to 0.13, for $c_0 = 2.4$ wt % (Figure 8a). Since the draw ratio (λ_{SDZ}) in the SDZs scales very closely with the leveling depression ds via $\lambda_{\text{SDZ}} \sim \tau_0/(\tau_0 - 2ds)$,^{22–25,27,30–32} The decrease of (ds/τ_0) from 0.26 to 0.13 for a change from $c_0 = 0$ to

$c_o = 2.4\%$ translates into a decrease of λ_{SDZ} from 2.08 to 1.35, a 3-fold decrease of the molecular strain. This, however, is consistent with the fact that the volume fractions of MWCNTs (c_o 's) are already significantly greater than the percolation threshold of MWCNTs, approximately 0.08 vol %, for the MWCNTs. The slope of the linear increase of d versus w during the initial necking also decreases with c_o , indicating an increase of chain friction in the PPO/MWCNTs nanocomposites.

The increase of chain friction of the nanoplastic flow in MWCNTs/PPO was estimated by use of the Rouse chains model as applied for crazes in the PS systems before with A_{chain} of the PPO chain approximately 0.55 nm^2 . For both the pristine PPO and MWCNTs/PPO films, the tube sliding velocities v 's, measured from SDZ widening, were shown, with somewhat large data fluctuations, to be indistinguishable from each other; they were almost constant ($\sim 1500 \text{ nm/s}$) but in fact slowly decrease with w (Figure 8c). The friction coefficient ζ_T was found to increase with the w when $w < w_c$ but then began leveling-off for $w > w_c$ (Figure 8d). The addition of the MWCNTs (1.5wt.%) in PPO had raised the chain friction from $\zeta_{PPO} \sim 4.3 \times 10^{-5} \text{ kg/s}$ to $\zeta_T \sim 7.5 \times 10^{-5} \text{ kg/s}$, but the overall trend remains unchanged. Clearly, the incorporation of MWCNTs during the nanoplastic flow had dramatically reduced the extensibility of the entanglement network of the PPO matrix.

Strain-Hardening of the Entangled Chains.

The intriguing differences between SDZs and crazes in the interactions with MWCNTs obviously should be related to the plastic flow properties of the entanglement network incurred during the local deformation. According to Kramer,^{22–25,27,30–32} the state of deformation induced by the deformation zones is related to the structure of entanglement network. For example, the average draw ratio of the plastic flow, λ_{craze} or λ_{SDZ} , scales approximately with the extensibility of the chain network, λ_{max} , defined as $\lambda_{max} = l_e/d_e$ where l_e is the contour length between entanglements and d_e is the direct distance between them.^{22–25,27,30–32} The PPO is known to have a tighter entanglement chain network ($\lambda_{max} = 3.1$, $v_e = 1.5 \times 10^{26} \text{ chains/m}^3$) compared to that of PS ($\lambda_{max} = 4.2$, $v_e = 3.3 \times 10^{25} \text{ chains/m}^3$) (shown schematically in Figure 9a).^{22,32} Furthermore, the deformations of the entanglement networks in both PS and PPO had been explored before by microscopic stress analyses from the AFM topography.^{33–35,37–39}

It was found that both entanglement networks manifested a twostage process, strain-softening and strain-hardening, during the deformation with a critical strain ε_h (dubbed as the hardening strain) dividing these two regimes.^{34,37} The hardening strains ε_h 's for crazing in the loose chain network of PS and that for SDZs in the tighter PPO chain network were quite different. The hardening strain ε_h of PS (of molar mass 2M)

was determined to be $\varepsilon_h = 1.4$ while it was approximately $\varepsilon_h = 0.3$ for PPO.³⁴

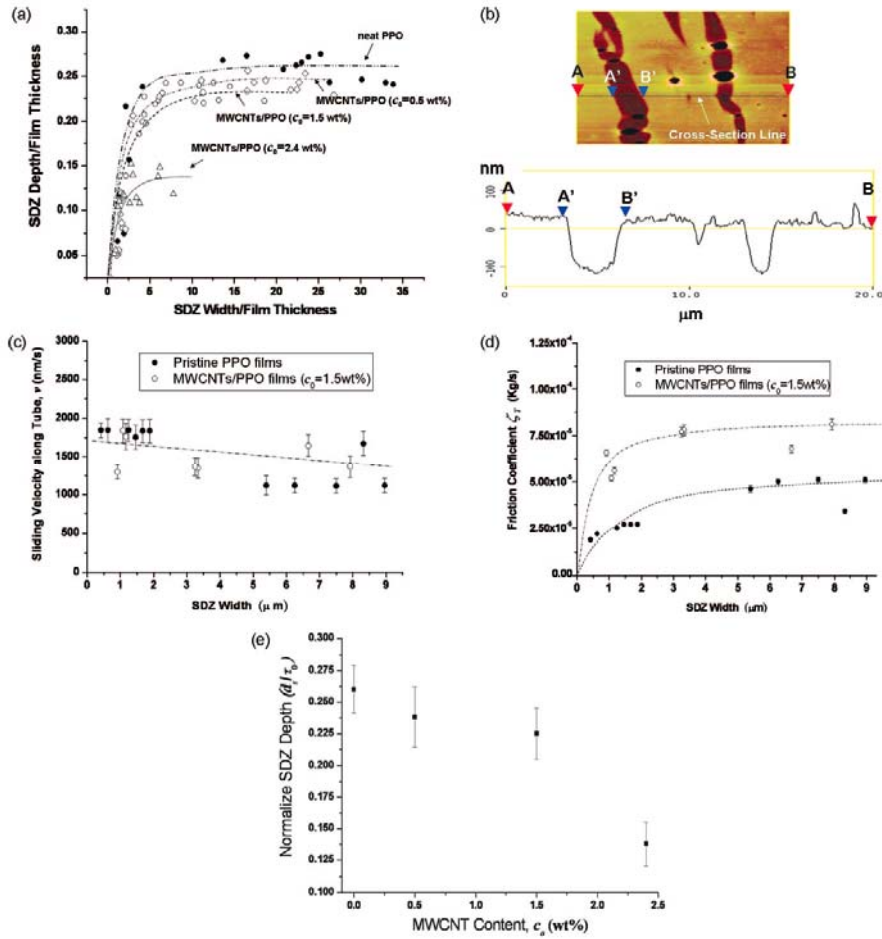


Figure 8. (a) SDZ depth vs SDZ width in the pristine PPO and MWCNTs/PPO films: pristine PPO films ($c_0 = 0$ wt %) (ζ , $c_0 = 2.4$ wt % (ζ , $c_0 = 1.5$ wt % (ζ , $c_0 = 0.5$ wt % (ζ). (b) AFM micrographs of the stretched and etched MWCNTs/PPO films. (c) Tube sliding velocity of a PPO chain versus SDZ width in pristine PPO and MWCNT/PPO films, (d) Friction coefficient of a PPO chain versus SDZ width in pristine PPO and MWCNT/PPO films. (e) Normalized SDZ depth versus α .

With this, the drawing mechanics of the plastic flows were further analyzed by comparing ε_h 's of the two polymers with the corresponding maximum strain ε_p 's (the plateau strain) in the films (Figure 9b). Although the plateau strains ε_p 's for both PS and PPO increase monotonically with w , the plateau strains ε_p 's for $w < 5 \mu\text{m}$ in MWCNTs/PS were smaller than the hardening strain ($\varepsilon_h = 1.4$) of the PS chain network. Recalling that virtually all the crazes formed in the MWCNTs/PS films were thinner than $2 \mu\text{m}$ in width, it indicates that the PS chains in the nanoplastic flows were still in the strain-softening stage, incapable of drawing the relatively much more rigid

MWCNTs into crazes. On the contrary, the plateau strains ϵ_p 's in the SDZs of MWCNTs/PPO would be greater than ϵ_h of the PPO chain network ($\nu = 0.3$) for $w > 0.6\mu\text{m}$. Since most SDZs in the MWCNTs/PPO nanocomposite were wider than that ($0.6\mu\text{m}$), the PPO chains in the nanoplastic flow were able to pull the MWCNTs into the local deformation zones.

Discussions

The length scales of interactions during the drawing of surface grafted MWCNTs by the nanoplastic flows of glassy polymers may be in the order of tens of nanometers, as hinted by the diameter of MWCNTs ($\sim 25\text{ nm}$), due to the fact that some degrees of local bending of the MWCNTs obviously deemed inevitable. Since the bending moment of CNTs increases approximately to the third power of the tube diameter, drawing of CNTs would become more dominant, as opposed to polymer draining through the CNTs, during the nanoplastic flows when the diameter of the CNTs decreases. Early results seems to confirm this picture in that single-walled CNTs (SWCNTs) were observed being drawn into crazes in films of the bulky polybenzoxazoles macromolecules where SWCNTs were surface treated by a physical adsorption means.⁴⁹

In the light of this, other than the improved compatibility that has led to uniform dispersion of CNTs in the polymer matrix, the effects of molecular weight and the amount of the grafted polymers⁵⁰ may be primarily on the magnitude of tube friction ζ_T during the nanoplastic flows. Higher molecular weights and greater polymer fractions are expected to increase the frictions. It, however, would not qualitatively alter the major observations obtained in this experiment. Further explorations in this direction is interesting but is beyond the scope of this study.

The range of CNT fractions (0-10 wt %) explored in this experiment covers the regime ($>0.1\text{ wt \%}$) where the dispersed CNTs percolate electrically.⁴⁹ However, electric percolation does not correspond to mechanical percolation where the CNTs would effectively form a network that is fully stress-bearing. As revealed by the PS systems, CNT displacement that causes substantial modifications of the purported CNTs network occurs upon stretching as polymer chains draining through the CNTs to cause local CNT pileup at the craze boundaries. In the strainhardening system of PPO, although the CNTs can be drawn into the SDZs, they at the same time did not escape the fate of strain localization and underwent fracture at a strain not significantly greater than those without them. Apparently, control over the state of entanglement between CNTs and stability of the CNTs network requires further material engineering that exploits the properties and geometries of individual CNTs as well as nanostructuring them into right space. The notion of a stress-bearing

entanglement network of CNTs that effectively shield the polymer composite from mechanical stress remains to be tested by further experiments and is out of the scope of the intended study here. For the range of very dilute CNT fractions (>1 wt %), the effect on the nanoplastic flow is minute, however.

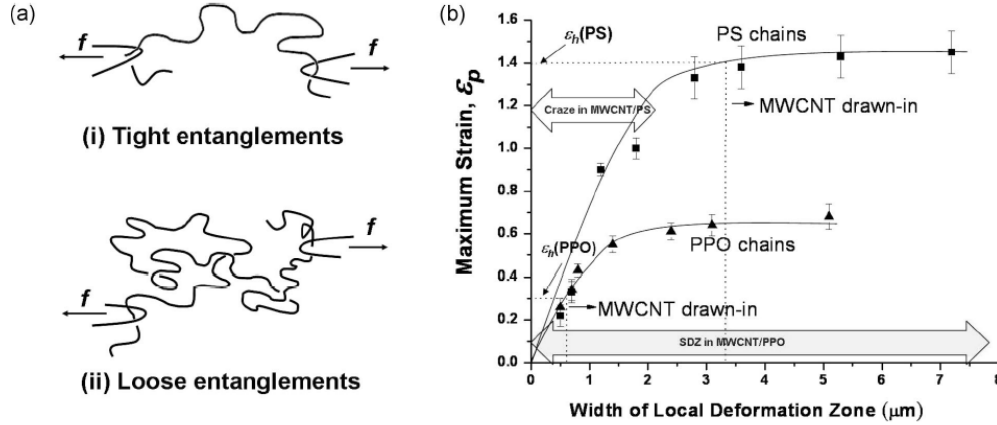


Figure 9. (a) Schematic drawings of tight and loose chain entanglements, and (b) the local maximum strain versus the width of local deformation zones.

With the micromechanical analyses based on AFM data, the interactions between the embedded MWCNTs and the glassy polymer chains during the nanoplastic flows can be understood in a simple and coherent framework in terms of the plastic flows micromechanics and the properties/structure of the chain entanglement network. The complicated effects of filler arising from MWCNTs in glassy polymers can be understood further by pursuits using this approach. The important fundamental behavior of glassy polymer chain during the nanoplastic flows of crazing or shear yielding can be unveiled with advances of the chain-MWCNTs interactions.

Conclusions

In conclusion, the surface-grafted MWCNTs dispersed in a polymer matrix dramatically toughen the glassy polymer by delocalization of plastic flows, engendered by a significant increase of chain friction during microdeformation. The interactions between the MWCNTs and polymer chains, however, are quite different for craze-forming brittle polymer (PS) and SDZ-forming ductile polymer (PPO), which can be attributed to variations in the chain entanglement network structure. For PS, the CNTs-polymer interactions during the plastic flow is in the regime of polymer strain softening in which the polymer chains drawn into crazes are filtering through the pileup of MWCNTs at craze boundaries. The pileup is resulted from the incapability of the softened chains to pull the rigid CNTs into the nanoplastic flow. In

this situation, chain friction increases linearly with craze width during widening of the craze and ultimately forces nucleation of new crazes, leading to delocalization of the strain. In contrast, the PPO chains undergo strain-hardening during the nanoplastic flow and are capable to draw MWCNTs into the SDZs, leaving no pileup of MWCNTs at the zone boundaries. The delocalization effect due to MWCNTs is thus much smaller as compared to that in MWCNTs/PS and the SDZs can still grow to a width significantly wider than crazes in PS/MWCNTs of the same MWCNTs loadings. The physical participation of MWCNTs in the nanoplastic flows of PPO has generated an increase of chain friction although it does not alter qualitatively the dependence of chain friction on the degree of drawing during the flow. The incorporation of MWCNTs in the flow considerably reduce the extensibility of the glassy polymer, giving rise to substantially lower plateau strain of the plastic flow (3 time reduction for $c_0 = 2.4$ wt %) and higher draw stress (1.5 time increase for $c_0 = 2.4$ wt %). At high MWCNTs contents in either PS or PPO, the increase of chain friction eventually suppresses the formation of crazes or SDZs and ultimately leads to embrittlement of the nanocomposites.

References and Notes

- (1) Yu, M. F.; Lourie, O.; Dyer, M. J.; Moloni, K.; Kelly, T. F.; Ruoff, R. S. *Science* **2000**, 287, 637.
- (2) Hwang, G. L.; Hwang, K. C. *Nano Lett.* **2001**, 1, 435.
- (3) Bekyarova, E.; Itkis, M. E.; Cabrera, N.; Zhao, B.; Yu, A.; Gao, J.; Haddon, R. C. *J. Am. Chem. Soc.* **2005**, 127, 5990.
- (4) Hecht, D.; Hu, L.; Gruner, G. *Appl. Phys. Lett.* **2006**, 89, 133112.
- (5) Yakobson, B. I.; Campbell, M. P.; Brabec, C. J.; Bernholc, J. *Comput. Mater. Sci.* **1997**, 8, 341.
- (6) Yang, Y.; Gupta, M. C.; Dudley, K. L.; Lawrence, R. W. *Nano Lett.* **2001**, 5, 2131.
- (7) Hill, D. E.; Lin, Y.; Rao, A. M.; Allard, L. F.; Sun, Y. P. *Macromol.* **2002**, 35, 9466.
- (8) Liu, C. H.; Fan, S. S. *Appl. Phys. Lett.* **2005**, 86, 123106–1.
- (9) Qian, D.; Dickey, E. C. *Appl. Phys. Lett.* **2000**, 76, 2868.
- (10) Blond, D.; Barron, V.; Ruether, M.; Ryan, K. P.; Nicolosi, V.; Blau, W. J.; Coleman, J. N. *Adv. Funct. Mater.* **2006**, 16, 1608.
- (11) Hwang, G. L.; Shieh, Y. T.; Hwang, K. C. *Adv. Funct. Mater.* **2004**, 14, 487.
- (12) Coleman, J. N.; Cadek, M.; Blake, R.; Nicolosi, V.; Ryan, K. P.; Belton, C.; Fonseca, A.; Nagy, J. B.; Gun'ko, Y. K.; Blau, W. J. *Adv. Funct. Mater.* **2004**, 14, 791.

- (13) Singh, S.; Pei, Y.; Miller, R.; Sundararajan, P, R. *AdV. Funct. Mater* **2003**, *13*, 868.
- (14) Zhu, J.; Kim, J.; Peng, H.; Margrave, J. L.; Khabashesku, V. N.; Barrera, E. V. *Nano Lett.* **2003**, *3*, 1107.
- (15) Li, X.; Gao, H.; Scrivens, W. A.; Fei, D.; Xu, Xiaoyou; Sutton, M. A.; Reynolds, A. P.; Myrick, M. L. *Nanotech* **2004**, *15*, 1416.
- (16) Qian, D.; Dickey, E. C. *J. Micro.* **2001**, *204*, 39.
- (17) Watts, P. C. P.; Hsu, W. K. *Nanotech* **2003**, *14*, L7.
- (18) Liu, T. X.; Phang, I. Y.; Shen, L.; Chow, S. Y.; Zhang, W. D. *Macromolecules* **2004**, *37*, 7214.
- (19) Zhang, W. D.; Shen, L.; Phang, I. Y.; Liu, T. X. *Macromolecules* **2004**, *37*, 256.
- (20) Manchado, M. A.; Valetini, L.; Biagiotti, J.; Kenny, J. M. *Carbon* **2005**, *43*, 1499.
- (21) Meincke, O.; Kaempfer, D.; Weickmann, H.; Friedrich, C.; Vathauer, M.; Warth, H. *Polymer* **2004**, *45*, 739.
- (22) Kramer, E. J. *AdV. Polym. Sci.* **1983**, *52/53*, 1.
- (23) Donald, A. M.; Kramer, E. J. *J. Polym. Sci.: Polym. Phys.* **1982**, *20*, 899.
- (24) Donald, A. M.; Kramer, E. J. *J. Polym. Sci.: Polym. Phys.* **1982**, *23*, 1183.
- (25) Donald, A. M.; Kramer, E. J. *Polymer* **1982**, *23*, 461.
- (26) Donald, A. M.; Kramer, E. J. *Polymer* **1982**, *23*, 457.
- (27) Henkee, C. S.; Kramer, E. J. *J. Polym. Sci.: Polym. Phys.* **1985**, *22*, 721.
- (28) Yang, A. C.-M.; Kramer, E. J. *J. Polym. Sci.: Polym. Phys.* **1985**, *23*, 1353.
- (29) Yang, A. C.-M.; Kramer, E. J. *J. Mater. Sci.* **1986**, *21*, 3601.
- (30) Yang, A. C. M.; Kramer, E. J.; Kuo, C. C.; Phoenix, S. L. *Macromolecules* **1986**, *19*, 2010.
- (31) Yang, A. C. M.; Kramer, E. J.; Kuo, C. C.; Phoenix, S. L. *Macromolecules* **1986**, *19*, 2020.
- (32) Kramer, E. J.; Berger, L. L. *AdV. Polym. Sci.* **1990**, *91/92*, 1.
- (33) Yang, A. C. M.; Kunz, M. S.; Logan, J. A. *Macromolecules* **1993**, *26*, 1776.
- (34) Lin, J. H.; Yang, A. C. M. *Macromolecules* **2001**, *34*, 3698.
- (35) Lin, C. H.; Yang, A. C. M. *Macromolecules* **2001**, *34*, 4865.
- (36) Yang, A. C. M.; Wang, R. C.; Lin, J. H. *Polymer* **1996**, *37*, 5751.
- (37) Yang, A. C.-M.; Wang, R. C.; Kunz, M. S.; Yang, I. C. *J. Polym. Sci.: Polym. Phys. Ed.* **1996**, *34*, 1141.
- (38) Hsiao, C. C.; Lin, T. S.; Cheng, L. Y.; Ma, C. C. M.; Yang, A. C. M. *Macromolecules* **2005**, *38*, 4811.
- (39) Lin, T. S.; Cheng, L. Y.; Hsiao, C. C.; Yang, A. C. M. *Mater. Chem. Phys.* **2005**, *94*, 438.

- (40) Kong, H.; Gao, C.; Yan, D. *Macromolecules* **2004**, *37*, 4022.
- (41) Bridgman, D. W. *Studies in Large Plastic Flow and Fracture*; Harvard University Press: Cambridge, U.K., 1964: p 9.
- (42) Hutchinson, J. W.; Neale, K. W. *J. Mech. Phys. Solids* **1983**, *31*, 405.
- (43) G'sell, C.; Marquez-Lucero, A. *Polymer* **1993**, *34*, 2740.
- (44) Rubinstein, M.; Colby, R. H. *Polymer Physics*, Oxford University Press, Oxford, 2003; Chapter 9.
- (45) The area of the confining tube (Achain) for a single PS chain was calculated by $A_{chain} = M_0 / (N_{Av} F b)$ where M_0 is the molar mass of a Kuhn monomer, N_{Av} is Avogadro's number, F is the density, and b is the Kuhn length.
- (46) A polymer segment in the wormlike tube has to move a contour length of $l = bN$ to produce a translational distance of $R = bN^{1/2}$. Therefore, the sliding velocity within the tube is $N^{1/2}$ times the linear velocity measured from deformation zone widening.
- (47) Cotiuga, I.; Picchioni, F.; Agarwal, U. S.; Wouters, D.; Loos, J.; Lemstra, P. *Macromol. Rapid Commun.* **2006**, *27*, 1073.
- (48) Doi, M.; Edwards, S. F. *The Theory of Polymer Dynamics*; Clarendon: Oxford, U.K., 1986; p 338.
- (49) Yang, A. C.-M. Micro-mechanisms of deformation, conduction percolation and nanotube crosslinking via surface grafting polymerization in CNT-polymer nanocomposites. The 4th US Air Force-Taiwan Nanoscience Initiative Workshop, University of Houston, Houston, TX, February 8-9, 2007.
- (50) Lee, J. Y.; Zhang, Q.; Emrick, T.; Crosby, A. J. *Macromolecules* **2006**, *39*, 7392.